POLITECNICO DI TORINO

Department of Structural and Geotechnical Engineering

Master Degree in Civil Engineering

Master Degree Dissertation

SEISMIC RELIABILITY OF BRIDGES ISOLATED WITH SINGLE-CONCAVE FRICTION PENDULUM BEARINGS

Supervisors
Prof. Eng. Paolo Castaldo
Illustrious Prof. Eng. Giuseppe Mancini

Candidate
Elisabetta Tunesi
231151

December 2017

"Se tu hai una mela
ed io ho una mela
e ce le scambiamo,
allora tu ed io avremo
sempre una mela per uno.
Ma se tu hai un'idea
ed io ho un'idea
e ce le scambiamo,
allora avremo
entrambi due idee"

George Bernard Shaw

DEDICATIONS

To the ones who make me happy.

Approfitto di questa occasione per dedicare un pensiero a voi che mi avete accompagnato in questo arduo e talvolta estenuante percorso, addolcito però dal vostro costante sostegno, che ha reso più facile superare ostacoli apparentemente insormontabili. Francamente, mi scuso per questo gesto tanto banale quanto scontato. Se è vero però che "*verba volant, scripta manent*", allora vorrei lasciare scolpiti, come incipit di questo mio lavoro, l'affetto e la gratitudine che nutro nei vostri confronti.

Nei confronti dei miei genitori. A voi porgo un abbraccio immenso e, cosa che non ho mai fatto abbastanza, un sincero, sentito grazie. Grazie per avermi cresciuto libera di essere me stessa. Grazie per aver sopportato le mie pazzie, nelle quali avete comunque sempre creduto, forse anche più di me. Sono orgogliosa di essere vostra figlia e di avere voi come esempio e fonte di ispirazione. *Last but not least*, grazie per tutte le mattine di questi ultimi anni in cui vi siete svegliati con me, per me, alle luci dell'alba. Siete persone straordinarie.

Nei confronti di mio zio Michele. Grazie per esserci sempre. Grazie per aver reso la mia infanzia ancora più divertente e ogni momento difficile più piacevole, con la tua presenza e la tua unica, incomparabile simpatia.

Nei confronti di Nicolò. Grazie per la pazienza e la comprensione che mi hai dimostrato e che, mi dispiace, a volte ho anche un po' preteso. Grazie per l'aiuto, l'appoggio, lo stimolo che mi hai dato. Grazie per tutte le dritte e i consigli che fino all'ultimo ti ho chiesto. Grazie per la splendida persona che sei. La vita con te è in un'alt(r)a dimensione.

Nei confronti di Paolo Castaldo, mio relatore e punto di riferimento per la realizzazione di questo lavoro. In lui ho trovato una persona professionale ma al tempo stesso amica, con cui ho trascorso giornate di studio intense, ma alleggerite dalla gradevole compagnia, sua e dei suoi colleghi. A lui sono profondamente riconoscente per aver contribuito ad arricchire la mia preparazione, trasmettendomi parte delle sue stimabili conoscenze.

Nei confronti del mio Aristotele, il cui affetto felino è per me essenziale e fonte di gioia immensa. Grazie per la vitalità, la serenità, la dolcezza che ogni giorno mi trasmetti.

CONTENTS

INTRODUCTION

This thesis aims at evaluating the optimal properties of Friction Pendulum (FP) isolating devices and assessing the seismic reliability of isolated multispan bridges, with the intent to provide design criteria and diagrams according to the performance based earthquake engineering philosophy.

Bridges are key elements of transportation systems. Previous seismically induced damages to these structures, the significant cost of reconstruction and the need to bridges' immediate operation revealed the necessity of seismic vulnerability assessment of them according to performance based design concepts. Such methodology requires accurate prediction of seismic capacity of the bridges and seismic demand associated to them.

In the latest forty years, earthquakes caused severe damages to civil infrastructures all over the world, with an increasing trend. Lots of important bridges collapsed, even if designed to resist seismic actions: this was mainly due to their usual structural simplicity, which makes them be very vulnerable to seismic damaging. The latter primarily occurs in the piers, and then it may result in collapse of the bridge spans. Although the *Capacity Design* concepts have been widely accepted for seismic design of buildings, they may not be appropriate for bridges, since they do not usually exhibit structural redundancy because of their simply supported static scheme.

Among the design strategies aimed at mitigating the effects of earthquakes, seismic isolation has emerged as the most promising one. It creates, by means of appropriate bearings, a structural discontinuity which allows large relative horizontal displacements between the upper part, defined as *superstructure*, and the lower one, called *substructure*, so that the superstructure mass is uncoupled from seismic ground motions and the energy transmitted by the earthquake to the structure is reduced. Friction Pendulum Systems (FPS) are particular types of seismic isolators, which allow relative displacements between the super- and substructure by means of spherical surfaces. The energy dissipation is provided by the friction encountered during the movement of the sliding surfaces. Hence, the dynamic response of these devices is strictly related to their frictional behaviour. Besides, they provide a restoring force, thanks to the surfaces curvature, which also allows the devices returning to their initial position after a seismic event. This way, the isolating system permits to obtain an elongation of the natural period of the structure, towards frequency values lower than those typical of earthquakes, and allows to dissipate the seismic input energy, thanks to its frictional behaviour. Experimental studies attested the intrinsic randomness of the

dynamic behaviour of FP devices, due to the dependence of the friction coefficient on non-controllable parameters, such as sliding velocity, contact pressure and temperature. Consequently, the modelling of these devices has been set in accordance to a probabilistic approach.

A multi-degree-of-freedom system has been considered, modelling the bridge with a linear behaviour and the isolators with a nonlinear one, characterised by a velocity-dependent model. The seismic response of the structural system has been evaluated by considering the earthquake input as a stochastic random process. To perform the analyses, a dimensionless form of the motion equations, respect to the seismic intensity level, has been implemented in order to reduce the number of parameters controlling the problem. This approach led to a condensed presentation of the structural response and allowed exploring, through an extensive parametric study, wide ranges of isolator and bridge properties and different seismic intensity levels.

Since the estimates of the response statistics obtained for each parameter combination reflect the effect of the variability of the characteristics of the selected records at different intensity levels, they may be used for seismic risk analyses.

Accordingly, an Incremental Dynamic Analysis (IDA) has been firstly performed, to reach the relationship between the seismic demand and the capacity of the structure and evaluate the structural performance accurately.

IDA results allowed evaluating the seismic vulnerability of bridges and developing their fragility curves, which have been integrated with hazard curves in order to assess the seismic reliability of the structure, so as to define a reliability criterion to assist the design of the Friction Pendulum dimensions in plan.

1
SEISMIC RELIABILITY AND GENERAL DESIGN CRITERIA

Seismic structural design may be seen to have been in constant evolution over the last century. Initially, following structural damage in the earthquakes of the early 20th century (Kanto, Long Beach, Napier), seismic attack was perceived in terms of simple mass-proportional lateral forces, resisted by elastic structural action. In the 1950's the influence of structural period in modifying the intensity of the inertia forces started to be incorporated into structural design, but structural analysis was still based on elastic structural response. Ductility considerations were introduced in the 1960's and 70's as a consequence of the experimental and empirical evidence that well-detailed structures could survive levels of ground shaking capable of inducing inertia forces many times larger than those predicted by elastic analysis. Gradually this led to a further realization, in the 1980's and 90's, that strength is important, but only in that it helps to reduce displacements or strains, which may be directly related to damage potential, and that the proper definition of structural vulnerability should hence be related to deformations, not strength.

1.1 *PERFORMANCE BASED SEISMIC DESIGN*

Design for seismic resistance has been undergoing a critical reappraisal in recent years, with the emphasis changing from *strength* to *performance*. For most of the past seventy years – the period over which specific design calculations for seismic resistance have been required by codes – strength and performance have been considered to be synonymous. However, over the past forty years there has been a gradual shift from this position with the realisation that increasing strength may not enhance safety, nor necessarily reduce damage. The development of *Capacity Design* principles in New Zealand in the 1970's (Park and Paulay, 1976) was an expression of the realisation that the distribution of strength through a building was more important than the absolute value of the design base shear. This may be identified as the true start to performance based seismic design, where the overall performance of the construction is controlled as a function of the design process.

Experience from recent earthquakes demonstrates that design codes have been successful in meeting the primary objective of limiting the loss of life. However, many of the constructions that structural engineers consider to have performed successfully during an earthquake represent a substantial economic loss for the owner. Although it is usually possible to repair a structure damaged by an earthquake, often it is not practical to do so, especially considering the often high replacement cost of non-structural equipment, finishes and contents. Consequently, the economic impact of structural damage in terms of interruption of business and disruption to the community may be staggering.

The concept of performance based design was developed in an attempt to narrow the gap between the expectations that society places on structural performance during an earthquake and the philosophy that structural engineers use to develop the design codes. In 1995 the Structural Engineers Association of California issued an overview of the objectives of performance based seismic design. Target levels of structural response have been defined relative to the anticipated condition of the construction after earthquakes of varying intensity. In particular, four states of damage have been related to four earthquake intensities (Table 1.1). Expected levels of damage to structural members, architectural elements and mechanical systems also have been defined for each damage condition. During the design process, the engineer would consider each earthquake level and check that the calculated structural response is consistent with the expected performance.

Earthquake Designation	Return period [yrs]	Probability of Exceedance (in 50 years)	Condition of Standard Occupancy Structure
Frequent	30	81%	Fully Operational
Occasional	50	63%	Operational
Rare	475	10%	Life Safety
Very rare	975	5%	Near Collapse

Table 1.1 – Performance Objectives for buildings and bridges
(Norme Tecniche per le Costruzioni, 2008)

The relationship between these performance levels and earthquake design level is summarised in Figure 1.1:
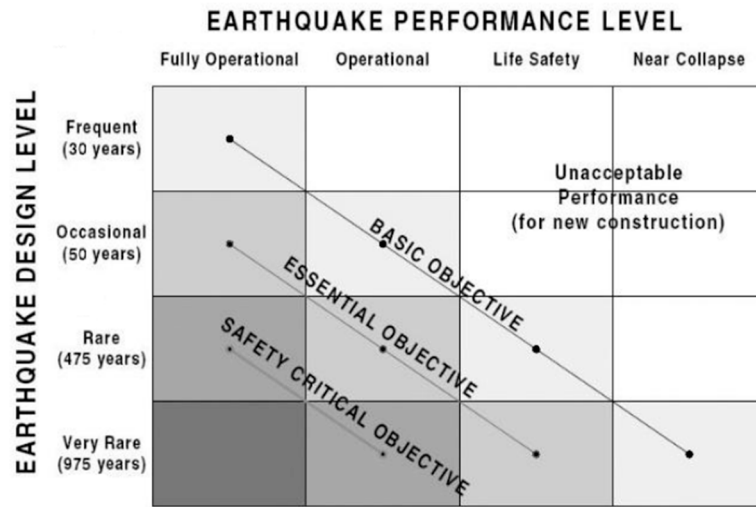
*Figure 1.1 – Relationship between earthquake design level and performance level
(Structural Engineers Association of California, 1995)*

The definition of performance limit states, from which the assessment of structural reliability may be carried out, is a complex issue that may be solved by identifying appropriate damage variables to describe the structural system condition. In bridges seismic design, one of the most important parameters is the ratio between the maximum column displacement and the column height, also known as drift index (Table 1.2). This parameter strictly depends on the structural typology and may be inferred from both experimental surveys and inspections on earthquake-damaged structures.

Limit state	Damage Description	Column drift index
Fully Operational	First yield	0.007
Operational	Cracking, Spalling	0.015
Life Safety	Loss of anchorage	0.025
Near Collapse	Incipient column collapse	0.05

Table 1. 2 – Description of bridges damage states (Dutta & Mander , 1999)

1.2   *SEISMIC RISK*

Seismic risk represents the risk of damage from earthquake to a construction, system or other entity; it has been defined as the potential economic, social and environmental consequences of hazardous events that may occur in a specified region and in a given period of time. Actually, another important concept associated with risk is *hazard*. Seismic hazard is a natural phenomenon such as ground shaking, fault rupture, or soil liquefaction that is generated by an earthquake, whereas seismic risk is the probability that humans will incur loss or damage to their built environment if they are exposed to a seismic hazard. The consequences of an earthquake also depend on the structural resistance to the effects of a seismic tremor. A construction's potential for damage is known as *vulnerability*. The more vulnerable a structure is (due to its type, inadequate design, poor quality materials and construction methods, lack of maintenance), the greater the consequences will be. Finally, the number of assets exposed to risk, the possibility in other words of damage in economic terms, to cultural heritage or the loss of human lives, is defined *exposure*. The loss is typically quantified in terms of the cost to return the system to its state before the earthquake. Therefore, seismic risk is an interaction among seismic hazard, vulnerability and exposure.

The determination of seismic risk is one of the most important issues for dealing with uncertainty in risk mitigation decision-making, a key step in risk management. In general, seismic risk may be qualitatively expressed by the combination of seismic hazard, vulnerability and exposure:

$$Seismic\ Risk = Seismic\ Hazard \times Vulnerability \times Exposure \qquad (\mathbf{1.1})$$

Since the exposure is related to the urban and infrastructural risk, which is competence of urban planning matters, it may be assumed equal to one. Hence, as shown in Equation 1.1, high seismic hazard does not necessarily mean high seismic risk and vice versa. There is no risk if there is no vulnerability, even though there is a high seismic hazard. Equation 1.1 also shows that engineering design or a policy for seismic hazard mitigation may differ from design and policy decisions related to seismic risk reduction. It may or may not be possible to mitigate seismic hazard, but it is always possible to reduce seismic risk, either by mitigating seismic hazard, reducing the vulnerability, or both.

Considering the aspects related to structural damage, and thus the limit states that may be reached because of a seismic event, the risk may be defined as the probability of collapse in a specific period of time (e.g., the useful life of the structure), whose *limit state function Z* is negative if the corresponding limit condition is reached or exceeded. The probability that

Z is negative identifies the failure probability P_f. In seismic applications, the Z function may be expressed by comparing the seismic demand D, namely the required performance of the structure by seismic action, and the effective capacity C of the structure, which may be represented in terms of displacement or resistance. According to these definitions, the risk may be expressed as:

$$P_f = P[Z \leq 0] = P[C \leq D] \tag{1.2}$$

Seismic risk quantification is very complicated and somewhat subjective because it not only depends on the desired physical measurement (i.e., magnitude, ground motion, fatalities, or economic loss), but also on how the hazard and vulnerability interact in time and space. The hazard and vulnerability may interact at a specific site (site-specific risk) or over an area (aggregate risk). To assess seismic risk, a model has to be assumed or introduced to describe how the hazard and vulnerability interact in time. The most commonly used model for seismic risk estimation is the Poisson one.

To evaluate the probability of failure P_f, it is necessary separating the structural response from the probabilistic demand (Cornell A. , 2004):

$$P_f = \sum_a P[C \leq D | IM = a] \cdot P[IM = a] \tag{1.3}$$

in which the first term indicates the conditional probability of failure given a seismic intensity IM, i.e., the fragility (vulnerability), while the second term identifies the probability that an earthquake with intensity IM equal to a occurs, i.e., the seismic hazard of the site. IM is a concise parameter measuring the intensity of the earthquake: usually, peak parameters are used, such as the PGA and the response spectrum. Integral parameters, such as the duration of the seismic event, may be used, even if they play a secondary role in the structural performance.

The mathematical correct expression of Equation 1.3 is:

$$\lambda_f = \sum_i \lambda_i \cdot \int_{IM} P[C \leq D | IM = im] \cdot f_{IM_i} \, d(im) \tag{1.4}$$

which identifies, by means of the integral of the product between the seismic fragility and seismic hazard, the average number of events leading to the structure collapse (Figure 1.2).

Under the Poisson assumption, the probability of failure in a time interval $[t, t + \Delta t]$ may be estimated by:

$$P_f[t, t + \Delta t] = 1 - e^{-\lambda_f \Delta t} \qquad (1.5)$$
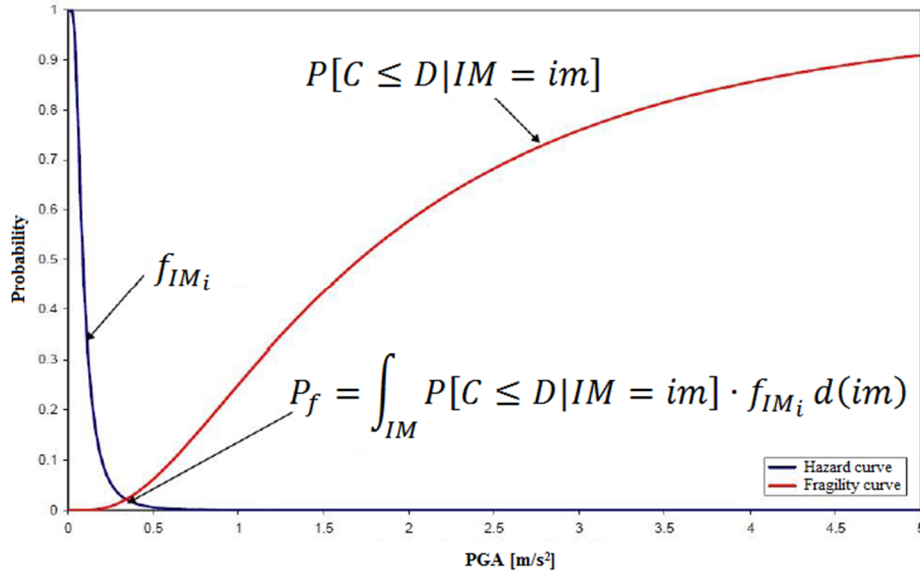
Figure 1.2 – Graphic illustration of Equation 1.4

Equation 1.5 describes a quantitative relationship between seismic hazard (that is, an earthquake of intensity *IM* or larger with an average recurrence interval or frequency) and seismic risk (namely, a probability P_f that an earthquake of intensity *IM* or larger might occur during an exposure time Δt for a given vulnerability). Equation 1.5 is derived from the interactions between the hazard and vulnerability in time and space, taking also in consideration the physical interaction between the hazard and vulnerability. Actually, there is a relationship between ground motion and damage levels (i.e., fragility curve); the damage level may also be related to a level of economic loss. Thus, seismic risk is quantified by four parameters: *probability*, *level of severity* (i.e., a physical or monetary measurement), *spatial* measurement and *temporal* measurement.

1.2.1 *Characterization of seismic hazard*

Seismic hazard studies have been carried out in recent years to analyse local and regional areas with a view to zonation (basic hazard information for seismic classification) or micro-zonation (local hazard information). In the latter case, hazard assessment means identifying areas on a municipal scale that, in the event of a seismic tremor, may be subjected to amplification phenomena and providing data useful for urban planning.

Hazard studies may also be used in site analysis, to locate critical constructions from a point of view of safety, risk or strategic importance (power stations, military installations, hospitals). Hazard assessment in this case means calculating the probability of an earthquake of a magnitude that exceeds specific threshold values, leading to the choice of different areas if necessary.

Hazard assessment may be deterministic or probabilistic. The deterministic method is based on the study of damage observed during seismic events in the past at a given site, reconstructing the damage scenarios to determine the frequency of repetition of tremors of the same intensity. However, since this approach requires complete information to be available regarding local seismicity and its effects, it is generally preferred the probabilistic approach. This expresses hazard as the probability of an event with certain characteristics occurring in a given interval of time. The most frequently used probabilistic method is the Cornell one, which entails identification in the area of the zones responsible for the seismic events (genetic seismic zones), quantification of their level of seismic activity and calculation of the effects caused by these zones on the area in relation to its distance from the epicentre. This way, the assessment of seismic hazard leads to the creation of the hazard curves that, for a given period or peak ground acceleration (PGA), correlate the spectral acceleration with a certain probability of exceedance, which usually refers to a time period of fifty years.

In Italy, the INGV – *Istituto Nazionale di Geofisica e Vulcanologia* (Meletti & Montaldo, 2007) provides the Country's hazard maps (Interactive maps of seismic hazard, http://esse1-gis.mi.ingv.it), which may be referred to every specific site and are related to nine annual average frequencies of exceeding as many PGA and spectral acceleration values, function of ten structural period values (Figure 1.3).
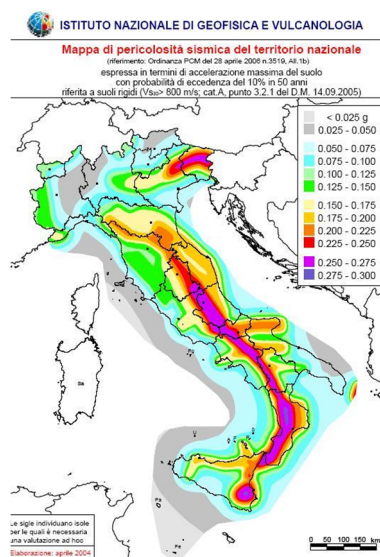
Figure 1.3 – Seismic hazard map of Italy in terms of PGA
with exceedance probability of 10% in 50 years (INGV)

In particular, they have been developed seismic hazard maps in terms of PGA, with probability of exceedance in fifty years amounting to: 81%, 63%, 50%, 39%, 30%, 22%, 10%, 5% and 2%, corresponding respectively to the return periods of 30, 50, 72, 101, 140, 201, 475, 975 and 2475 years. Each processing led to generating the hazard curves that represent the median (50th percentile), the 16th and the 84th percentile of the distribution of the PGA values.

1.2.2 *Characterization of seismic vulnerability*

Seismic vulnerability assessment is an approved process or methodology of evaluating deficiencies in a structure that prevents the latter from achieving a selected performance objective. Therefore, vulnerability relates the intensity of the earthquake and the level of damage to the structural system. The intensity measure *IM* may be identified by means of several parameters, including the peak ground acceleration PGA, the spectral pseudo-acceleration evaluated at the fundamental vibration period of the structure. Anyway, whatever is the selected *IM*, it may describe the earthquake capability to damage a structure. Conversely, the choice of the damage parameter is usually more complex. In a structural analysis the damage may be related to specific limit states by achieving definite levels of displacement or resistance of the structures. At the end of the vulnerability assessment process, it is possible to define a fragility (vulnerability) curve that correlates the structural damage with the *IM*.

In probabilistic terms, the fragility identifies the probability of exceeding a determined limit state given a fixed seismic intensity. Hence, by means of fragility curves, it is possible to detect the intensity of the seismic action which is necessary to cause a certain level of seismic response or damage to the structure. Figure 1.4 shows an example of fragility curves, corresponding to predetermined damage levels, in function of the peak ground acceleration.
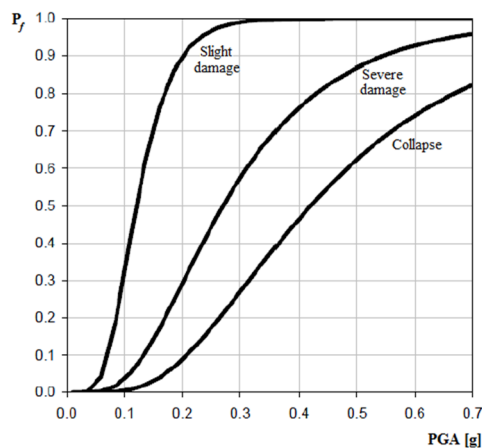
Figure 1.4 – Fragility curves with reference to fixed damage levels

There are several approaches to evaluate seismic fragility: the main two are based on empirical and analytic methods.

Empirical methods

This approach is the most widespread and realistic, as it is based on the statistical analysis of earthquake damage, according to available data of past seismic events (Rossetto & Elnashai, 2003). However, the accuracy of the method may not always be appropriate because of the lack of a sufficiently large database of observations, especially with reference to reinforced concrete structures. Moreover, it is not possible to create fragility curves related to a particular construction, but only to classes of structures, since the empirical methods are based on the definition of classes characterized by typological or functional indicators (Di Pasquale, Orsini, & Romeo, 2005), such as constructive typology, plan morphology, height, year of construction.

Each class may be associated to a probability of damage matrix or a fragility curve. The hypotheses formulated to generate the vulnerability curves or damage matrices are verified by a statistical processing of damage caused by past earthquakes (*a posteriori analysis*).

Analytic Methods

This approach is commonly applied to the calculation of the vulnerability of a single structure, whose level of knowledge is adequate. The fragility curves may be generated by implementing structural analysis with different levels of sophistication: linear, nonlinear, pseudo-static or dynamic analyses. Obviously, the computing time grows proportionally to the accuracy of the results.

The most commonly used analytical approach in fragility studies is based on the nonlinear dynamic analysis, in which damage is associated with the achievement of a limit state that may be identified by the attainment of a limit rotation or a collapse mechanism of the structure, while the action is generally expressed in terms of spectral parameters, such as $S_a(T)$.

1.2.3 *Seismic Reliability*

According to the Italian regulations (Norme Tecniche per le Costruzioni, 2008), the "constructions and structural components shall be designed, constructed, tested and serviced so as to enable them to be used in a way economically sustainable and with the level of security provided by these regulations. The security and performance of a structure or a part of it shall be assessed in relation to the limit states that may occur during its nominal life. *Limit state* identifies the condition over which the structure no longer meets its design criteria". Hence, the structural reliability, also known as the probability of success, may be defined as the probability, in a predetermined period of time, that the structure will continue to perform the functions for which it was designed and constructed. In other words, it may be expressed as the probability that the useful life of the structure is not less than a specific value of the design nominal life. Consequently, a construction may be considered reliable if the probability P_s that it performs its functions throughout its useful life will be greater than a predetermined acceptance value P^*.

Evaluation of seismic reliability

The assessment of the structural seismic reliability may not generally be carried out by means of a simple deterministic approach, since it is necessary to take into account that the level of protection concerning the performance limit states may be expressed only in probabilistic terms, i.e., by the probability that any predefined limit state is exceeded at least once during the useful life of the structure. To evaluate the level of protection, given a specific limit state, it shall be checked that the following relation is satisfied:

$$P_f \leq P_f^* \qquad\qquad (1.6)$$

in which P_f^* is a limit value of the probability of failure, representing the accepted risk in relation to the consequences of reaching the considered limit state. Ensuring a high degree of security, and thus minimizing the P_f^* value, means designing more important, then more expensive, structures, so that they may result economically incompatible with their function as well as with the country's economic and development conditions. Therefore, the acceptable value of the probability of failure is not easy to be determined, as it involves not only structural, but also political and financial, competence.

2

Seismic Damage in Bridges and Protective Strategies

In the latest forty years, earthquakes caused severe damages to civil infrastructures all over the world, with an increasing trend. Lots of important bridges collapsed, even if designed to resist seismic actions: this was mainly due to their usual structural simplicity, which makes them be very vulnerable to seismic damaging. Bridges are lifeline structures, thus evaluating their damage is fundamental to assess that of road and highway systems: the related risk is actually calculated with specific reference to the direct damage of bridges and to the delay on travelling time due to bridges' closure.

2.1 *Frequent Seismic Damages and Retrofit Techniques*

The damage due to earthquakes may interest all the structural components of a bridge: in particular, the damages to the deck, which usually has not a pre-eminently aseismic function, are related to cinematic concept errors, which lead to different failure mechanisms (unseating, pounding); conversely, the various types of damage observed on the columns are generally caused by flexural ductility and shear resistance defects.

Seismic retrofitting is the modification of existing structures to make them more resistant to seismic activity, ground motion, or soil failure due to earthquakes. With better understanding of seismic demand on structures and with recent experiences with large earthquakes near urban centres, the need of seismic retrofitting is well acknowledged. Prior to the introduction of modern seismic codes in the late 1960-70's, many structures were designed without adequate detailing and reinforcement for seismic protection.

2.1.1 *Deck – Unseating and pounding*

Deck collapse caused by relative displacement of spans in longitudinal direction was very recurrent, especially in simply supported multispan bridges: in most cases seats and corbels resulted in a scanty length, so that spans became unseated and suddenly collapsed. The following Figures 2.1 and 2.2 show some examples of this type of failure: it is worth noting how the deck remained perfectly intact, as the seismic action does not specifically

harm this structural component of the bridge. Conversely, seats would need to be oversized: in Figure 2.2 – b is depicted the hinge of a new arc bridge, that was cleanly cut due to horizontal seismic actions. In this case there were absolutely inadequate seismic restrainers, consisting of bolts connecting the arch end plates to the transverse beam of the collapsed span.
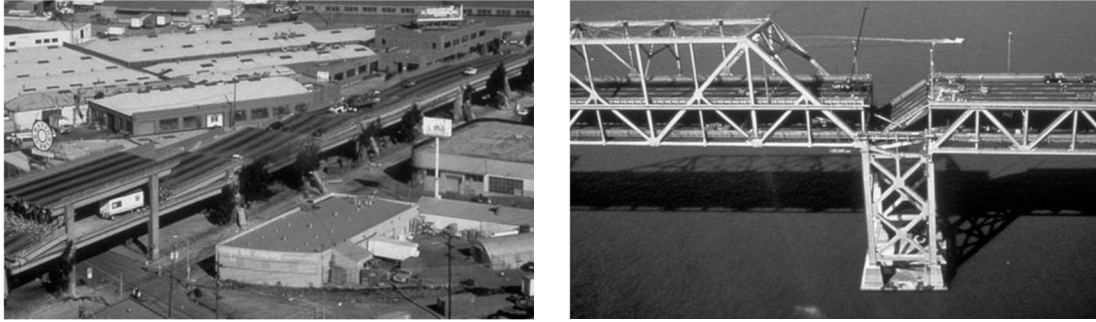
Figure 2.1 – Loma Prieta earthquake, California, USA, 1989: Unseating
a) Cypress Viaduct and b) Viaduct approaching the East Bay Bridge
(Pinto, Franchin, & Lupoi, 2009)

Figure 2.2 – Kobe earthquake, Japan, 1995:
a) Unseating, Nishinomiya-ko Bridge and b) Bearing failure, Higashi-Kobe Bridge
(Pinto, Franchin, & Lupoi, 2009)

When bridges are built on soft or liquefiable soils, their vulnerability exponentially increases. Soft soils generally yield the structural response amplification, so that the loss of support becomes more probable. In the case of saturated sandy silt or silty sand soils, liquefaction may occur and the induced soil movements may push the foundations out of place; if the bridge foundation system is made of piles, their carrying capacity may cease.
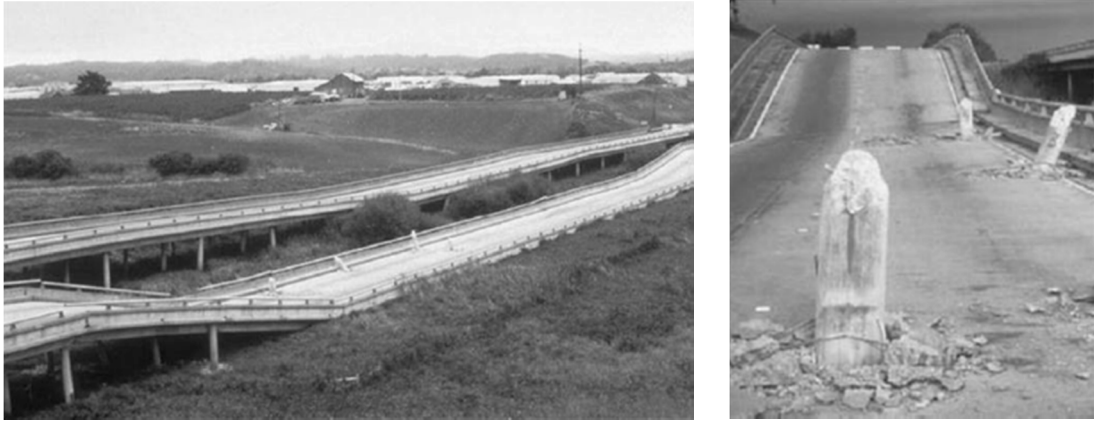
Figure 2.3 – Loma Prieta earthquake, California, USA, 1989, West Grand Viaduct:
a) Soil liquefaction effects and b) Punching of piles through the road bed

When adjacent structural components have different stiffness and the distance among them is not enough to allow their differential displacements, damage may occur due to cyclic pounding (Figure 2.4). Moreover, as the fundamental frequencies may result in out of phase, shear forces and consequent pounding are amplified.

Figure 2.4 – Pounding damage:
a) Kobe earthquake, Japan, 1995, Near Nishinomiya Port
b) Sichuan earthquake, China, 2008, Miao Zi Ping Bridge

2.1.1.1 *Retrofit techniques* (Pinto, Franchin, & Lupoi, 2009)

In many existing bridges with simply supported spans, bearings are placed under every beam and are made of short wide unreinforced neoprene, whose horizontal stiffness is very low: to avoid the deck collapse and contain relative displacements, it may be introduced, on the top of the piers, a system of reinforced concrete restrainers with interposed neoprene bearings (Figure 2.5).
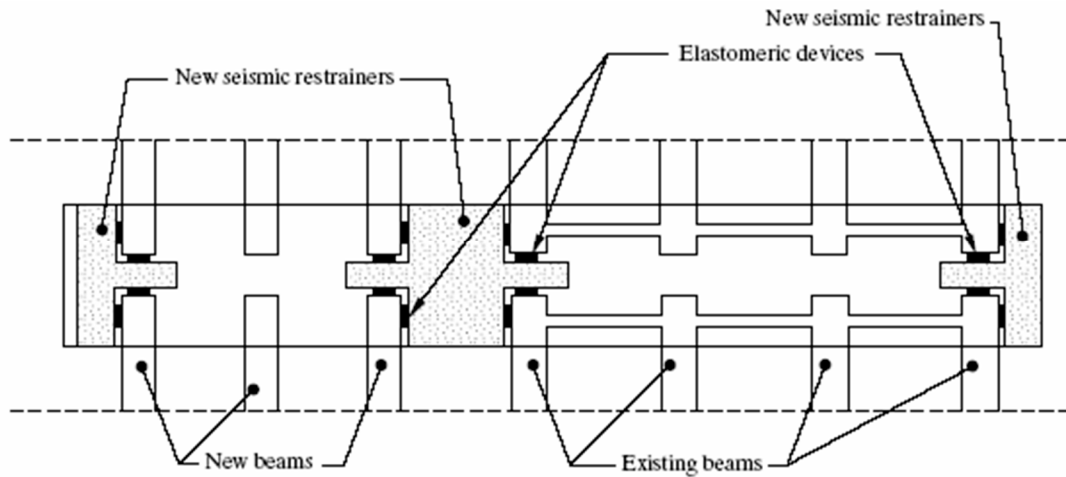
Figure 2.5 – Planimetric view of longitudinal and transversal seismic restrainers
(Pinto, Franchin, & Lupoi, 2009)

Another solution may be the insertion of seat extenders, as those shown in Figure 2.6. They are generally simple and inexpensive to install.

More incisive solutions are those implying the modification of the deck static scheme, from simply supported to continuous: in this case it is not necessary placing the bearings under every beam and the possibility of a loss of support is escaped.

Figure 2.6 – Example of seat extenders

2.1.2 *Columns – Flexural and shear failure*

Bridge's piers often failed after a progressive flexural yielding followed by a cyclic deterioration of the cross section due to insufficient confinement and, consequently, by a decrease of the shear resistance. This collapse mechanism reveals a flexural ductility depletion (Figure 2.7 – a), usually combined with exceeding the shear resistance (Figure 2.7 – b). The shear governed failure, instead, has been rarely observed. The latter is typical in squat piers (Figure 2.8).
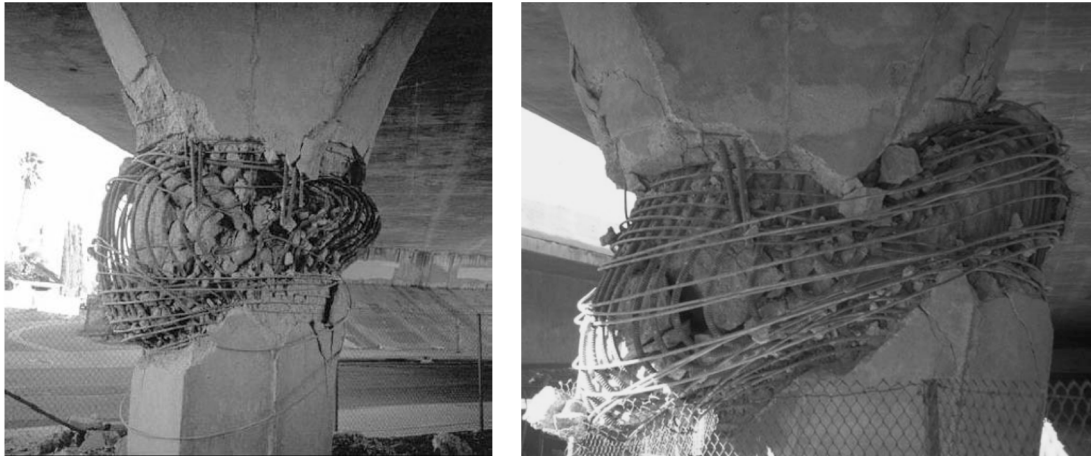
Figure 2.7 – Northridge earthquake, California, USA, 1994, Gothic Avenue Viaduct:
a) Plastic hinge collapse and b) Flexural and shear combined collapse
(Pinto, Franchin, & Lupoi, 2009)

Figure 2.8 – Chi Chi earthquake, Taiwan, 1999, Wushi Viaduct: column shear failure
(Pinto, Franchin, & Lupoi, 2009)

These failures lead to high residual deformations and so, especially if the deck is very broad and supported by a single line of piers, a complete collapse caused by the loss of equilibrium may occur, also due to the high moment of inertia generated by the deck rotation (Figure 2.9).

Figure 2.9 – Kobe earthquake, Japan, 1995, Hanshin Viaduct (Pinto, Franchin, & Lupoi, 2009)**:**
a) collapse due to loss of equilibrium and b) column failure detail

A further vulnerable element in framed piers is represented by the inadequate dimensioning of the beam-column joints, which are very sensitive to shear failure (Figure 2.10).

Figure 2.10 – Kobe earthquake, Japan, 1995, Shinkansen Viaduct (Pinto, Franchin, & Lupoi, 2009)

2.1.1.2 *Retrofit techniques* (Pinto, Franchin, & Lupoi, 2009)

In reinforced concrete columns not designed basing on earthquake engineering concepts, the overlap and anchorage lengths of longitudinal bars and the quantitative of transversal reinforcement have been usually resulted insufficient. Both concrete and compressed longitudinal bars confinement was inadequate and taut longitudinal bars also slipped off, as consequence of a lack of shear resistance and ductility.

The most settled retrofitting strategies aiming to avoid these problems are:

- Concrete, steel or composite materials jacketing;
- Modification of the pier static scheme by introducing shear walls or additional columns.

Concrete jacketing

Concrete jacketing technique consists in creating a new reinforced concrete section around the existing pier (Figure 2.11 – a). It is fundamental creating an appropriate connection between the two parts of concrete, by means of a set of bars inserted in apposite holes, which are made in the existing concrete after removing the reinforcement cover and injected with cement mortar or epoxy resins (Figure 2.11 – b). The jacket may be (a) detached from the base, about 100-150 mm, providing an increase in ductility and shear resistance, or (b) connected to the foundation through longitudinal bars, providing in this case also a contribution to the flexural strength. The increased confinement improves both the behaviour of the compressed concrete and the force transmission in the overlapping zone among the bars. In case (b), as usual jacket thickness is between 200 and 300 mm, the increase in flexural strength may be important and the foundation may result inadequate to the new forces transmitted by the column: that's why the first option is more widespread, but, if foundations are able to exert higher resistance, the second option may be advantageous in limiting plastic deformations.

a) Circular cross section   b) Rectangular cross section
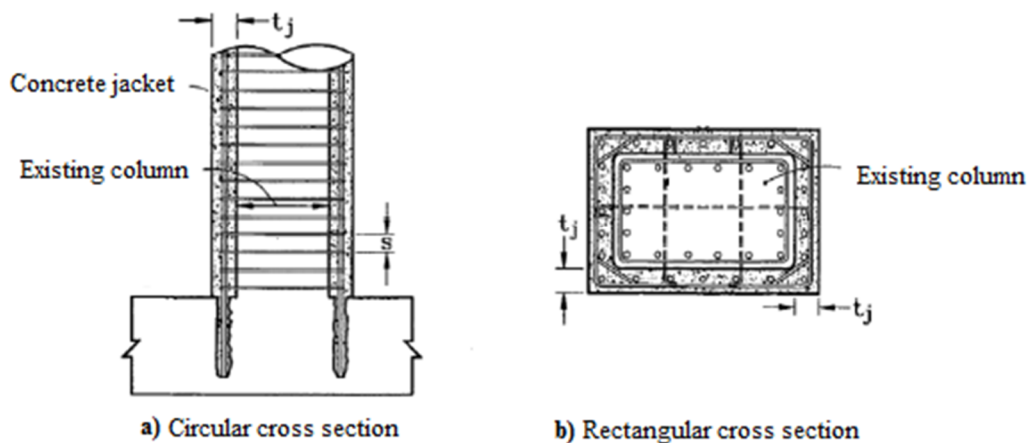
Figure 2.11 – Concrete jacketing technique (Pinto, Franchin, & Lupoi, 2009)

Concrete jacketing is very effective for circular sections, while for rectangular ones its efficiency is inversely proportional to the size of the cross section. This problem particularly affects diaphragm piers jacketing, as they may show a lack of resistance, despite the large section, caused by their usual reduced reinforcement. In such cases, the two jacket sides should be connected by means of bars crossing the existing section, parallel to the short side: these bars are usually located at a distance of 300-400 mm in the vertical direction and 1.0 m in the transverse one. It is worth pointing up that during the drilling operation to insert the bars, the existing reinforcement might be intercepted: recently, they have been developed some techniques in which lower diameter bars, even made of innovative materials such as aramid fibre-reinforced polymers, are used.

Steel jacketing

This technique is one of the first used in seismic retrofitting of reinforced concrete columns with rectangular cross section, by means of circular or elliptical jacketing forms. It was employed for thousands of bridge piers in California, after the Loma Prieta earthquake in 1989, and proved to be very effective during the Northridge earthquake in 1994 (Figure 2.12): over fifty bridges have not suffered any sort of damage to the columns, even for peak ground accelerations above 0.3*g*.

Figure 2.12 – Steel jacketing of pier:
Northridge earthquake, California, USA, 1994, Santa Monica Highway

Jacketing thickness is usually in the range of 6 ÷ 12 mm, while that between it and the pier is about 12.5 ÷ 25 mm, and it is injected with cement mortar or resins (Figure 2.13 – a). Steel jacketing may be jointed through in situ welding or mechanical joints as shown in Figure 2.13 – b. As for concrete jacketing, the best results are obtained in the case of circular full cross sections, even if the efficiency of this technique has not yet been experimentally supported for piers whose diameter is higher than 4.0 m.

Since the required quantity of steel is considerable, steel jacketing may be economically less competitive, but it is noteworthy that this solution provides a very high increase in flexural and shear resistance. In particular, to increase the flexural strength it is necessary anchoring the jacket to the foundation, by means of anchor bolts connected to steel profiles welded to the base (Figure 2.13 – d). For rectangular piers, elliptical jackets have effect on shear and flexural resistance (Figure 2.13 – c-d), but not on confinement.
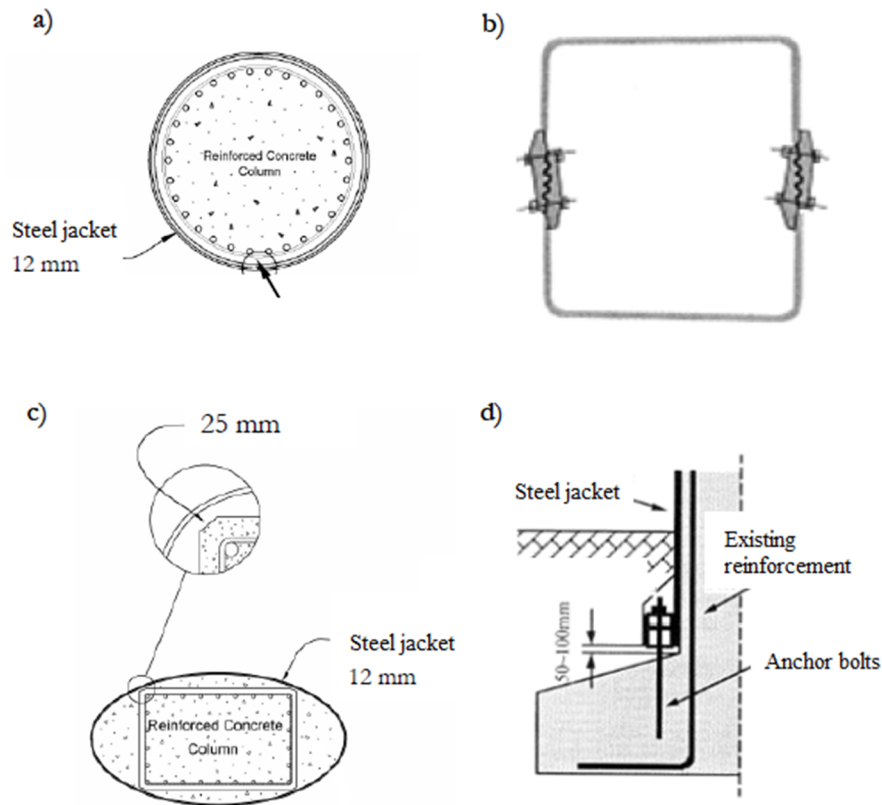
Figure 2.13 – Steel jacketing technique (Pinto, Franchin, & Lupoi, 2009)

Composite materials jacketing

Many fibre-reinforced polymers may be used in this type of jacketing, such as carbon, aramid or glass fibres; the choice depends on stiffness, resistance and deformation to failure of the specific material. If the purpose is to improve the confinement, the most suitable fibres are carbon ones, which are characterized by the highest elastic modulus (comparable to steel) and by a linear elastic behaviour until failure. Moreover, carbon fibres resistance is about ten times higher than that of ordinary reinforcement steel. Confinement is therefore more effective than that offered by transverse reinforcement, as the lateral expansion of concrete is elastically controlled even at very high deformation levels.

These materials are supplied in sheets, which are usually placed transversally to the column axis, to improve confinement and shear resistance. Besides, they might also be positioned parallel to the pier axis and anchored by steel plates to the foundation, to increase flexural resistance (Figure 2.14). For rectangular sections, a solution similar to that of steel jacket (Figure 2.13 – c) has also been adopted to increase the effectiveness of confinement (Figure 2.15).
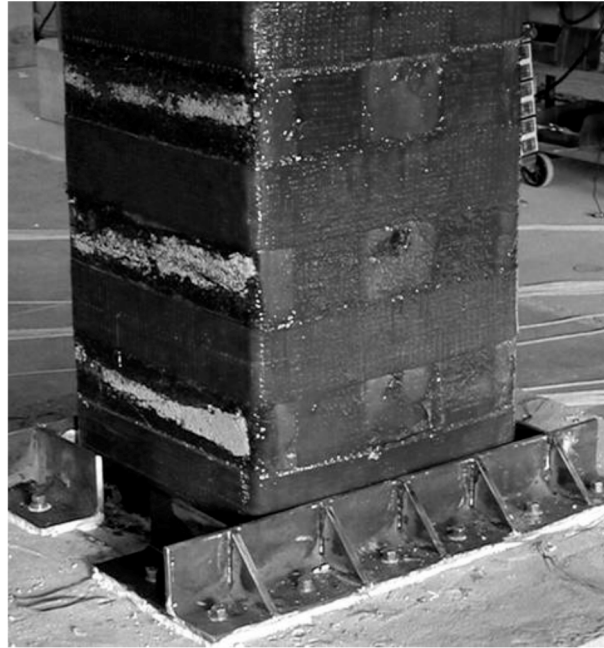
Figure 2.14 – Carbon fibre-reinforced jacketing
(EUCENTRE experimentation, DPC-Reluis - Line 3 Project)
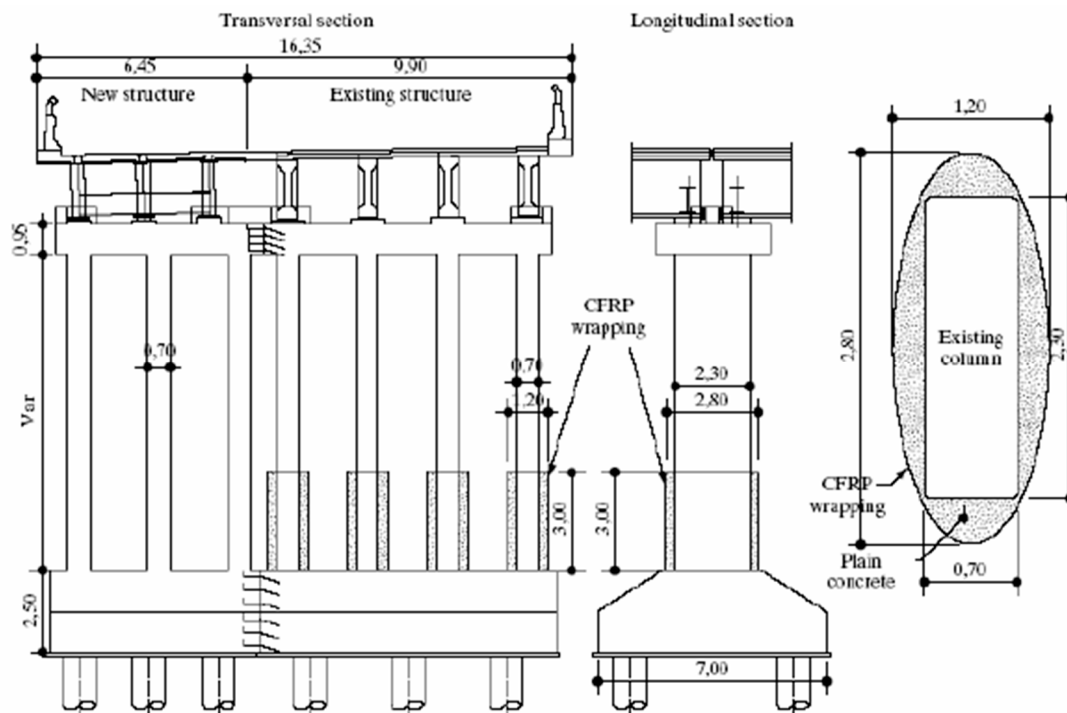
Figure 2.15 – Carbon fibre-reinforced jacketing with previous elliptical section creation
around the existing one (Pinto, Franchin, & Lupoi, 2009)

For columns with slightly variable cross section, the most suited jacketing material is aramid, whose fibres are less rigid than those of carbon. Aramid fibres may be supplied in sheets and bars: in particular, the sheets are used in jacketing and the bars to prestress the foundations (§ 2.1.4) or as connection between the sides of concrete jackets in the case of rectangular piers.

Furthermore, jacketing may be carried out through glass fibres mixed with resins. Similarly to the *shotcrete* construction technique, this material is pneumatically projected onto the column surface, on which a welded mesh is also arranged. This solution has been subjected to cyclic testing which gave good results in terms of increase in ductility.

Transformation into diaphragm column

In some cases of short framed columns it may be constructed a reinforced concrete wall among the two piers, the foundation and the cup beam. The new concrete casting is connected to the existing column by means of steel bars. It results a diaphragm column with very high stiffness and strength in the plane of the new wall (Figure 2.16).
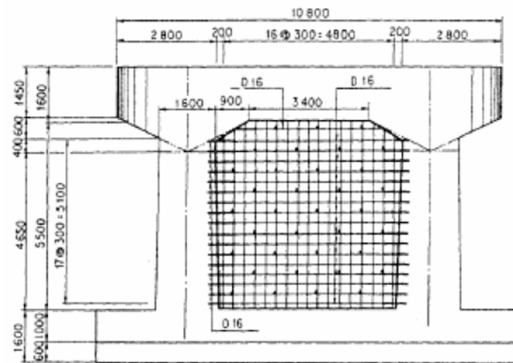
Figure 2.16 – Transformation into diaphragm column (Pinto, Franchin, & Lupoi, 2009)

Vertical prestressing

Vertical external prestressing of columns is very suitable in the case of cellular cross sections, as the cables may be easily arranged within the section. The prestressing action may be modulated along the pier, taking care to avoid abrupt changes in stiffness or unintentional shifts of the plasticization zones.

2.1.3 *Abutments*

In Italy, the most frequently used typologies of abutments in existing bridges are the gravity one, in non-reinforced concrete, and the cantilever one, in reinforced concrete.

As abutments are subjected to ground thrusts (Figure 2.17), which are amplified during seismic events, the contact between the superstructure and the top of the abutment restricts the movements inwards. Consequently, the rotation and collapse of the upper wall may occur (Figure 2.18). Large rotations of the abutment may also cause damage to the deck support system.
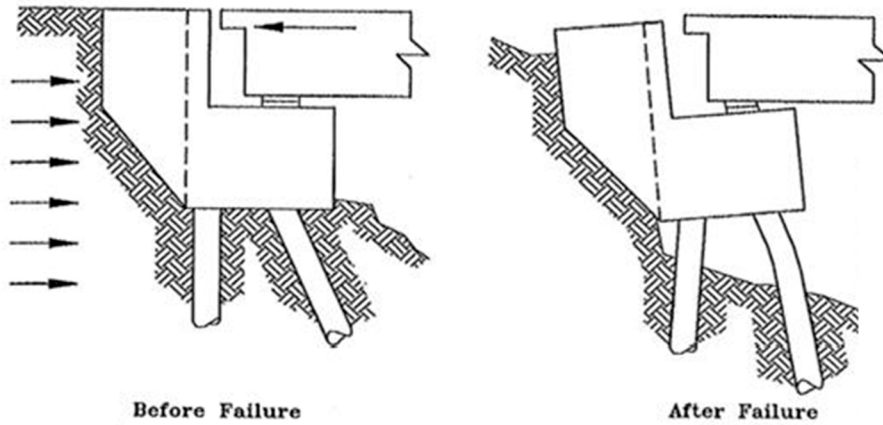
Figure 2.17 – Abutment failure due to seismic action

Figure 2.18
a) Abutment collapse: Northridge earthquake, California, USA, 1994, Granada Hills
b) Abutment shift: Kobe earthquake, Japan, 1995, Near Nishinomiya Port
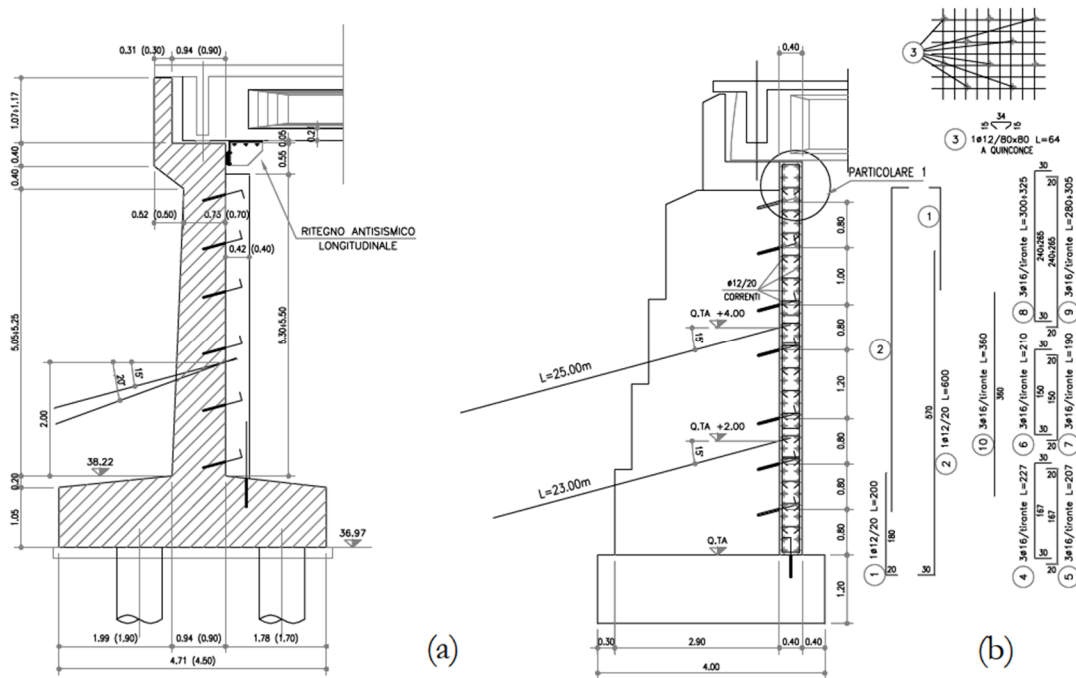
Figure 2.19 – Abutment retrofitting: a) cantilever abutment and b) gravity abutment
(Pinto, Franchin, & Lupoi, 2009)

The most common retrofitting technique to solve the problems of global stability is the positioning of tie rods, whose internal actions are distributed on the abutment's face by means of an additional reinforced concrete jacket. It may be arranged a succession of tie rods in the case of gravity abutments, as they exhibit a flexural strength deficit even above the base section (Pinto, Franchin, & Lupoi, 2009). These solutions are shown in Figure 2.19.

Another solution to reduce the ground thrusts on the abutment's face consists in replacing the overleaf filling material with a lower weight one, characterized by better mechanical characteristics (Pinto, Franchin, & Lupoi, 2009).

2.1.4 *Foundations*

Collapse in foundations due to seismic actions occurred in relatively few cases, because they are not the weakest structural component and their collapse is preceded by the piers flexural or shear one. Nevertheless, an underestimated design seismic action may cause the foundation failure (Figure 2.20).

Figure 2.20 – Foundation collapse: Chi Chi earthquake, Taiwan, 1999

Enhancements on foundations may be required if the existing foundation is not adequate to transmit to the ground the forces exerted by the superstructure, as the actual seismic action is usually higher than that of the first design. Furthermore, if the pier or abutment have been seismically rehabilitated, it is necessary to verify that the foundation is able to resist the new increased forces. In any case, if the pier has been extended to accommodate a wider deck, the foundation has to be properly adapted (Pinto, Franchin, & Lupoi, 2009).

The new part of the foundation is usually a plinth based on micro-piles. The main problem is to make the two portions of the plinth collaborate, in order to guarantee a monolithic behaviour. The most common solution is to dispose a dense arrangement of steel bars. In the case of elevated internal actions it is possible to resort to transverse prestressing.

Figure 2.21 shows the seismic retrofitting of the foundation of an enlarged viaduct: in such cases the micro-piles should be designed to provide vertical and rotational stiffness (against rotation around the bridge cross-axis) comparable to those of the existing part.
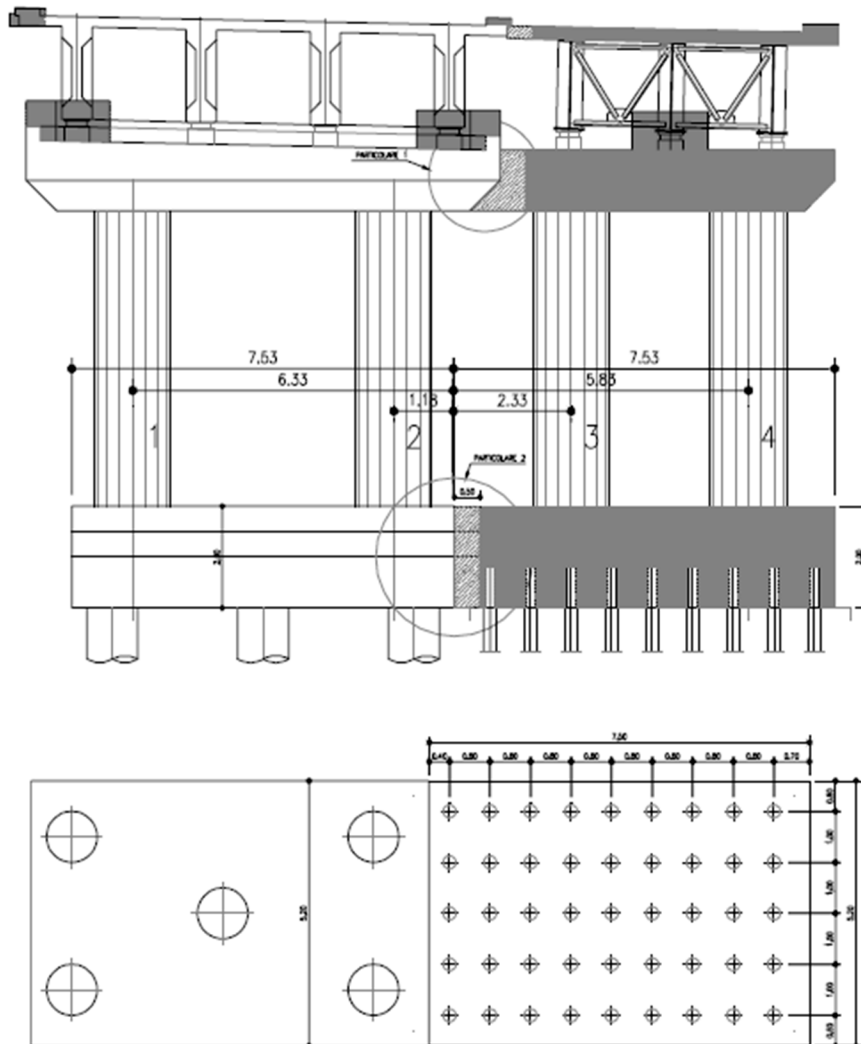
Figure 2.21 – Foundation of an enlarged viaduct (Pinto, Franchin, & Lupoi, 2009)

2.2 *VIBRATION CONTROL TECHNIQUES*

To prevent structural damage due to seismic actions, a different approach, for both existing and new constructions, is that based on the vibrations control: the structural dynamic response is artificially regulated by means of not exactly structural devices, to reduce the vibrations induced by earthquakes.

At first, it may be considered an input-output relation as that represented in Figure 2.22:
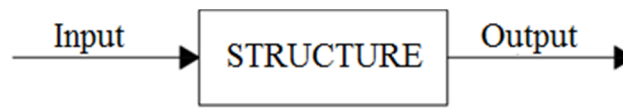
Figure 2.22 – Conventional structure

This system may be modified, in order to control the input or the response, by adding an external element, called *controller*. In earthquake engineering, this concept is applied in the so-called *Vibration Control* methods.

The *Vibration Control* systems may be classified into two categories (Palazzo & Petti, 1995):

- Open-cycle systems, in which the controller lies between the input and the structural system; it seems like a filter that, interposed between the ground and the structure, modifies the energy transmitted by the input signal. The control action is independent from the output.

- Closed-cycle systems, which instead are influenced by the response of the system. The controller receives the output information, i.e., the structural response, and then it modifies the way as the structure perceives the input signal, so that it may be considered to perform a feedback action. The advantage is that the structural response may be monitored, but the input data may not be controlled.

Figure 2.23 – Open-cycle system
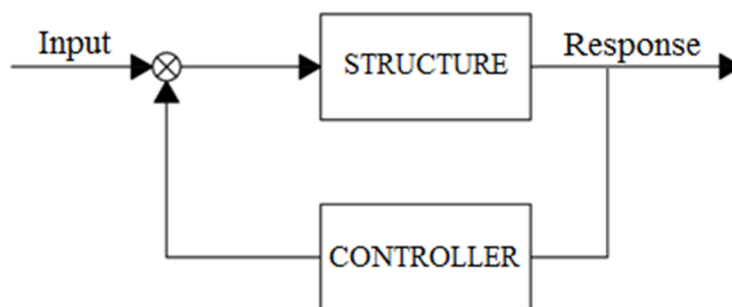
Figure 2.24 – Closed-cycle system

2.2.1 *Vibration Control strategies*

Several *Vibration Control* approaches have been developed and implemented on different structures, such as tall buildings, long bridges and wind turbines, to reduce vibration induced by different external excitations. The principal *Vibration Control* techniques are:

- Passive control;

- Active control;

- Semi-active control;

- Hybrid control.

The passive control method is simple and reliable. This control method provides for the introduction of additional elements (PED) that change the seismic behaviour without requiring external forces. The passive control system may include sensors to measure the excitation amplitude. Since there are no external control forces, the vibration amplitude is minimized by controlling internal forces provided by the motion of the points of attachment (Constantinou, Soong, & Dargush, Passive Energy Dissipation Systems for Structural Design and Retrofit, 1998). Figure 2.25 shows the basic structure of passive vibration control approach: this system may be classified as an open-cycle control one.
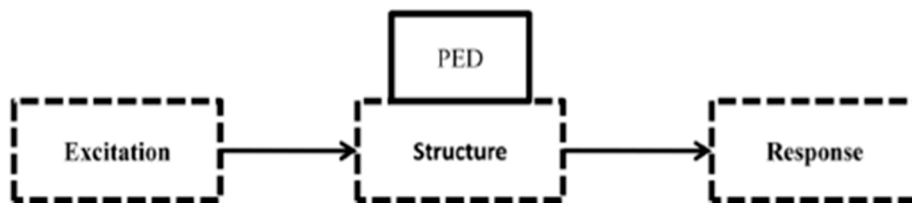
Figure 2.25 – Structure with Passive Energy Dissipation (PED)
(Rahman, Ong, Chong, Julai, & Khoo, 2015)

The principal passive control techniques include:

- *Seismic isolation* (Figure 2.26 – b), that consists of inserting a low horizontal rigidity element between the ground and the structure in order to uncouple their motion;

- *Additional energy dissipation* (Figure 2.26 – c), in which damping devices, in addition to the bracing elements, are introduced in order to dissipate energy through their hysteretic, frictional and viscous behaviour;

- *Tuned mass damper* (Figure 2.26 – d): additional masses, moving in phase-opposition with the structure, are used to contain the displacements.
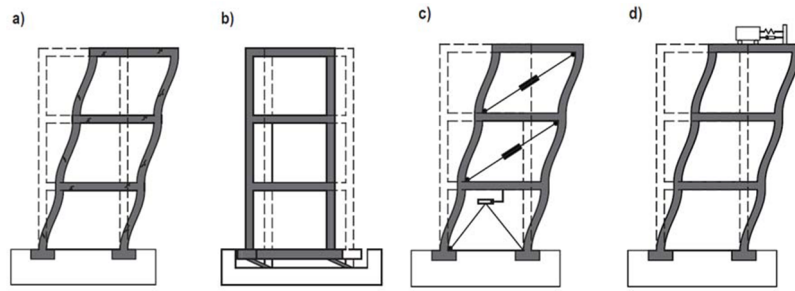
Figure 2.26 – a) Non-protected structure; b) Seismic isolation;
c) Additional energy dissipation; d) Tuned mass damper (Foti D. & Mongelli M., 2011)

The active control system consists of force delivery devices, real-time data processors and sensors. The input control forces are provided based on the acquired information from sensors that measure the excitation input and the response of the system structure. Real-time data computers process the information and calculate the necessary force to counter the measured vibration amplitude. The control forces are generated by electro-hydraulic actuators which require large power sources. External actuators provide required forces to mitigate the structural vibration (Figure 2.27).
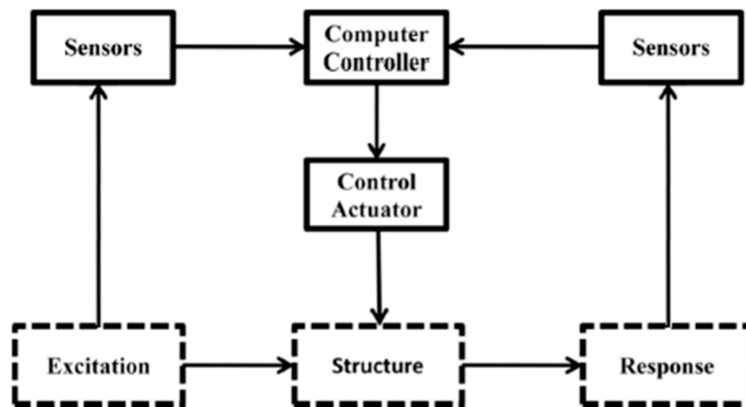
Figure 2.27 – Structure with active vibration control (Rahman, Ong, Chong, Julai, & Khoo, 2015)

Figure 2.27 shows the basic scheme of active vibration control approach: under excitation, the structural behaviour is measured through sensors and the processors provide the required force to control actuator. Then the control actuator inputs required force to minimize unwanted amplitude of the structure (Rahman, Ong, Chong, Julai, & Khoo, 2015). Hence, the functioning may be schematized as that of a closed-cycle system.

Semi-active vibration control systems combine the advantages of active and passive control ones (Figure 2.28). Compared to the passive control method, where the control forces are developed from the motion of the structure itself, appropriate adjustable mechanical devices are used to provide control forces. Therefore, semi-active devices are often called as

controllable passive devices (Chu, Soong, & Reinhorn, 2005). Besides, the structure of a semi-active control system is quite similar to that of the active control one, except the external control force. Semi-active control approach appears to be most attractive nowadays for its nature of structure which offers reliability of passive and adaptability of active devices (Rahman, Ong, Chong, Julai, & Khoo, 2015).
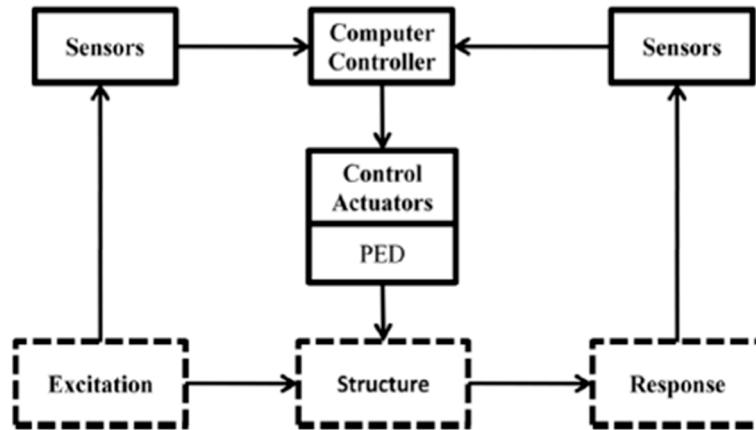
Figure 2.28 – Structure with semi-active vibration control
(Rahman, Ong, Chong, Julai, & Khoo, 2015)

Finally, the hybrid vibration control is based on applying an active control system to a passive control one, as shown in Figure 2.29. Consequently, to achieve the same performance of an active control system, the hybrid one needs less strength and energy.
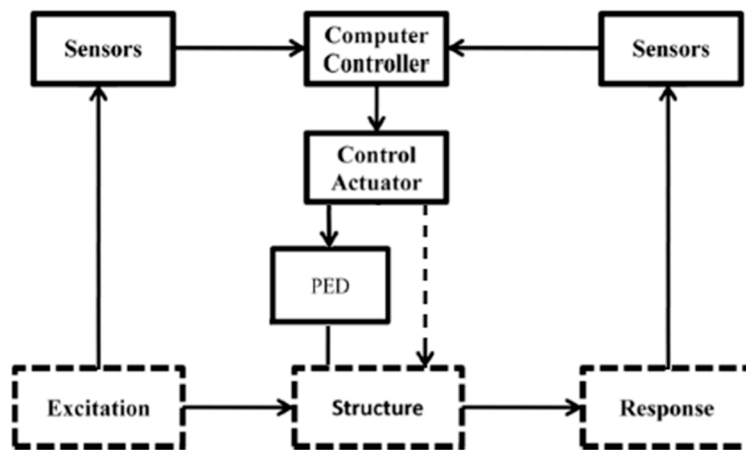
Figure 2.29 – Structure with hybrid vibration control

The following Table 2.1 shows the knowledge and development level of the previously mentioned *Vibration Control* techniques.

Vibration Control method	Scope	Maturity degree
Seismic isolation	Medium height buildings	• Mature technique • Many experimental results and data • Many applications over the world
	Bridges and civil infrastructures	
	Instrumentation and devices	
Additional energy dissipation	Medium height/tall buildings	• Mature technique • Many experimental results and data • Many applications over the world
	Towers, poles, chimneys	
	Long span bridges and civil infrastructures	
Other types of passive control	Medium height/tall buildings	• Relatively mature technique • Many experimental results and data • Many applications over the world
	Towers, poles, chimneys	
	Long span bridges and civil infrastructures	
Active, semi-active and hybrid control	Tall buildings	• Mature technique • Many theoretic results • Some applications over the world
	Towers, poles, chimneys	
	Long span bridges and civil infrastructures	

Table 2.1 – Vibration Control strategies

It may be seen that *seismic isolation* and *energy dissipation* have emerged as the most promising techniques for retrofitting strategies to improve the seismic performance of existing structures, but they also represent a practical solution for new construction, when conventional design is not suitable or economical. The improved performances justify the possible greater costs due to the devices design and installation; however, a lower request of strength and rigidity to the structure generally compensates for this rise in costs.

This thesis aims at analysing the parameters governing the behaviour of a particular type of isolating devices, namely the Friction Pendulum bearings. The seismic isolation principles will be presented in the following Chapter 3.

3

SEISMIC ISOLATION OF BRIDGES AND FRICTION PENDULUM DEVICES

Isolation technique provides an alternative approach for seismic design of many new bridges as well as a convenient way to upgrade the existing ones. The main function of the isolation technique is to decouple the structure from the support. When appropriate, the use of special energy dissipating devices between the superstructure and the substructure may significantly reduce the forces induced in the bridge structure as compared to non-isolated bridges. The flexibility of the bearing pads causes a period shift for the structure normally to the longer period range. Some isolating systems also provide energy dissipation mechanisms through the hysteresis behaviour of the bearing. Furthermore, most isolating devices may be easily replaced after a damaging earthquake by jacking up the superstructure. With seismic isolation, the bridge piers may be designed to remain elastic during a severe earthquake and at the same time achieve an economic design.

3.1 *SEISMIC ISOLATION PRINCIPLES*

Seismic isolation aims at improving the structural response to the horizontal earthquake actions. The reduction of the response may be achieved:

- by lengthening of the fundamental period of the structure, which reduces forces but increases displacements;
- by increasing the damping, which reduces displacements and may reduce forces;
- preferably, by a combination of the two previous effects.

The first principle is to create a structural discontinuity which allows large relative horizontal displacements between the upper part, defined as *superstructure*, and the lower one, called *substructure*, so that the superstructure mass is uncoupled from seismic ground motions. The super- and substructure are connected by means of special types of bearings, known as seismic isolation bearings, which are placed below the superstructure and on top of the substructure and show a very low horizontal stiffness.

Since the energetic content of seismic excitations is very high for frequency values near to those characterizing the dynamic behaviour of multispan bridges (the typical range is 1-10 Hz), the aim is reducing the oscillation frequencies, that is, elongating the fundamental period of the structure. Usually, multispan bridges are characterized by period values in the range from 0.2 s to 1.2 s: the introduction of isolating devices provides a period increase to values higher than 2 s and even about 4 s.

By uncoupling the superstructure from the substructure, their dynamic behaviour results diversified: the substructure undergoes modest deformations, the more its rigidity is; on the other hand, the more the isolators are flexible, the larger are the oscillations that the superstructure is subjected to. In fact, nearly all of the displacement will typically occur over the height of the isolators and not in the super- or substructure.

Usually, during an earthquake, the larger the oscillations caused by the isolators' displacements, the lower the consequent accelerations and inertia forces transmitted to the superstructure. Therefore, seismic isolation would be more efficient if the superstructure was subjected to lower and lower accelerations; if so, two main kinds of benefits would arise:

- direct benefits to the superstructure, being the inertia forces acting on it greatly reduced;
- indirect benefits to the substructure, because the inertia forces transmitted to it by the superstructure are restrained.

In bridges, seismic isolators are typically installed between the deck and the supporting structures (piers and abutments): under normal conditions, these bearings behave like conventional ones; however, in the event of a strong earthquake, they add flexibility to the bridge by elongating its period and dissipating input energy. This permits the superstructure to oscillate at a lower frequency than the piers, resulting in large relative displacements across the isolator interface. However, these large displacements may be controlled by incorporating damping elements in the bearing or by adding supplemental dampers. Generally, the reduction of seismic actions induces its major benefits to piers and abutments (indirect benefits to the substructure); in continuous deck bridges, a proper calibration of the mechanical characteristics of the isolation system may control the distribution of the reduced lateral forces among the substructures and foundations, to further enhance the overall economy and effectiveness of new and retrofit designs.

Seismic isolation effects may be easily explained referring to elastic response spectra in terms of accelerations and displacements, for different damping levels, as shown in the following Figure 3.1:

(a) Lengthening of period (and dissipation)

(b) Limitation of force (and dissipation)
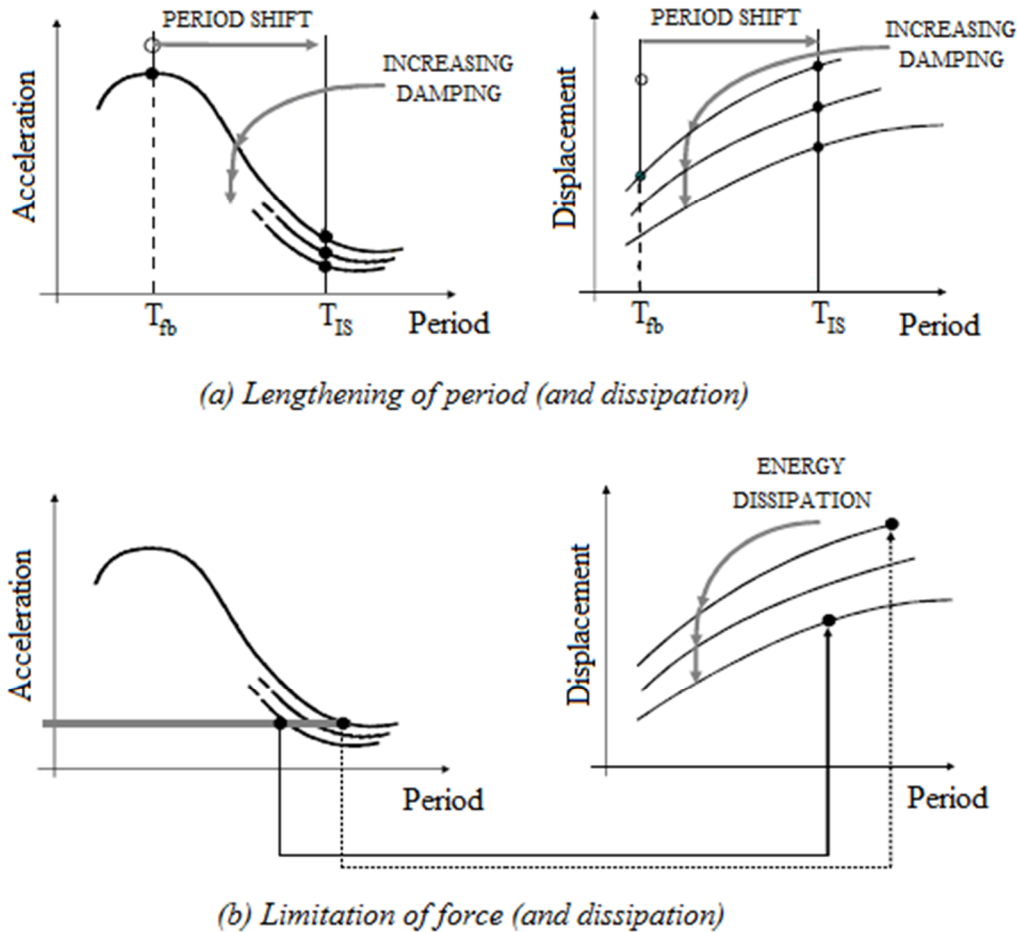
Figure 3.1 – Seismic demand reduction strategies by isolation
(Norme Tecniche per le Costruzioni, 2008)

Seismic isolation systems provide a horizontal isolation from the effects of earthquake shaking and an energy dissipation mechanism to reduce displacements. Actually, considering a fixed-base structure with fundamental period T_{fb}, its isolation from ground motions should generate one of the following effects:

- the elongation of the isolated structure's fundamental period (period shift in Figure 3.1 – a, from T_{fb} to T_{IS}), which may substantially reduce, by a factor exceeding three in most cases, the accelerations that may develop in the superstructure. Such significant reductions in force enable the cost-effective construction of structures that respond in the elastic range (no damage) in design earthquake shaking. In terms of displacements, the period shift leads the isolated structure in the range corresponding to higher displacements, which anyway occur over the height of the isolators;

- the limitation of the force transmitted to the substructure, by using devices with non-linear behaviour characterized by low hardening, that is, very low increase of force for large displacements. In this way the inertia forces, and thus the accelerations, acting on the superstructure are reduced, again at the expense of an increment in the isolators displacements.

The increase in displacement response associated with the use of seismic isolators has, in particular, a deleterious impact on expansion joints in bridges. These large displacements may be controlled by incorporating damping elements in the bearing or by adding supplemental dampers. This is particularly useful for very high seismicity sites or in presence of subsoils with poor characteristics, i.e., types soil C, D, E (Norme Tecniche per le Costruzioni, 2008): in these cases, in fact, the response spectra may show high displacements and accelerations even for high oscillation periods.

In conclusion, there are several conditions that, alone or together, may lead to the use of seismic isolation in a bridge:

- to avoid brittle failure in some piers;
- to avoid concentration of damage in non-regular bridges (e.g. continuous bridges with piers of significantly different height);
- to reduce spectral accelerations in very stiff piers;
- to increase the energy dissipation capacity of the bridge in order to reduce strength and displacement demands of piers.

Clearly, the first two conditions mainly apply to the retrofit of existing bridges, while the latter two are better related to the design of new bridges. In principle, the design of a seismically isolated bridge is simpler than the design of a conventional bridge, as all the structural members (excluding the isolation system) may be assumed to behave elastically. On the other hand, this condition makes the *Capacity Design* approach of conventional bridges inadequate for the design of the isolated ones: alternative design procedures are then needed. When designing an isolated bridge, its geometry and the pier and deck sections are usually known, as they result from non-seismic load conditions. Thus, the pier strength and the characteristics of the isolating system are the only design variables. When dealing with the retrofit of existing bridges, the pier reinforcement is also known and the characteristics of the isolating system become the only design variables.

3.2 FRICTION PENDULUM DEVICES

Friction Pendulum Systems (FPS) are particular types of seismic isolators, which allow relative displacements between the super- and substructure by means of spherical surfaces.

The working principle of FPS is simple (Figure 3.2): a spherical bearing surface identifies a pendulum system whose fundamental period is related essentially to the length of the pendulum itself, i.e. the radius of curvature of the spherical sliding surface. This period represents that of the isolated structure and is independent of its weight. The energy dissipation is provided by the friction encountered during the movement of the sliding surfaces. Hence, the dynamic response of these devices is strictly related to their frictional behaviour.
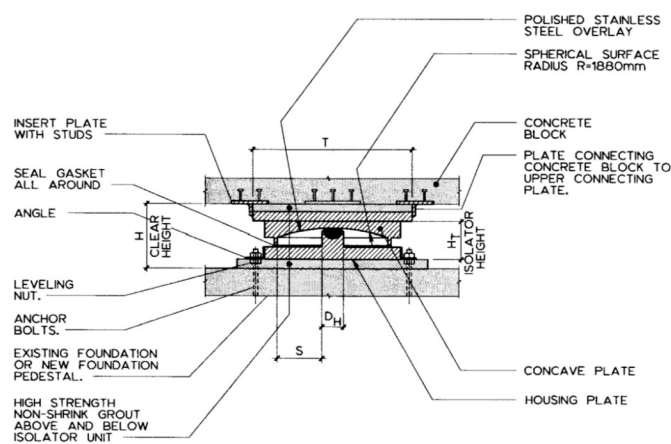
Figure 3.2 – Cross section of FPS bearing

The system is activated only when horizontal forces exceed the static value of friction. Once set in motion, the device develops a lateral force equal to the combination of the requested frictional force and the restoring one along the spherical surface.

FPS may be designed in two main types, with one or two primary spherical sliding surfaces that accommodate the horizontal displacement, respectively classified as single concave and double concave FPS (DCFP).

Single concave FPS (Figure 3.3 – a) are characterized by:

- a concave slider, whose curvature radius imposes the period of oscillation and that accommodates horizontal displacement;
- a base element with a secondary concave sliding surface which permits the rotation;
- a steel intermediate element with two convex surfaces suitably shaped to be coupled with the other two elements.

The device may also be installed upside-down, i.e. with the main concave slider at the bottom.

Double concave FPS (Figure 3.3 – b) are characterized by two primary concave sliding surfaces with the same radius of curvature; both surfaces accommodate horizontal displacement and rotation. In this case each single sliding surface is designed to accommodate only half of the total horizontal displacement, so that the device dimensions in plan may be significantly smaller in comparison with single FPS. Another advantage of DCFP is that eccentricity of the vertical load is halved, i.e. is equal to half the displacement, while in single FPS it is equal to the displacement.
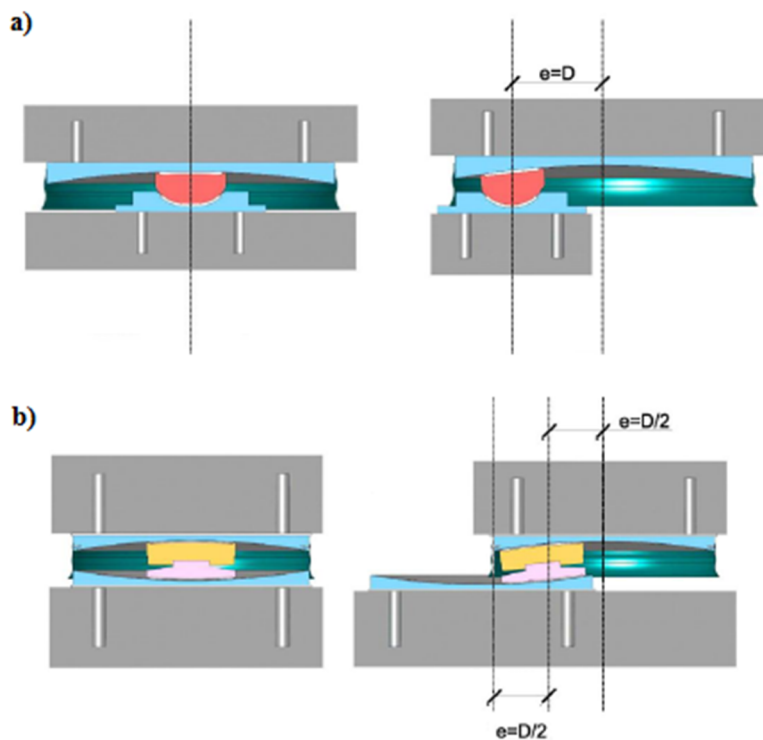
Figure 3.3 – Friction pendulum devices: a) single concave FPS and b) double concave FPS

The most employed sliding surface materials are stainless steel and Polytetrafluoroethylene (PFTE or Teflon®). The use of PTFE is convenient because of low maintenance costs, as it deteriorates only when the system is in motion.

3.2.1 *Dynamic behaviour*

Sliding devices with a flat sliding surface (Figure 3.4 – a) limit the force transmitted to the superstructure to:

$$F_{max} = \mu_d N_{Sd} \text{sgn}(\dot{d}_b) \tag{3.1}$$

where:

- μ_d is the dynamic friction coefficient;
- N_{Sd} is the normal force through the device, i.e. the superstructure weight $W = m_d g$;
- $\text{sgn}(\dot{d}_b)$ is the sign of the velocity vector, being d_b the relative displacement of the two sliding surfaces.

Such devices however may result in substantial permanent displacements. Therefore they should be used in combination with devices providing adequate restoring capability.

Contrary, sliding devices with a spherical sliding surface of radius R_b (Figure 3.4 – b) also provide a restoring force at displacement d_b, so that the force – displacement relationship is:

$$F_{max} = \frac{N_{Sd}}{R_b} d_b + \mu_d N_{Sd} \text{sgn}(\dot{d}_b) \tag{3.2}$$
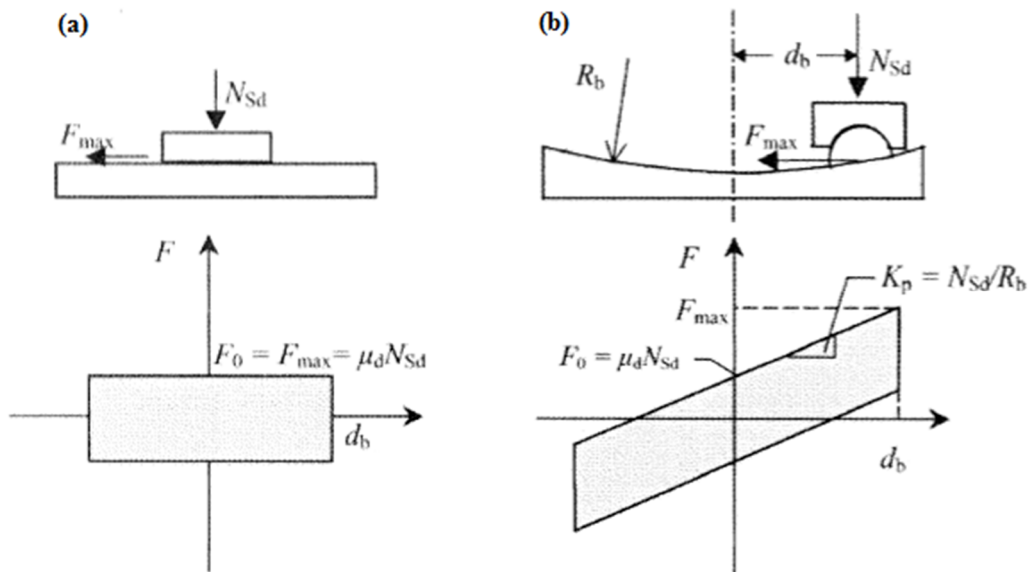
Figure 3.4 – Friction force-displacement behaviour
(Eurocode 8 - Design of Structures for Earthquake Resistance, 2005)

The previous Equation 3.2 represents a nonlinear hysteretic law and, in particular, FPS behaviour may be modelled through a bilinear one (Figure 3.5), characterized by three main parameters:

- the characteristic strength $F_0 = \mu_d N_{Sd}$;

- the secondary stiffness k_2, which is related to the restoring force and represents the system stiffness corresponding to the plastic branch, once the friction threshold has been exceeded:

$$k_2 = \frac{N_{Sd}}{R_b} \tag{3.3}$$

- the elastic stiffness k_1, considered proportional to the secondary one by a coefficient α: $k_1 = \alpha k_2$.
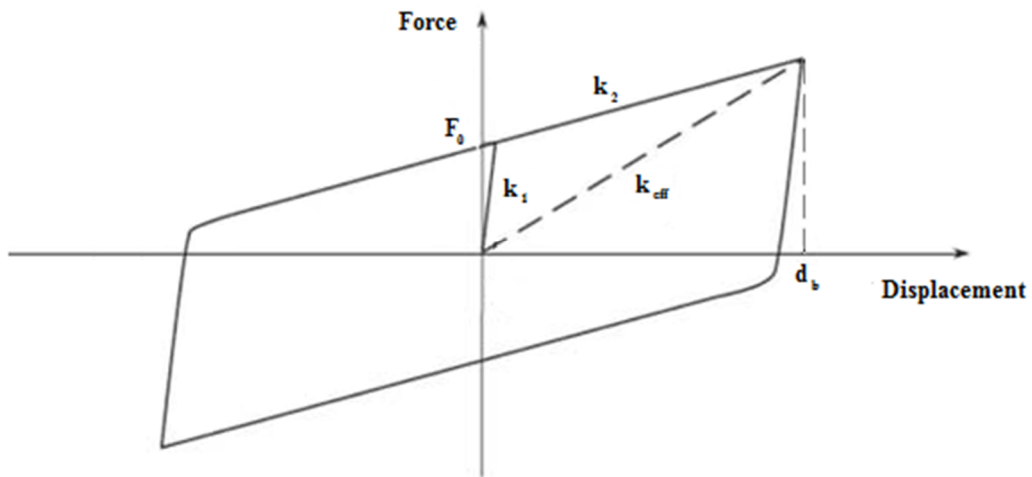
Figure 3.5 – Bilinear hysteretic behaviour: Equivalent model

Actually, sliding devices are characterized by a virtually infinite stiffness until the horizontal force does not exceed the static friction one: that's why the first segment of the hysteresis cycle is usually assumed as vertical. In this sense, Professor Kelly (Kelly J. , 1996) has suggested a value of $\alpha = 51$. Hence, in a first phase, called *sticking*, the super- and substructure are rigidly connected and the whole system may be considered to behave like a non-isolated structure. After exceeding the static friction threshold, the pendular motion starts and the system is governed by the secondary stiffness k_2. Once the maximum displacement is reached, the friction coefficient instantaneously becomes nil. In this phase, to let the pendulum motion restart in the opposite direction, the friction threshold has to be exceeded once again: this is represented by a vertical segment of length $2F_0$ (Figure 3.6).
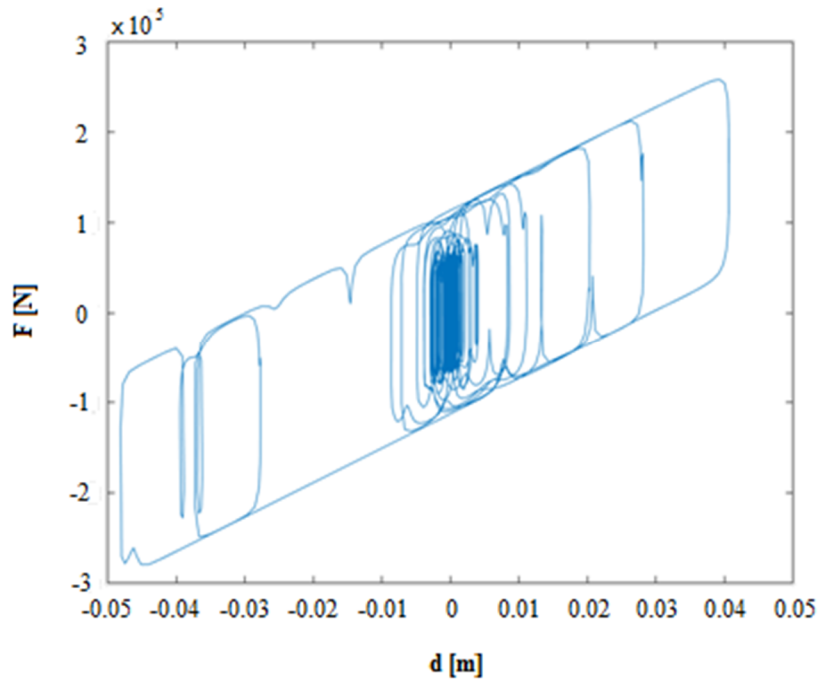
Figure 3.6 – Bilinear hysteretic behaviour: Typical cycle of FPS

The FPS nonlinear dynamic behaviour may be well explained analysing the scheme depicted in Figure 3.7 (Zayas, Low, & Mahin, 1987), which shows the forces acting on the slider:

- the lateral force F;
- the vertical load W through the isolating device;
- the friction force F_a along the sliding surface;
- the contact force S, orthogonal to the sliding interface;
- the traction forces f_a on the slider surface, whose effect is implicitly incorporated in the friction force.
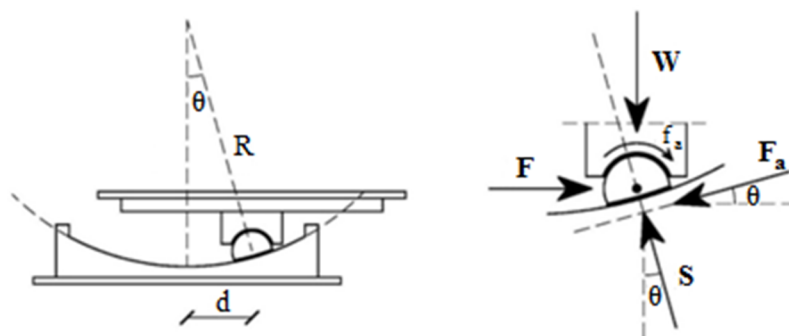
Figure 3.7 – FPS dynamic configuration

Therefore, they may be expressed the equations governing the dynamic behaviour, considering the equilibrium in horizontal and vertical directions, respectively:

$$\begin{cases} F - F_a \cos\theta - S\sin\theta = 0 \\ W + F_a \sin\theta - S\cos\theta = 0 \end{cases} \qquad (3.4)$$

$$\begin{cases} F = F_a \cos\theta + S\sin\theta \\ S = \dfrac{W}{\cos\theta} + \dfrac{F_a \sin\theta}{\cos\theta} \end{cases} \qquad (3.5)$$

Combining the latter two equations:

$$F = F_a \cos\theta + W\tan\theta + F_a \frac{\sin\theta^2}{\cos\theta} = W\tan\theta + F_a \frac{(\sin\theta^2 + \cos\theta^2)}{\cos\theta} \qquad (3.6)$$

$$F = W\tan\theta + \frac{F_a}{\cos\theta} \qquad (3.7)$$

Expressing the horizontal displacement in relation with the effective radius, the lateral force may be rewritten as:

$$d = R\sin\theta \qquad (3.8)$$

$$F = \frac{Wd}{R\cos\theta} + \frac{F_a}{\cos\theta} \qquad (3.9)$$

Finally, under the hypothesis of small oscillations:

$$\sin\theta \sim \tan\theta \sim \theta \cong \frac{1}{R} \qquad (3.10)$$

$$\cos\theta \sim 1 \qquad (3.11)$$

Hence, the force – displacement relationship results:

$$F = \frac{W}{R}d + F_a \qquad (3.12)$$

and Equation 3.2 is demonstrated, as the friction force F_a is depending on the friction coefficient and on the normal component of the vertical force:

$$F_a = \mu_d W\cos\theta \cong \mu_d W \qquad (3.13)$$

Besides, the restoring capability of the friction pendulum isolating system is assured if the related force exceeds the friction one; this happens for specific values of the maximum displacement d, in function of the friction coefficient:

$$\frac{W}{R}d > \mu_d W \qquad \Rightarrow \qquad d > \mu_d R \qquad (3.14)$$

Hence, if the displacement values are lower than $\mu_d R$, the system will be in a configuration of stable equilibrium and it will not able to restore; conversely, for higher displacements, the restoring capability is guaranteed. This is the reason why they should be preferred materials with low friction coefficient, such as PTFE.

In conclusion, it is noteworthy that the fundamental vibration period of the isolated structure is independent of its weight and is function of the curvature radius only, thus resulting equivalent to the period of a pendulum:

$$T_d = 2\pi\sqrt{\frac{m_d}{k_d}} = 2\pi\sqrt{\frac{m_d}{m_d g/R}} = 2\pi\sqrt{\frac{R}{g}} \qquad (3.15)$$

3.2.1.1 *Linear modelling of FPS dynamic behaviour*

Assuming as reference the secant stiffness value k_{eff} (Figure 3.5), defined as the ratio between the maximum horizontal force and the maximum lateral displacement exhibited by the isolator:

$$k_{eff} = \left(\frac{Wd}{R} + \mu_d W\right)\frac{1}{d} = \left(\frac{1}{R} + \frac{\mu_d}{d}\right)W \qquad (3.16)$$

the related natural vibration period is then:

$$T_{eff} = 2\pi\sqrt{\frac{m_d}{k_{eff}}} = 2\pi\sqrt{\frac{1}{g\left(\frac{1}{R} + \frac{\mu_d}{d}\right)}} \qquad (3.17)$$

A base isolation system may be modelled considering an equivalent linear viscoelastic behaviour if all the following conditions are satisfied (Norme Tecniche per le Costruzioni, 2008):

- the equivalent stiffness of the isolating system is at least 50% of the secant stiffness for hysteresis cycles implying deformation values equal to 20% of the reference displacement; for FP devices, this requisite is achieved by imposing:

$$\frac{R}{d_{dc}} \leq \frac{1}{3\mu_d}$$

    where d_{dc} is the centre of rigidity displacement due to seismic action, with reference to the considered limit state;

- the equivalent linear damping of the isolation system is less than 30%;

- the force – displacement characteristics of the isolating system do not vary by more than 10% due to variations in deformation velocity, within a range of $\pm$ 30% around the design value, and in vertical load on the devices;

- the force increase in the isolating system for displacement values between $0.5d_{dc}$ and d_{dc} is at least equal to 2.5% of the superstructure total weight.

If the system may be represented by a linear equivalent model, the value of the period T_{eff} differs from the corresponding tangent one for no more than 14%, so that also the difference, in terms of dynamic response parameters, between linear and nonlinear models results to be insignificant. If the previous requirements for the use of a linear equivalent model are not respected, instead, the dynamic response has to be evaluated by means of nonlinear analyses able to detect the phenomena related to the transition from states characterized by different rigidities.

Another important parameter that defines the sliding isolator behaviour is the equivalent viscous damping coefficient, which may be estimated through the equivalence between the energy dissipation produced by friction and that caused by the viscous behaviour:

$$\xi_{eff} = \frac{Hysteresis\ cycle\ area}{2\pi k_{eff}d^2} = \frac{4\mu_d W d}{2\pi \left(\frac{1}{R} + \frac{\mu_d}{d}\right) W d^2} \tag{3.18}$$

$$\xi_{eff} = \frac{2\mu_d}{\pi \left(\frac{d}{R} + \mu_d\right)} \tag{3.19}$$

The equivalent damping is thus function of the friction coefficient, curvature radius and displacement demand. The latter identifies the displacement design value for the considered limit state: consequently, the equivalent dissipation to be adopted in an elastic analysis

depends on the specific limit state and assumes different values in relation to the system displacement demand. Generally, this value is related to the Life Safety limit state for the super- and substructure verification; the required increased reliability of the isolating system, instead, shall be implemented by designing each device with reference to the Near Collapse limit state.

When the equivalent stiffness or damping coefficient significantly depends on the design displacement, it should be carried out an iterative process until the difference between the calculated and the assumed value is less than 5%.

It is noteworthy that the adoption of an equivalent linear model is possible only if the vertical seismic component is lower than 0.1g. In any case, even in the absence of a vertical acceleration component, the variation of axial load through the devices has to be less than 10% of the value related to the quasi-permanent combination. Otherwise, it is necessary to resort to a nonlinear analysis by assuming a suitable constitutive law and proceeding with a step by step integration of the equations of motion.

3.2.2 *Mechanics of Friction Pendulum devices*

Friction is the force resisting the relative motion of solid surfaces, fluid layers and material elements sliding against each other. There are several types of friction, i.e., dry, fluid, lubricated, skin, internal friction: in this context the first one will be considered.

Dry friction is a force that opposes the relative lateral motion of two solid surfaces in contact. It depends on contact type and geometry, contact surfaces velocity and on the involved materials properties. With the exception of atomic or molecular friction, dry friction arises from the interaction of surface features, known as asperities: each asperity carries a load, the summation of which equilibrates the normal force N, i.e., the net force compressing two parallel surfaces together. The deformation of each asperity is firstly elastic and then plastic, once the tangential load F has exceeded the material shear strength (Figure 3.8).
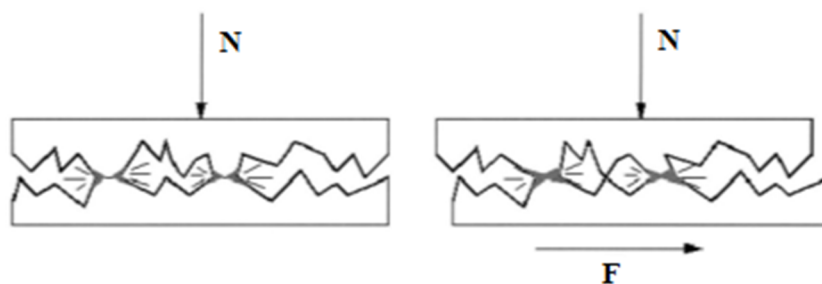
Figure 3.8 – Simplified friction mechanism

Coulomb friction is an approximate model used to calculate the force of dry friction. It is governed by the law:

$$F \leq \mu N \tag{3.20}$$

in which:

- F is the friction force exerted by each surface on the other. It is parallel to the surface, in a direction opposite to the net applied force;
- μ is the coefficient of friction, which is an empirical property of the contacting materials. It is characterized by a constant value;
- N is the normal force exerted by each surface on the other, directed perpendicular to the surface.

Dry friction may present two regimes: *static friction* and *kinetic friction* (sliding or dynamic friction), between non-moving and moving surfaces, respectively. They are characterized by different friction coefficients, denoted as μ_{static} and $\mu_{dynamic}$. Usually, the static coefficient is higher than the dynamic one.

3.2.2.1 *Experimental studies on FPS friction coefficient*

Although the Coulomb law is the most applied friction model, it is not suitable to analyse the sliding devices behaviour, as their friction coefficient is not constant. Experimental surveys (Mokha, Constantinou, & Reinhorn, 1990), (Constantinou, Mokha, & Reinhorn, 1990) & (Constantinou M. C., Whittaker, Kalpakidis, Fenz, & Warn, 2007), carried out on FP devices with stainless steel-PTFE interface, showed a close dependence of the friction dynamic coefficient on sliding velocity and contact pressure. Moreover, it is influenced by temperature, loading time, cyclic load and axial load variation.

Effect of sliding velocity and pressure

In normal temperature conditions ($\approx 20°C$) and in presence of clean and non-lubricated interfaces, the dynamic friction coefficient, starting from the static (or breakaway) value μ_B at zero velocity, initially decreases as the sliding velocity increases, until a minimum value f_{min} is reached. Then, further increments in sliding velocity cause a progressive increase of the friction coefficient up to a maximum constant value f_{max}. Besides, for a specific velocity value, the dynamic coefficient reduces as the applied normal load is incremented (Figure 3.9).
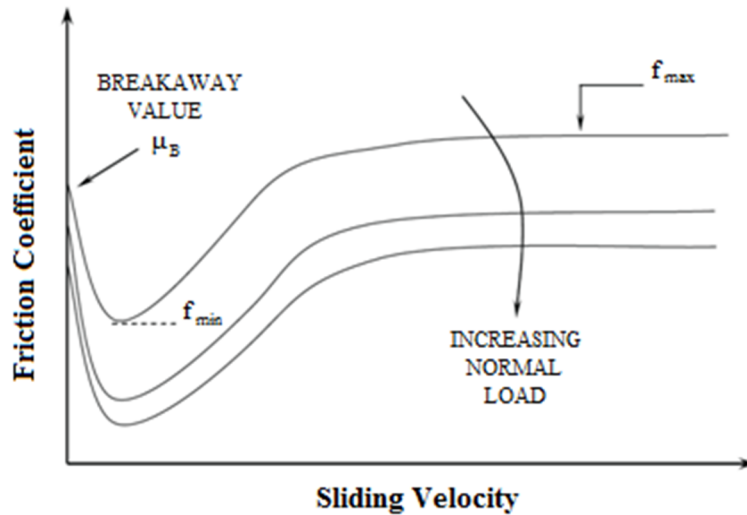
Figure 3.9 – Effect of sliding velocity and pressure on dynamic friction coefficient

It is pointed out that the illustrated behaviour is obtained in testing the sliding device under cyclic harmonic displacements and that measurements of the sliding friction are related to the first cycle, at the first instant in which the peak sliding velocity is attained. The sliding friction is also known to decrease with increasing number of cycles, because of interface heating. Friction in this interface is primarily the result of *adhesion*.

Adhesion is a phenomenon related to the atomic bonds between the contacting sliding surfaces. As they usually show many superficial irregularities, it is necessary to make a distinction between the *apparent area* and the *real area*, over which the two sliding bodies are in contact. The real area of contact is the sum of several small contact regions, called junctions of contact, where atomic bonds take place (Figure 3.10).
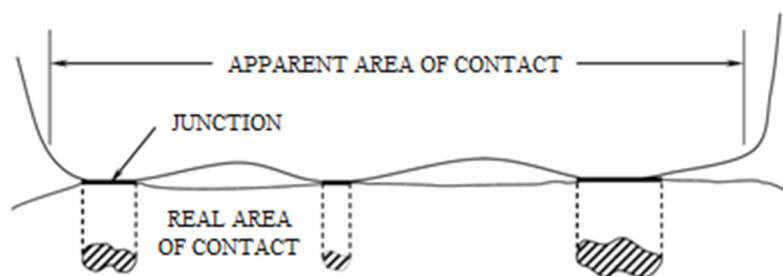
Figure 3.10 – Real contact area and apparent area
(Constantinou M. C., Whittaker, Kalpakidis, Fenz, & Warn, 2007)

To separate the two surfaces, it is necessary a force equal to the product of the junctions shear resistance s and the real contact area (Bowden F.P., Tabor D., 1964):

$$F_a = sA_r \qquad (3.21)$$

According to the previous equation, friction is the required force to break bonds between the contacting surfaces.

There is a threshold pressure value p_0 identifying the incipient plastic deformations; in this case the real contact area increases while the pressure remains constant. In fact, if an extended surface, with lots of contact junctions, is considered, an increase in normal load, from W_a to W_b, generates the increment in the junctions' number and so in the contact area (Figure 3.11).
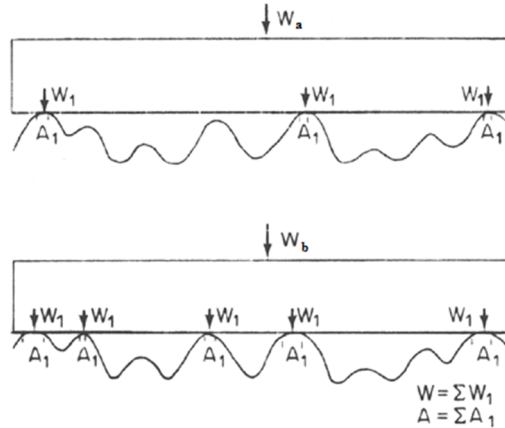
Figure 3.11 – Deformation of asperities under loading (Halling, 1981)

Since the normal load through the device generates a pressure:

$$p = \frac{N}{A_r} \qquad\qquad (3.22)$$

the real contact area may be expressed as:

$$A_r = \frac{N}{p_0} \qquad\qquad (3.23)$$

The friction force is then proportional to the normal load:

$$F_a = \frac{sN}{p_0} \qquad\qquad (3.24)$$

If PTFE exhibits only elastic deformations, the contact area will be exponentially proportional to the load (Mohka, Constantinou, & Reinhorn, 1988):

$$A_r = kN^n \qquad\qquad (3.25)$$

where k is a constant value related to the surface conformation and n is a constant that varies in the range $\frac{2}{3} \div 1$.

In order to evaluate the relation between friction coefficient and load, the Bowden and Tabor *Adhesion Model* is used.

The shear strength of the interface may be approximated as a linear function of the actual pressure (pressure over the real contact area):

$$s = s_o + \alpha p \tag{3.26}$$

The friction coefficient thus may be expressed as:

$$\mu = \frac{F_a}{N} = \frac{(s_o + \alpha p)A_r}{pA_r} = \frac{s_o}{p} + \alpha \tag{3.27}$$

The following Figure 3.12 illustrates the variation of real contact area, contact pressure and friction coefficient with normal load.
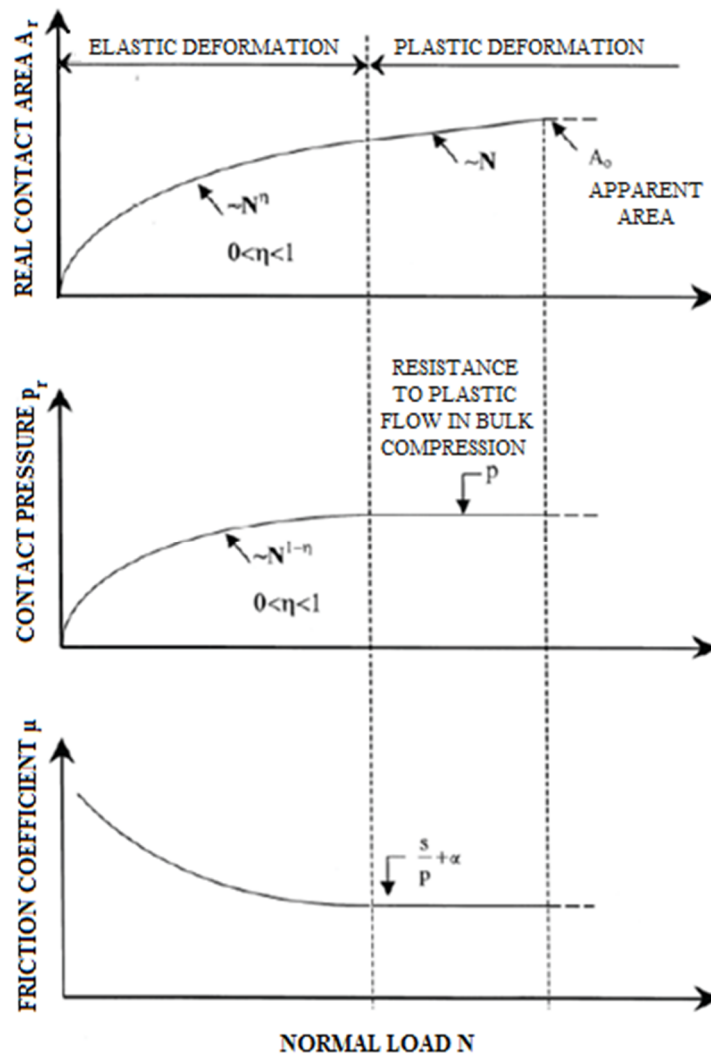
Figure 3.12 – Variation of real contact area, contact pressure, friction coefficient in function of the normal load (Constantinou M. C., Whittaker, Kalpakidis, Fenz, & Warn, 2007)

Assuming elastic deformations of asperities, the real contact area is proportional to the normal load, according to Equation 3.25. As the load increases, deformations might be mainly plastic and the real contact area will be represented by Equation 3.23: if plastic deformations occur, the actual pressure remains constant and the real contact area increases in proportion to the normal load. Hence, by considering elastic and plastic deformations of PTFE asperities, it is possible to explain the reduction in the friction coefficient with increasing normal load and the eventual attainment of a nearly constant value.

The initial friction coefficient value μ_B is very high because of adhesion forces. When the motion starts, a thin crystalline film of PTFE lays down on the steel surface: this reduces the friction coefficient down to the f_{min} value, due to the low shear resistance of the film. The following increment with the increase in sliding velocity leads to the f_{max} value, which is 5-6 times higher than f_{min}, for velocity values concerning seismic applications (160-400 mm/s).

M. Dolce, D. Cardone and F. Croatto studied sliding isolators with PTFE-stainless steel non-lubricated interface, for three different temperature values: -10°C, 20°C, 50°C (Figure 3.13).
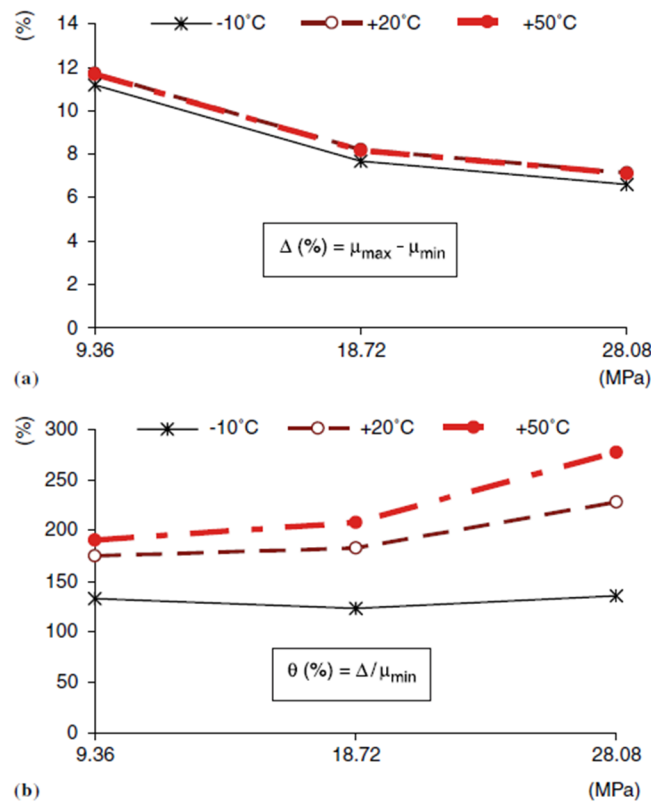
Figure 3.13 – (a) absolute and (b) percentage increment of the sliding friction coefficient with reference to service conditions, as a function of contact pressure and for three different air temperatures

The difference between the maximum and minimum values of the sliding friction coefficient, $\Delta = f_{max} - f_{min}$, is higher at low contact pressure, assuming nearby 12% values for 9.36 MPa and less than 7% for 28.08 MPa. Temperature, instead, has a negligible influence on Δ, Figure 3.13 – a.

Conversely, the effect of temperature is more evident on the dimensionless parameter $\theta = \frac{\Delta}{f_{min}}$, whose trend is increasing with the contact pressure, especially at medium-to-high temperatures, Figure 3.13 – b.

According to the experimental results, the dynamic friction coefficient is practically constant for seismic applications, i.e. at very high sliding velocities, but significantly different from the friction coefficient in slow movements (Dolce, Cardone, & Croatto, 2005).

Effect of temperature

Viscoelastic materials, such as Teflon®, are very sensitive to temperature: the friction coefficient reduces as the temperature increases; in particular, a change in temperature has drastic effects on the breakaway and minimum dynamic values of the friction coefficient (Figure 3.14).
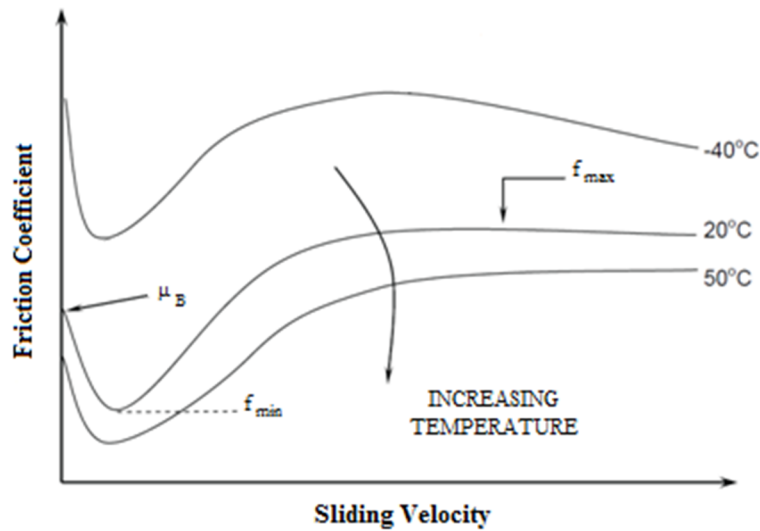
Figure 3.14 – Effect of temperature on variation of friction coefficient

The friction coefficient reduction rate is higher if the temperature variation is from low to medium values, rather than from medium to high ones. Actually, the heat produced through sliding is proportional to the friction coefficient: the heat flux at high velocities (500 mm/s) is much greater than that at low velocities (< 1 mm/s). Then, the heating up of the surfaces occurring at high velocities compensates for the effects on viscoelastic properties of

PTFE due to low temperature values. Therefore, a variation from 20°C to -40°C leads to an increment in f_{max} about only 50%.

The following Figure 3.15 shows the reduction ratio of the friction coefficient, for low and high velocities, $v_1 = 8$ mm/s and $v_2 = 316$ mm/s, in function of temperature and for three different contact pressure values, 9.36 MPa, 18.7 MPa and 28.1 MPa. For high sliding velocities, usually regarding seismic applications, the reduction ratio is about $0.15 - 0.3\%/°C$, for lubricated surfaces. Hence, it depends on the sliding velocity but not on the contact pressure.

$$(P_1 = 9.36 MPa, v_1 = 8mm/s): \mu = 1.09E\text{-}1 - 7.31E\text{-}4*\Delta T + 4.3E\text{-}6*\Delta T^2$$
$$(P_2 = 18.7 MPa, v_1 = 8 mm/s): \mu = 8.45E\text{-}2 - 7.31E\text{-}4*\Delta T + 4.3E\text{-}6*\Delta T^2$$
$$(P_3 = 28.1 MPa, v_1 = 8 mm/s): \mu = 6.85E\text{-}2 - 7.31E\text{-}4*\Delta T + 4.3E\text{-}6*\Delta T^2$$

in which $\Delta T = (T-T_0)$ and $T_0 = -10°C$

$$(P_1 = 9.36 MPa, v_2 = 316mm/s): \mu = 1.96E\text{-}1 - 3.95E\text{-}4*\Delta T + 1E\text{-}6*\Delta T^2$$
$$(P_2 = 18.7 MPa, v_2 = 316mm/s): \mu = 1.42E\text{-}1 - 3.95E\text{-}4*\Delta T + 1E\text{-}6*\Delta T^2$$
$$(P_3 = 28.1 MPa, v_2 = 316mm/s): \mu = 1.18E\text{-}1 - 3.95E\text{-}4*\Delta T + 1E\text{-}6*\Delta T^2$$

in which $\Delta T = (T-T_0)$ and $T_0 = -10°C$
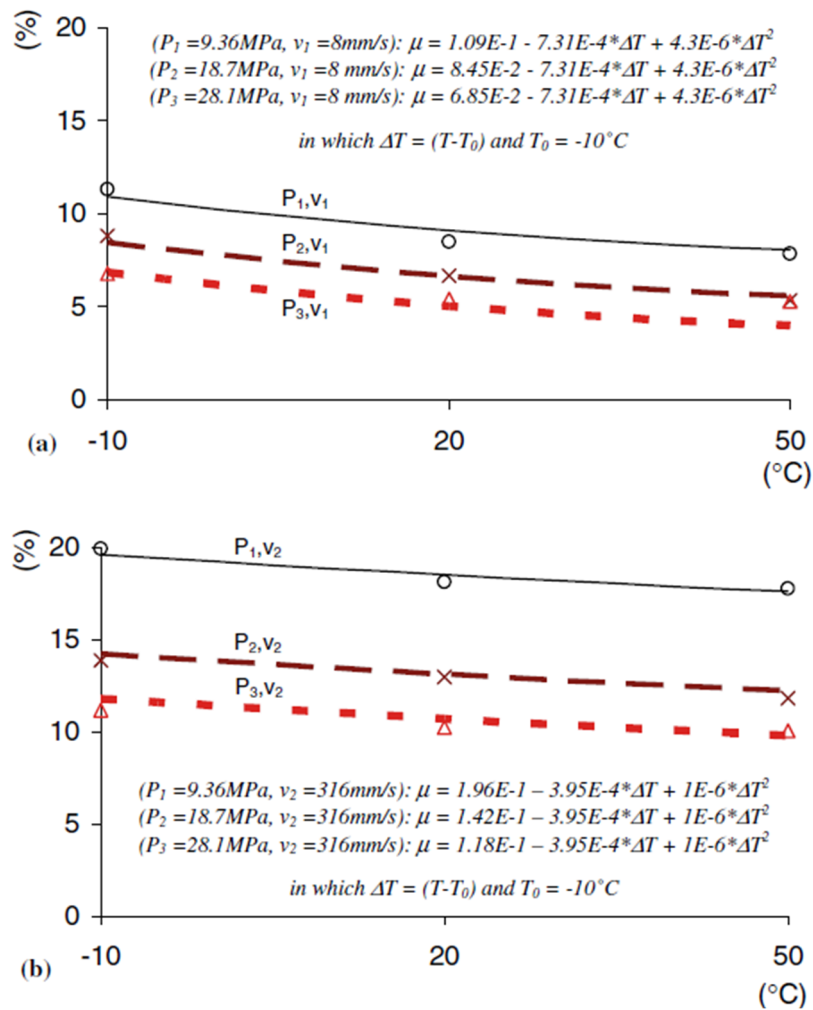
Figure 3.15 – Reduction ratio of the friction coefficient, for a) low and b) high velocities, in function of temperature and for three different contact pressure values

Effect of loading time and cyclic loads

Teflon® is a material characterized by a viscoelastic behaviour, so it would be expected that the effect of the load on the real contact area and then on the friction coefficient is higher as the loading time increases (Bowden F.P., Tabor D., 1964). However, experimental

studies carried out on polymeric materials proved that loading time has not influence on the static coefficient (Mokha, Constantinou, & Reinhorn, 1990), whose values resulted to be essentially the same for a load applied for 0.5 hours and 594 days. On the other hand, tests carried out on specimens subjected to previous cyclic loads showed a reduction in static friction coefficient, due to the formation of a PTFE film on the steel surface after the first cycle (Constantinou M. C., Whittaker, Kalpakidis, Fenz, & Warn, 2007). The friction coefficient tends to decrease during loading cycles at high velocities, due to the viscoelastic properties of Teflon®. This reduction is about 25-30%.

Effect of axial load variation on seismic behaviour of devices

Seismic isolators are characterized by a very high vertical stiffness only in compression: if they are subjected to traction forces, they may suffer damage to the sliding interface or become unseated. Moreover, the permanence in compressive states is necessary to apply linear analysis methods.

Since the equivalent period T_{eff} and the horizontal force F developed by the isolating system are direct functions of the axial load through the devices, they experience the after-effects of axial load variations, caused by the force system opposing to the overturning moment due to horizontal actions and simultaneous seismic vertical action. These variations involve irregularities in the force-displacement relation of the isolators.

3.2.3 *Modelling of Dynamic Friction Coefficient*

Experimental results (Mokha, Constantinou, & Reinhorn, 1990), (Constantinou, Mokha, & Reinhorn, 1990) & (Constantinou M. C., Whittaker, Kalpakidis, Fenz, & Warn, 2007) suggest that the sliding coefficient of friction pendulum devices with stainless steel-PTFE interface obeys to the following the law:

$$\mu = f_{max} - (f_{max} - f_{min})e^{-\alpha v} \qquad (3.28)$$

where:

- f_{max} is the friction coefficient maximum value, attained at large velocities of sliding;
- f_{min} is the minimum friction coefficient at essentially zero velocity;
- v is the bearing sliding velocity;

- α is a constant coefficient represented by the inverse of the characteristic sliding velocity; it assumes the values in the range 20-30 s/m for PTFE-steel interfaces (Mokha, Constantinou, & Reinhorn, 1990), (Constantinou, Mokha, & Reinhorn, 1990) & (Constantinou M. C., Whittaker, Kalpakidis, Fenz, & Warn, 2007).

In the following Figure 3.16 is shown the relation between the friction coefficient and the sliding velocity according to Equation 3.28, i.e., the Constantinou law. In particular, it may be observed the influence of the α parameter on the dimensionless friction coefficient $\dfrac{\mu}{f_{max}}$.
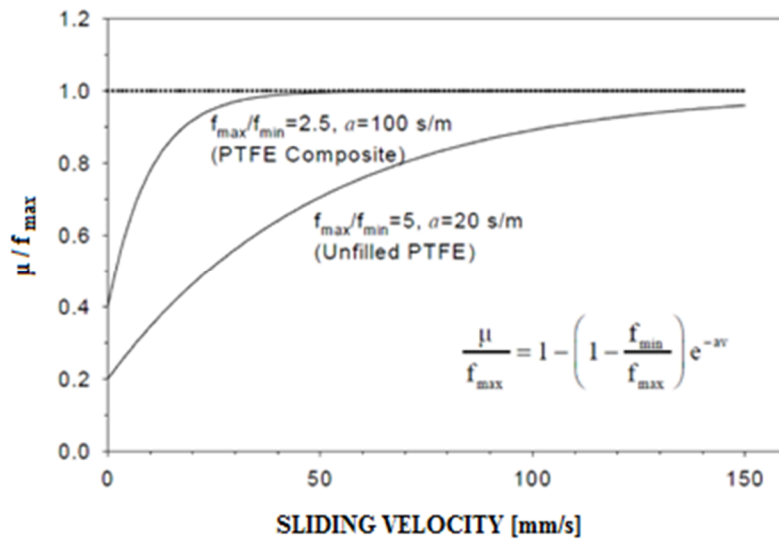
Figure 3.16 – Effect of the α parameter on friction coefficient according to Constantinou law

It is noteworthy that, for all PTFE devices, the maximum friction coefficient value is achieved at sliding velocity values about 150 mm/s: seismic events are characterized by higher values, 200-800 mm/s, thus reaching f_{max} is always assured. Moreover, although Constantinou law does not consider the friction coefficient initial decay, as that shown in Figure 3.9, during earthquakes it is reached the range of friction coefficient values in which the two models are similar. Hence, the friction coefficient modeling according to Constantinou law is reliable for seismic applications.

MODELLING AND PARAMETRIC ANALYSIS OF ISOLATED BRIDGE SYSTEM

The stochastic response of a multispan continuous deck bridge seismically isolated by the friction pendulum system (Figure 4.1) has been investigated.

The earthquake analysis of the isolated bridge under consideration has been performed basing on the following assumptions:

- The bridge was symmetric, so that it was possible to analyse the pier – abutment interaction: it was necessary to identify an appropriate model to study the relative displacements generated by the presence of the FPS below the deck;

- The bridge deck was straight and it was idealized as a rigid body;

- Bridge piers and abutments were modelled as rigidly fixed at the foundation level and were considered to support half the weight of the superstructure;

- Bridge piers were assumed to remain in the elastic state during the earthquake excitation. This is a reasonable assumption as the isolation attempts to reduce the earthquake response in such a way that the structure remains within the elastic range;

- The piers were modelled as a lumped mass system divided into a number of small discrete segments: each segment was connected by a node with one horizontal degree-of-freedom (dof) under consideration. The masses of each segment were assumed to be distributed between the two adjacent nodes in the form of point masses;

- The FP bearings provided at the piers and abutments had the same dynamic characteristics;

- The force-deformation behaviour of the FPS was considered to be rigid bilinear.
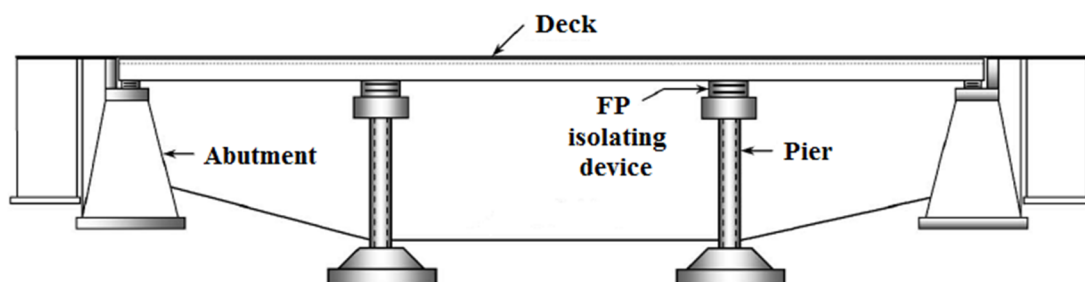
Figure 4.1 – Bridge elevation (Jangid R. , 2008)

4.1 MATHEMATICAL BRIDGE MODEL

At first, a preliminary study, in which both the pier and the abutment have been modelled with one degree-of-freedom, has been carried out. This simplified model has been validated using professional computing software.

Subsequently, the evolution of the pier model to n dof ($n+1$ dof system, Figure 4.2) has been carried out, looking out for avoiding problems of stability of the model and convergence of the analysis.
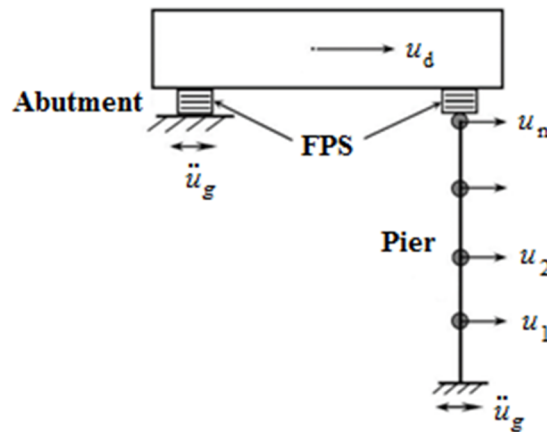
Figure 4.2 – Mathematical bridge model

This system is based on the Jangid theory (Jangid R. , 2008). The substructure of the bridge consists of rigid abutments and reinforced concrete piers; the FPS used is a spherically shaped, articulated sliding bearing (Zayas, Low, & Mahin, 1990).

4.1.1 Analysis Method

The analysis methods of seismically isolated bridges may consist of (Eurocode 8 - Design of Structures for Earthquake Resistance, 2005):

- the Fundamental mode Spectrum Analysis;
- the Multimode Spectrum Analysis;
- the Time history nonlinear Analysis.

The Fundamental mode and the Multimode analyses are based on representing the isolators behaviour by linear elastic elements with stiffness equal to the effective or secant stiffness of the element at the actual displacement. The effect of energy dissipation of the isolation system is accounted for representing the isolators with equivalent linear viscous elements on the basis of the energy dissipated per cycle at the actual displacement. The

response is then calculated by use of response spectra. Given that the actual displacement is unknown until the analysis is performed, these methods require some iterations until the assumed and calculated values of isolator displacement are equal (Constantinou M. , Whittaker, Fenz, & Apostolakis, 2007).

The Time history analysis Method is the most accurate. It should be used with explicit nonlinear representation of the characteristics of each isolator. When time history analysis is performed, a suite of not fewer than three appropriate ground motions shall be considered. If at least seven ground motions are analysed, the average value of the response parameter of interest shall be permitted to be used for design, while, if the ground motions are fewer than seven, the maximum value has to be considered. Ground motions shall consist of pairs of appropriate horizontal ground motion acceleration components that have to be selected and scaled from individual recorded events. Appropriate ground motions shall be selected from events having magnitudes, fault distance and source mechanisms that are consistent with those controlling the maximum considered earthquake. If the required number of recorded ground motion pairs is not available, appropriate simulated ground motion pairs shall be used to make up the total number required (Constantinou M. , Whittaker, Fenz, & Apostolakis, 2007). Time history analysis has to be performed in the case of isolated structures whose isolating system may not be represented by means of an equivalent linear model (Eurocode 8 - Design of Structures for Earthquake Resistance, 2005).

In this study, a nonlinear time history analysis has been carried out: it allowed the evaluation of the seismic response by the direct integration of the motion equations, after applying to the structure opportunely selected accelerograms.

4.2   *DYNAMICS OF ISOLATED BRIDGES*

First of all, it is pointed out that in this study it has been investigated the isolated bridge response in the only longitudinal direction; hence, the maximum seismic excitation acted along this direction. Transverse and vertical effects and any back-up systems have been disregarded.

According to Jangid (Jangid R. , 2008), the equations governing the motion of the isolated bridge are:

$$m_d \ddot{u}_d + F_a + F_p = -m_d \ddot{u}_g \qquad (4.1)$$

$$[m_p]\{\ddot{u}_p\} + [c_p]\{\dot{u}_p\} + [k_p]\{u_p\} - \{\psi\}F_p = -[m_p]\{1\}\ddot{u}_g \qquad (4.2)$$

in which:

- m_d is the mass of the deck;
- $[m_p]$, $[c_p]$ and $[k_p]$ are the mass, damping and stiffness matrices of size $n \times n$, respectively, of the pier under top free condition and according to the number n of nodes in which it is divided;
- F_a and F_p are the restoring forces of the FPS at abutment and pier level, respectively;
- u_d is the displacement of the deck relative to the ground;
- $\{u_p\} = \{u_1, u_2, \dots, u_n\}^T$ is the vector of the displacement of various nodes of the pier;
- $\{\psi\} = \{1, 0, \dots, 0\}^T$ is a vector of size $n \times 1$ that applies the restoring force of the specific FPS in its correspondence;
- $\{1\}$ is a unit vector of size $n \times 1$ that identifies the influence coefficient vector of the earthquake ground acceleration $\ddot{u}_g$.

The restoring forces of the FPS at abutment and pier level are $(i = a, p)$:

$$F_i = \frac{m_d g}{2R} u_d + \mu_d \frac{m_d}{2} g \cdot \text{sgn}(\dot{u}_d) \qquad (4.3)$$

The term $m_d g$ identifies the weight W of the deck, so that $\frac{W}{R}$ denotes the deck stiffness k_d: the product $k_d u_d$ represents the elastic contribution of the FPS response. The frictional contribution is represented by the second term on the right and is dependent on the friction coefficient of the FPS, which may be defined by the following equation (§ 3.2.3):

$$\mu_d = f_{max} - (f_{max} - f_{min})e^{-\alpha|\dot{u}_d|} \qquad (4.4)$$

where f_{max} is the friction coefficient maximum value, attained at large velocities of sliding, f_{min} is the minimum friction coefficient at essentially zero velocity, α is a parameter controlling the variations of velocity coefficients due to contact pressure, temperature and surface conditions, $|\dot{u}_d|$ is the sliding velocity module. It is noteworthy that both the elastic and frictional terms have been halved as the deck is considered to be equally supported by pier and abutment.

The previous equations contemplate the absolute displacements, velocities and accelerations, so that the matrix of the masses is diagonal, while those of damping and stiffness are symmetric. Conversely, according to the Kelly theory (Kelly J. M., 1990), which considers the relative displacements, the matrix of the masses is symmetric and those of damping and stiffness are diagonal. Basing on this latter convention, the absolute displacements may be written in terms of the relative ones:

$$u_d = v_d + v_{p,1} + v_{p,2} + \cdots + v_{p,n} \tag{4.5}$$

$$u_{p,n} = v_{p,1} + v_{p,2} + \cdots + v_{p,n} \tag{4.6}$$

$$u_{p,1} = v_{p,1} \tag{4.7}$$

Therefore, the equations of motion and the FPS restoring force expressions become:

$$m_d\big(\ddot{u}_d + \ddot{v}_d + \ddot{v}_{p,1} + \cdots + \ddot{v}_{p,n}\big) + F_a + F_p = -m_d\ddot{u}_g \tag{4.8}$$

$$m_{p,n}\big(\ddot{v}_{p,1} + \cdots + \ddot{v}_{p,n}\big) - F_a - F_p + c_{p,n}\dot{v}_{p,n} + k_{p,n}v_{p,n} = -m_{p,n}\ddot{u}_g \tag{4.9}$$

$$m_{p,n-1}\big(\ddot{v}_{p,1} + \cdots + \ddot{v}_{p,n-1}\big) + c_{p,n-1}\dot{v}_{p,n-1} + k_{p,n-1}v_{p,n-1} - \\ -c_{p,n}\dot{v}_{p,n} - k_{p,n}v_{p,n} = -m_{p,n-1}\ddot{u}_g \tag{4.10}$$

$$m_{p,1}\big(\ddot{v}_{p,1}\big) + c_{p,1}\dot{v}_{p,1} + k_{p,1}v_{p,1} - c_{p,2}\dot{v}_{p,21} - k_{p,2}v_{p,2} = -m_{p,1}\ddot{u}_g \tag{4.11}$$

$$F_p = \frac{W}{2R}v_d + \mu_d\frac{W}{2}\cdot \text{sgn}(\dot{v}_d) \tag{4.12}$$

$$F_a = \frac{W}{2R}\big(v_d + v_{p,n} + \cdots + v_{p,1}\big) + \mu_d\frac{W}{2}\cdot \text{sgn}\big(\dot{v}_d + \dot{v}_{p,n} + \cdots + \dot{v}_{p,1}\big) \tag{4.13}$$

By combining these equations into a single system, it may be obtained:

$$
\begin{bmatrix} m_d & m_d & \cdots & m_d \\ m_d & m_d + m_{p,1} & \cdots & m_d + m_{p,1} \\ \vdots & \vdots & \ddots & \vdots \\ m_d & m_d + m_{p,1} & \cdots & m_d + \sum_{i=1}^{n} m_{p,i} \end{bmatrix} \begin{Bmatrix} \ddot{v}_d \\ \ddot{v}_{p,1} \\ \vdots \\ \ddot{v}_{p,n} \end{Bmatrix} + \begin{bmatrix} c_d & 0 & \cdots & 0 \\ 0 & c_{p,1} & \cdots & 0 \\ \vdots & \vdots & \ddots & \vdots \\ 0 & 0 & \cdots & c_{p,n} \end{bmatrix} \begin{Bmatrix} \dot{v}_d \\ \dot{v}_{p,1} \\ \vdots \\ \dot{v}_{p,n} \end{Bmatrix} +
$$

$$
+ \left(\begin{bmatrix} k_d & 0 & \cdots & 0 \\ 0 & k_{p,1} & \cdots & 0 \\ \vdots & \vdots & \ddots & \vdots \\ 0 & 0 & \cdots & k_{p,n} \end{bmatrix} + \frac{W}{2R} \begin{bmatrix} 0 & 1 & \cdots & 1 \\ 1 & 1 & \cdots & 1 \\ \vdots & \vdots & \ddots & \vdots \\ 1 & 1 & \cdots & 1 \end{bmatrix} \right) \begin{Bmatrix} v_d \\ v_{p,1} \\ \vdots \\ v_{p,n} \end{Bmatrix} +
$$

$$
+ \begin{Bmatrix} \frac{W}{2R} \\ 0 \\ \vdots \\ 0 \end{Bmatrix} u_d + \frac{W}{2} \begin{Bmatrix} 1 \\ 0 \\ \vdots \\ 0 \end{Bmatrix} \mu_{d,p} \cdot \mathrm{sgn}(\dot{v}_d) +
$$

$$
+ \begin{Bmatrix} \frac{W}{2R} \\ 0 \\ \vdots \\ 0 \end{Bmatrix} v_d + \frac{W}{2} \begin{Bmatrix} 1 \\ 0 \\ \vdots \\ 0 \end{Bmatrix} \mu_{d,a} \cdot \mathrm{sgn}\left(\left[\begin{Bmatrix} 1 \\ 0 \\ \vdots \\ 0 \end{Bmatrix} \dot{v}_d + \begin{Bmatrix} 0 \\ 1 \\ \vdots \\ 0 \end{Bmatrix} \dot{v}_{p,n+\cdots} + \begin{Bmatrix} 0 \\ 0 \\ \vdots \\ 1 \end{Bmatrix} \dot{v}_{p,1} \right] \right) =
$$

$$
= - \begin{bmatrix} m_d & m_d & \cdots & m_d \\ m_d & m_d + m_{p,1} & \cdots & m_d + m_{p,1} \\ \vdots & \vdots & \ddots & \vdots \\ m_d & m_d + m_{p,1} & \cdots & m_d + \sum_{i=1}^{n} m_{p,i} \end{bmatrix} \begin{Bmatrix} 0 \\ 0 \\ \vdots \\ 1 \end{Bmatrix} \ddot{u}_g \qquad (4.14)
$$

Where $\mu_{d,p}$ is function of $\dot{v}_d$ and $\mu_{d,a}$ is function of $\left(\left[\begin{Bmatrix} 1 \\ 0 \\ \vdots \\ 0 \end{Bmatrix} \dot{v}_d + \begin{Bmatrix} 0 \\ 1 \\ \vdots \\ 0 \end{Bmatrix} \dot{v}_{p,n+\cdots} + \begin{Bmatrix} 0 \\ 0 \\ \vdots \\ 1 \end{Bmatrix} \dot{v}_{p,1} \right] \right)$.

In order to simplify the discussion, the previous system may be expressed in compact form as it follows:

$$
[M]\{\ddot{v}\} + [C]\{\dot{v}\} + ([K] + [K]_1)\{v\} + F_a + F_p = -[M]\{I\}\ddot{u}_g \qquad (4.15)
$$

in which $\{I\} = \{0,0,\dots,1\}^T$ is a vector of size $n \times 1$.

4.2.1 *Dimensionless problem formulation*

In order to generalize the problem and unveil the characteristic parameters controlling the seismic behaviour of the system, the equations of motion are reduced to a dimensionless form, basing on the procedure followed in (Castaldo & Tubaldi, 2015).

After dividing the first equation by the mass m_d and the successive equations by the masses $m_{p,i}$, it is possible identifying the parameters:

- Mass ratio, $\lambda = \frac{m_p}{m_d}$;

- Damping factor of deck and pier, $\xi_d = \frac{c_d}{2\omega_d m_d}$ and $\xi_p = \frac{c_p}{2\omega_p m_p}$;

- Fundamental circular frequency of deck and pier, $\omega_d = \sqrt{\frac{k_d}{m_d}}$ and $\omega_p = \sqrt{\frac{k_p}{m_p}}$.

Then, by employing the time scale $\tau = \omega_d t$, the seismic input may be expressed in terms of the product between a scale factor IM, whose dimension is an acceleration, and a dimensionless function $\gamma(t)$, describing its variation over time:

$$\ddot{u}_g(t) = IM \cdot \gamma(t) = IM \cdot l(\tau) \qquad (4.16)$$

where $l(\tau)$ is obtained from $\gamma(t)$ by scaling the time t by the factor $1/\omega_d$.

In the same way, the displacements may be expressed in dimensionless form by introducing the length scale $\frac{IM}{\omega_d^2}$:

$$\psi_d(\tau) = \frac{v_d \omega_d^2}{IM} \qquad (4.17)$$

$$\psi_p(\tau) = \frac{v_p \omega_d^2}{IM} \qquad (4.18)$$

Hence, the dimensionless parameters (Π terms) that control the dimensionless response to the seismic input $\gamma(t)$ are:

$$\Pi_\omega = \frac{\omega_p}{\omega_d} \qquad (4.19)$$

$$\Pi_\lambda = \frac{m_p}{m_d} \qquad (4.20)$$

$$\Pi_{\xi_p} = \xi_p \qquad \Pi_{\xi_d} = \xi_d \qquad (4.21)$$

$$\Pi_\mu = \mu(\dot{\psi}_d)\frac{g}{a_0} \qquad (4.22)$$

Parameter Π_ω measures the degree of isolation, Π_λ is the previously defined mass ratio and Π_{ξ_p} and Π_{ξ_d} describe the viscous damping inherent respectively to the pier and the isolator. The dimensionless parameter Π_μ measures the isolator strength, provided by the friction coefficient $\mu(\dot{\psi}_d)$, relative to the seismic intensity. Since this parameter depends on the response through the velocity $\dot{\psi}_d$, the following parameter is used in its stead:

$$\Pi_\mu^* = f_{max} \frac{g}{IM} \qquad (4.23)$$

It is noteworthy that Π_μ^* is independent on the response and that the normalized response of the dynamic system does not depend on the seismic intensity level IM. The free-vibration response and the response to an impulsive input depends only on Π_ω, Π_λ, Π_{ξ_p}, Π_{ξ_d} and Π_μ^*. Conversely, the seismic response depends also on the function $\gamma(t)$. Moreover, having assumed $\tau = \omega_d t$ as time scale, it follows that the expression of $\gamma(t)$, corresponding to a seismic input $\ddot{u}_g(t)$ imposed to a system with circular frequency ω_d, changes with ω_d itself. Thus, the same seismic input $\ddot{u}_g(t)$ yields different dimensionless response histories $\psi(\tau)$ and solutions, for systems with different frequency ω_d.

Finally, it is pointed out that although Π_μ^* is defined basing on the isolator peak friction f_{max} only, the normalized system response depends also on the other isolator properties, that is, on f_{min} and on the exponent α appearing in Equation 4.4 and controlling the friction variation. However, to further simplify the problem, in the following analyses, it is assumed that $f_{max} = 3f_{min}$ based on a regression of the experimental results, whereas the exponent α is assumed equal to 30 s/m (Mokha, Constantinou, & Reinhorn, 1990), (Constantinou, Mokha, & Reinhorn, 1990) & (Constantinou M. C., Whittaker, Kalpakidis, Fenz, & Warn, 2007).

4.3 *MODELLING IN MATLAB®*

MATLAB® (Matrix Laboratory) is a multi-paradigm numerical computing environment. It allows matrix manipulations, plotting of functions and data, implementation of algorithms, creation of user interfaces. A supplementary package, Simulink, adds graphical multi-domain simulation and model-based design for dynamic and embedded systems.

In this sense, MATLAB® allowed to efficiently carry out the numerical modelling of the *n*+1 dof system, in the assumption of nonlinear behaviour of the isolating devices. Using the

Simulink® tool, it was possible to simulate the considered system by laying out, on a spreadsheet, a block system allowing to perform the desired task.

Figure 4.3 shows a simple example of a block diagram created in Simulink to solve a second order differential equation, that is the basis to implement the step by step integration of a *n* dof system of dynamic equations.
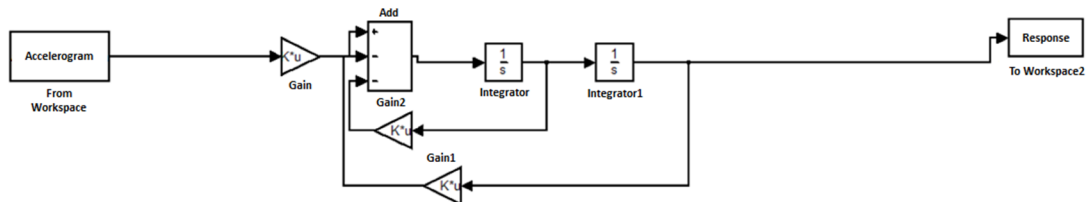
Figure 4. 3 – Second order differential equation solving within Simulink®

They may be individuated in the diagram the seismic input signal, which represents the history of the induced accelerations to the base of the analysed structure, the *integrator* blocks (in number equal to the order of the differential equation), which allow to trace the history of the system displacements, represented by the *response* block. It is also possible to introduce some *gain* blocks, through which the system's velocity and displacement histories, produced by the various *integrator* blocks, are multiplied by the entity set by the user in the respective dialog box: in the present case such entities are represented by the damping matrix and the stiffness matrix. This way, the software package performs the step by step integration of the input signal and, at each step, makes that integration pass through its respective *gains* and cyclically comes back to the *add* block, returning the looked-for results.

4.3.1 *Input parameters*

The analysis of the *n+1* dof model has been implemented considering a linear behaviour of the bridge and a nonlinear behaviour of the isolators, basing on literature research which led to the selection of the following input parameters:

- Four different values of the pier period T_p;
- Five different values of the isolating system period T_d;
- Three different values of the mass ratio λ;
- Ninety-five different values of the dimensionless friction coefficient Π_μ^*;
- Thirty seismic records, from natural earthquakes.

4.3.1.1 *Deterministic parameters*

They have been analysed 5700 different types of bridges, obtained by the combination of the deterministic parameters, which characterize the isolation level and the bridge and are displayed in the following Table 4.1.

T_p [s]	T_d [s]	λ [−]
0.05	2.0	0.10
0.10	2.5	0.15
0.15	3.0	0.20
0.20	3.5	
	4.0	

Table 4.1 – Deterministic input parameters values

The dimensionless friction coefficient Π_μ^* values have been defined as varying in the range $[0 \div 2]$, with constant step of 0.005 from 0 to 0.3 and with step 0.05 from 0.35 to 2. The first range is denser as it covers the Π_μ^* values giving the most relevant results.

4.3.1.2 *Seismic input*

The evaluation of the seismic performance of any engineered systems should account for the variability of the intensity, frequency content and duration of the records at the site. Coherent with the performance-based earthquake engineering approach (Aslani & Miranda, 2005), this study separates the uncertainties related to the seismic input intensity from those related to the characteristics of the record (record-to-record variability) by introducing a scale factor, that is, an intensity measure *IM*, through Equation 4.16. This way, the randomness in the seismic intensity may be described by a hazard curve, whereas the ground motion randomness for a fixed intensity level may be described by selecting a set of ground motion realizations characterized by a different duration and frequency content and by scaling these records to the common *IM* value.

The record-to-record variability has been defined through a set of thirty real ground motion records, considering the only horizontal component of the thirty accelerometer registrations, which are related to nineteen different seismic events (Table 4.2). These records have been selected within the websites of the Pacific Earthquake Engineering Research Centre (PEER, 2016), Italian Accelerometric Archive (ITACA, 2016) and European Strong-Motion Data (ISESD, 2016); they belong to the site classes B and C, as

defined in (Eurocode 8 - Design of Structures for Earthquake Resistance, 2005), their source-to-site distance, R, is greater than 8 km, and their moment magnitude, M, is in the range among 6.3 and 7.6. The record number is deemed sufficient to obtain quite accurate response estimates, given the efficiency of the IM employed (Luco & Cornell, 2007), although it may yield high response dispersions for high values of friction.

No.	Year	Earthquake name	Recording station name	$V_{S,30}$ [m/s]	Source [fault type]	M [−]	R [km]	PGA [g]
1	1994	Northridge	Beverly Hills – Mulhol	356	Thrust	6.7	13.3	0.52
2	1994	Northridge	Canyon Country – WLC	309	Thrust	6.7	26.5	0.48
3	1994	Northridge	LA – Hollywood Stor	316	Thrust	6.7	22.9	0.36
4	1999	Duzce, Turkey	Bolu	326	Strike-slip	7.1	41.3	0.82
5	1999	Hector Mine	Hector	685	Strike-slip	7.1	26.5	0.34
6	1979	Imperial Valley	Delta	275	Strike-slip	6.5	33.7	0.35
7	1979	Imperial Valley	El Centro Array #11	196	Strike-slip	6.5	29.4	0.38
8	1995	Kobe, Japan	Nishi-Akashi	609	Strike-slip	6.9	8.7	0.51
9	1995	Kobe, Japan	Shin-Osaka	256	Strike-slip	6.9	46.0	0.24
10	1999	Kocaeli, Turkey	Duzce	276	Strike-slip	7.5	98.2	0.36
11	1999	Kocaeli, Turkey	Arcelik	523	Strike-slip	7.5	53.7	0.22
12	1992	Landers	Yermo Fire Station	354	Strike-slip	7.3	86.0	0.24
13	1992	Landers	Coolwater	271	Strike-slip	7.3	82.1	0.42
14	1989	Loma Prieta	Capitola	289	Strike-slip	6.9	9.8	0.53
15	1989	Loma Prieta	Gilroy Array #3	350	Strike-slip	6.9	31.4	0.56
16	1990	Manjil, Iran	Abbar	724	Strike-slip	7.4	40.4	0.51
17	1987	Superstition Hills	El Centro Imp. Co.	192	Strike-slip	6.5	35.8	0.36
18	1987	Superstition Hills	Poe Road (temp)	208	Strike-slip	6.5	11.2	0.45
19	1987	Superstition Hills	Westmorland Fire St.	194	Strike-slip	6.5	15.1	0.21
20	1992	Cape Mendocino	Rio Dell Overpass	312	Thrust	7.0	22.7	0.55
21	1999	Chi-Chi, Taiwan	CHY101	259	Thrust	7.6	32	0.44
22	1999	Chi-Chi, Taiwan	TCU045	705	Thrust	7.6	77.5	0.51
23	1971	San Fernando	LA – Hollywood Stor	316	Thrust	6.6	39.5	0.21
24	1976	Friuli, Italy	Tolmezzo	425	Thrust	6.5	20.2	0.35
25	1980	Irpinia, Italy	Bisaccia	496	/	6.9	21.3	0.94
26	1979	Montenegro	ST64	1083	Thrust	6.9	21.0	0.18
27	1997	Umbria – Marche	ST238	n/a	Normal	6.0	21.5	0.19
28	2000	South Iceland	ST2487	n/a	Strike-slip	6.5	13	0.16
29	2000	South Iceland (a.s.)	ST2557	n/a	Strike-slip	6.4	15.0	0.13
30	2003	Bingol	ST539	806	Strike-slip	6.3	14.0	0.30

Table 4.2 – Selected ground motions for time history analysis

In this study, the spectral pseudo-acceleration $S_{pa}(T_d, \xi_d)$, at the isolated period of the system T_d and for the damping ratio $\Pi_{\xi_d} = \xi_d$, has been assumed as IM. This choice is motivated by the fact that if all the records are normalized to $S_{pa}(T_d, \xi_d)$, then the normalized displacement response of a system with period T_d, damping ratio ξ_d and mounted on FP isolators is equal to one for each record and it is not affected by the record-to-record variability. In the performed analyses, the damping ratio ξ_d has been taken equal to zero, consistent with other works that assumed the friction as the only source of damping in the isolators (Ryan & Chopra, 2004).

4.3.1.3 *Seismic performance description*

This study has considered the following set of response parameters relevant to the performance of the isolated system:

- the maximum isolator displacement $u_{d,max}$;

- the maximum pier displacement relative to the isolator $u_{p,max}$;

- the maximum FPS elastic forces at the abutment and pier level $F_{el,a,max}$ and $F_{el,p,max}$;

- the maximum FPS frictional forces at the abutment and pier level $F_{fr,a,max}$ and $F_{fr,p,max}$.

These parameters may be expressed in dimensionless form, allowing then to identify optimal friction values independent of the structural characteristics:

$$\psi_{u,d} = \frac{u_{d,max}\,\omega_d^2}{S_{pa}(T_d)} = \frac{u_{d,max}\,\omega_d^2}{IM} \tag{4.24}$$

$$\psi_{u,p} = \frac{u_{d,max}\,\omega_d^2}{S_{pa}(T_d)} = \frac{u_{d,max}\,\omega_d^2}{IM} \tag{4.25}$$

$$F_{b,i} = F_{el,i,max} + F_{fr,i,max} \qquad with \;\; i = p, a \tag{4.26}$$

$$\psi_{F_{b,p}} = \frac{\left|F_{b,p}\right|_{max}}{(m_d + \sum m_{p,i})S_{pa}(T_d)} = \frac{\left|F_{b,p}\right|_{max}}{(m_d + \sum m_{p,i}) \cdot IM} \tag{4.27}$$

$$\psi_{F_{b,a}} = \frac{\left|F_{b,a}\right|_{max}}{m_d\,S_{pa}(T_d)} = \frac{\left|F_{b,a}\right|_{max}}{m_d \cdot IM} \tag{4.28}$$

By repeatedly solving the dimensionless equations for the thirty ground motions records, a set of samples is obtained for each output variable used to monitor the seismic performance. In this study, the response parameters are assumed to follow a lognormal distribution, since it has a positive definition domain, from zero to infinite. The lognormality assumption permits to estimate, with a limited number of samples, the response at different percentile levels, which is very useful for system reliability assessment. It also permits to obtain a closed-form analytical estimate of the seismic risk (Castaldo, Palazzo, & Della Vecchia, 2015).

A lognormal distribution may be fitted to the generic response parameter D (i.e. the extreme values ψ_{u_d}, ψ_{u_p}, $\psi_{F_{b,p}}$ and $\psi_{F_{b,a}}$) by estimating the sample geometric mean $GM(D)$ and the sample lognormal standard deviation $\sigma_{\ln}(D)$, or dispersion $\beta(D)$, defined as follows:

$$GM(D) = \sqrt[N]{d_1 \cdot \ldots \cdot d_N} \tag{4.29}$$

$$\beta(D) = \sigma_{\ln}(D) = \sqrt[N]{\frac{(\ln d_1 - \ln[GM(D)])^2 + \cdots + (\ln d_N - \ln[GM(D)])^2}{N-1}} \tag{4.30}$$

where d_i denotes the ith sample value of D and N is the total number of samples. The sample GM is an estimator of the median of the response and its logarithm coincides with the lognormal sample mean $\mu_{\ln}(D)$. For small values, for example, below 0.3, the dispersion $\beta(D)$ is approximately equal to the coefficient of variation of the distribution (Cornell, Jalayer, Hamburger, & Foutch, 2002). Under the lognormality assumption, the relation between $GM(D)$, $\beta(D)$ and the kth percentile of the generic response parameter D may be expressed as:

$$d_k = GM(D)e^{f(k)\beta(D)} \tag{4.31}$$

where $f(k)$ is a function assuming the values $f(50) = 0$, $f(84) = 1$ and $f(16) = -1$ (Ang & Tang, 2007).

4.3.2 *Evolution of the model*

The equations of motion described in §4.2 are the basis for the development of an algorithm that may consider the pier – abutment interaction.

Firstly, it has been modelled in the MATLAB & Simulink® environment the n+1 dof system with $n = 1$ (Figure 4.4). The two dof system equations have been implemented within Simulink®, considering the nonlinearity of the sliding devices behaviour governed by Equation 4.4.

$$u_d = v_d + v_p$$
$$u_p = v_p$$
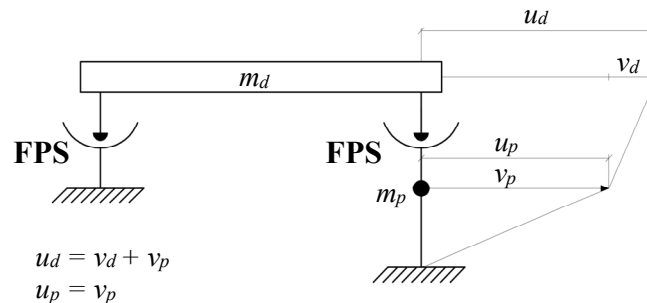
Figure 4.4 – Mathematical 2 dof bridge model

In Figure 4.5 it is illustrated the Simulink® diagram: the input signal a_g is at first multiplied by a *gain* which makes it be dimensionless in relation to the mass, then it is integrated twice, so that velocities and displacements may be determined. The type of integration is defined as *step-by-step integration*, since acceleration and velocity are integrated at each cycle, in order to better approximate the results. Simultaneously, the dimensionless velocity vector enters the *Gain 2* and the *Gain 7, 8, 9* packet: in the first case it is multiplied by the damping matrix and then it comes back into the system; in the second, it enters the two "packets" reproducing the mechanics of the FPS behaviour (Efraim & Blostotsky, 2012) and it generates the frictional term of the restoring forces at the abutment and pier level (Equations 4.12 and 4.13). The dimensionless vector of the displacements enters the *Gains 1, 5, 11*: in the first case it is multiplied by the total stiffness matrix (i.e. the sum of $[K]$ and $[K]_1$, Equation 4.15), while in the second it then generates the elastic term of the FPS forces at the abutment and pier level.

Figure 4.5 – Simulink® diagram to solve the 2 dof model's dynamic equations considering the pier – abutment interaction

The stability of the algorithm has been tested by performing two types of integration, in order to attain the most accurate approximation of the results. Accordingly, the analysis has been implemented with fixed input parameters, considering a fixed-step (*ode3*, step 0.001 s) and a variable-step (*ode23tb*, step from 0.01 s to 0.00001 s) integration.

Figure 4.6 – Comparison between variable and fixed-step integration results for $T_p = 0.05s$, $T_d = 2s$, $\lambda = 0.1$
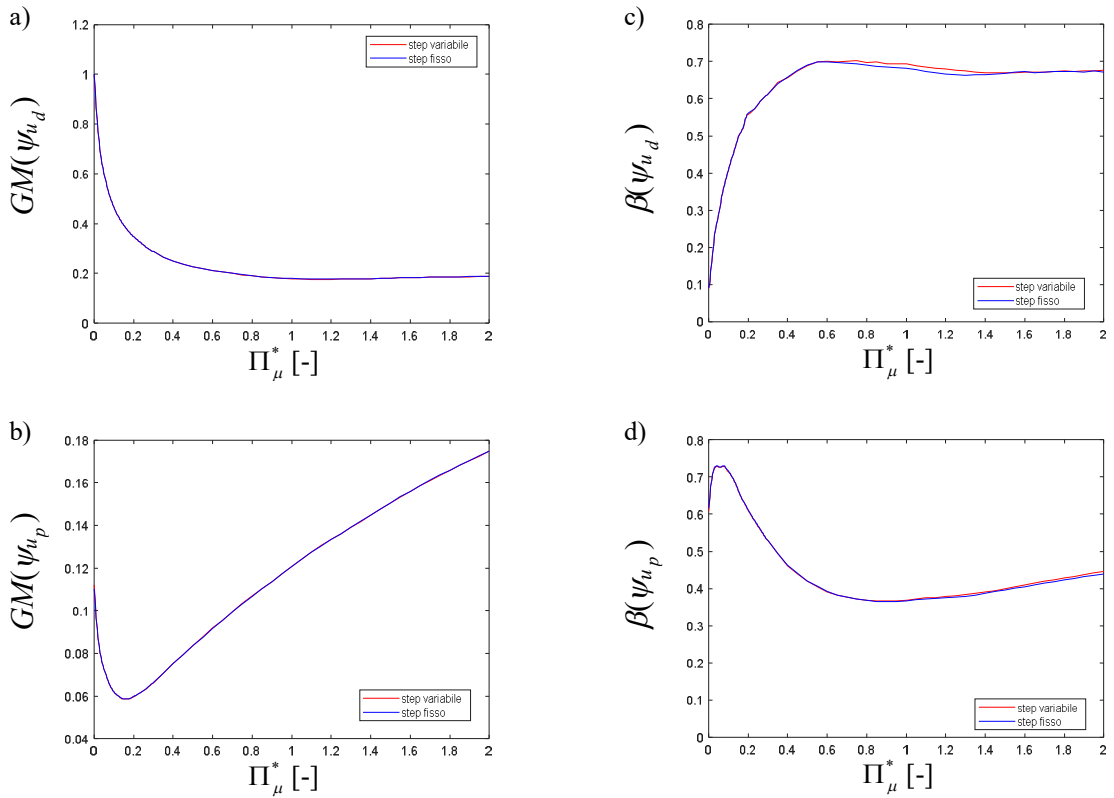
Figure 4.7 – Comparison between variable and fixed-step integration results for $T_p = 0.2s$, $T_d = 2s$, $\lambda = 0.2$

Figures 4.6 and 4.7 show that variable-step results are much more stable than fixed-step ones: this is due to the better approximation that characterizes each integration step. In fact, the fixed-step approach does not look after the precision of the solution, as it approximates the results in a constant way to the third decimal point, while the variable-step approach looks for the best approximation of the function in a range that varies from the second to the fifth decimal point. Clearly, the variable-step integration leads to a computational time higher than that of the fixed-step one. Besides, unstable parameters, such as very low T_p values (0.05 s), having an intrinsic high computational time, make the variable-step integration increase even more the computing burden.

4.4   *MODELLING IN SAP2000®*

The accuracy of the results produced by the MATLAB & Simulink® algorithm has been validated by making a comparison with the same three dof model implemented in the professional software SAP 2000®.

They have been defined the abutment and the two dof pier as rigidly connected by the deck. Between the substructure and the superstructure, it has been inserted the isolating friction pendulum device, modelling it by means of the nonlinear *NLlink* finite element, which shows a nonlinear biaxial behaviour and allows to model a 3D friction slider isolator. It was also possible to define a *Gap element* in the vertical direction, in order to represent the only compressive resistance of the device (Figure 4.8).
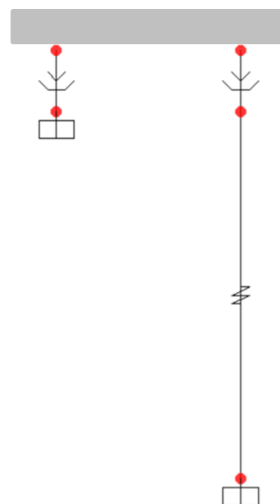
Figure 4.8 – Mathematical 2 dof bridge model implemented in SAP2000®

4.4.1 *Numerical validation of the model*

The validation of the model has been performed by comparing the results of the MATLAB & Simulink® analysis with those of the SAP2000® one, for a single earthquake excitation. Different solutions for specific T_p, T_d, λ and μ values have been compared.

In the following Figures 4.9 to 4.12 it is shown the comparison between: deck displacements; pier displacements; FPS hysteresis cycles, denoting the dependence on velocity. It may be clearly seen how the MATLAB & Simulink® results are very similar to the SAP2000® ones, so that the implemented model may be considered to be validated.
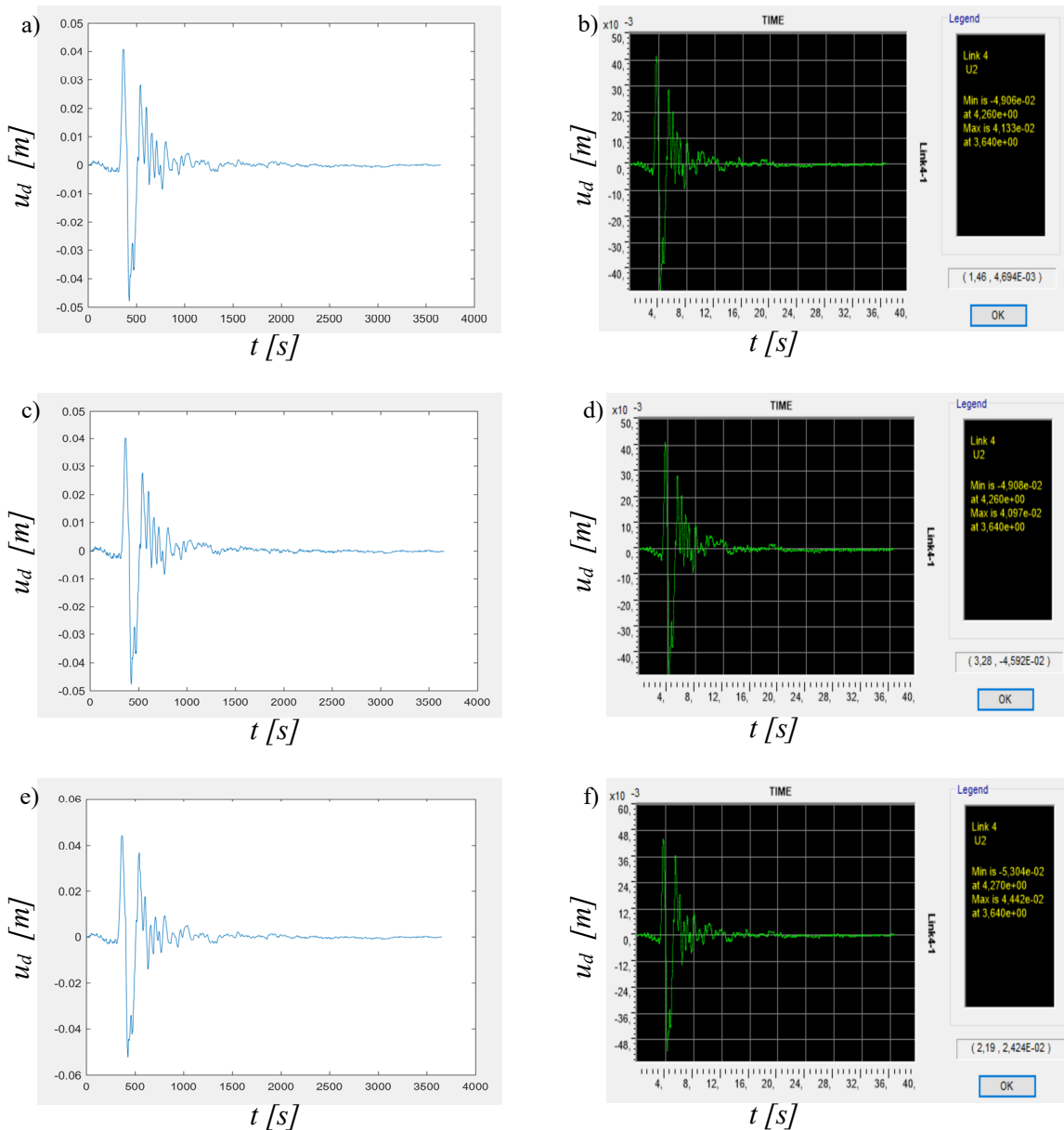
Figure 4.9 – MATLAB® vs SAP2000® results comparison in terms of deck displacements: a) and b) for $f_{max} = 0.03$, $f_{min} = 0.01$; c) and d) for $f_{max} = 0.03$, $f_{min} = 0.015$; e) and f) for $f_{max} = 0.025$, $f_{min} = 0.01$
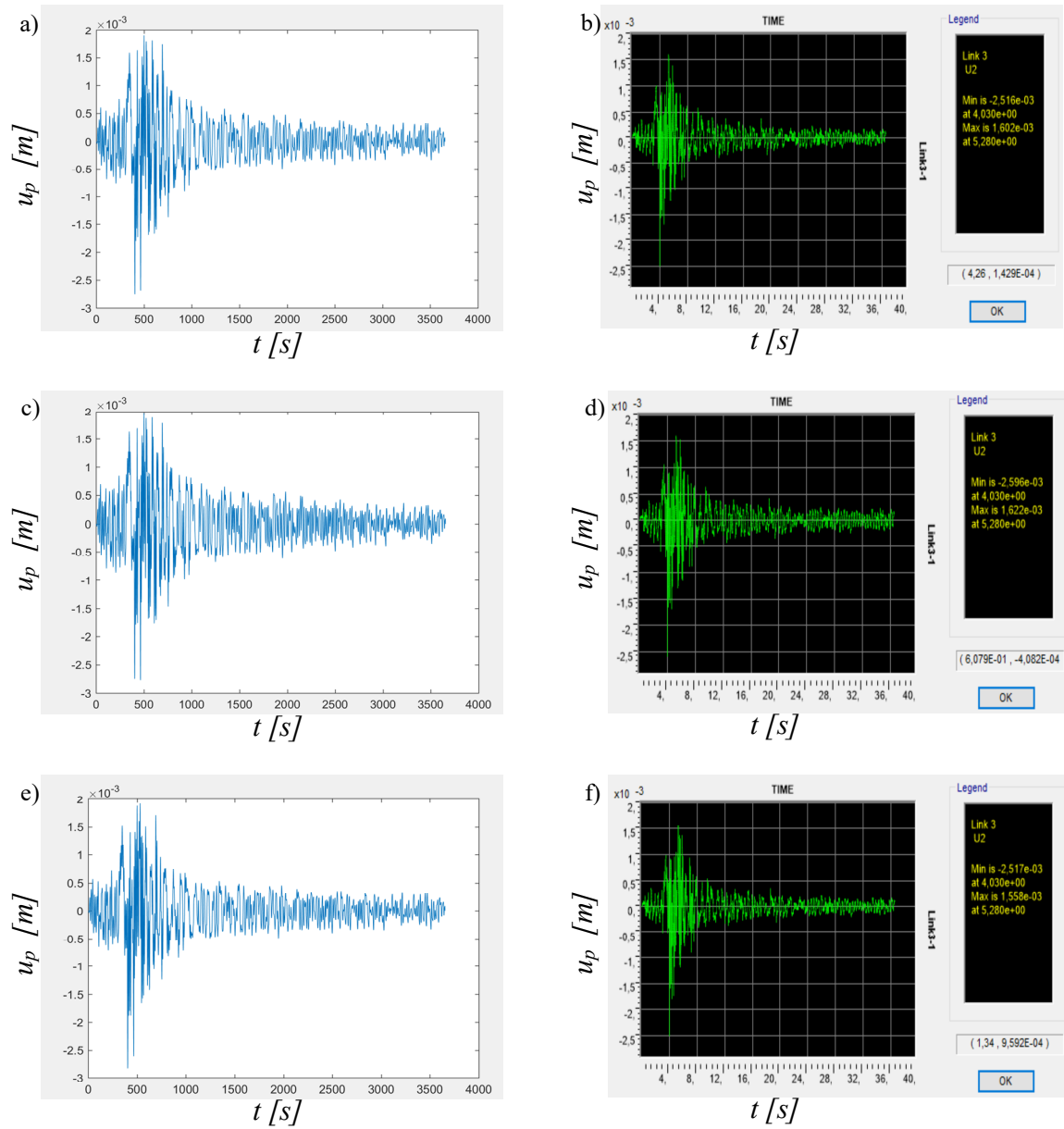
Figure 4.10 – MATLAB® vs SAP2000® results comparison in terms of pier displacements:
a) and b) for $f_{max} = 0.03$, $f_{min} = 0.01$; c) and d) for $f_{max} = 0.03$, $f_{min} = 0.015$; e) and f)
for $f_{max} = 0.025$, $f_{min} = 0.01$
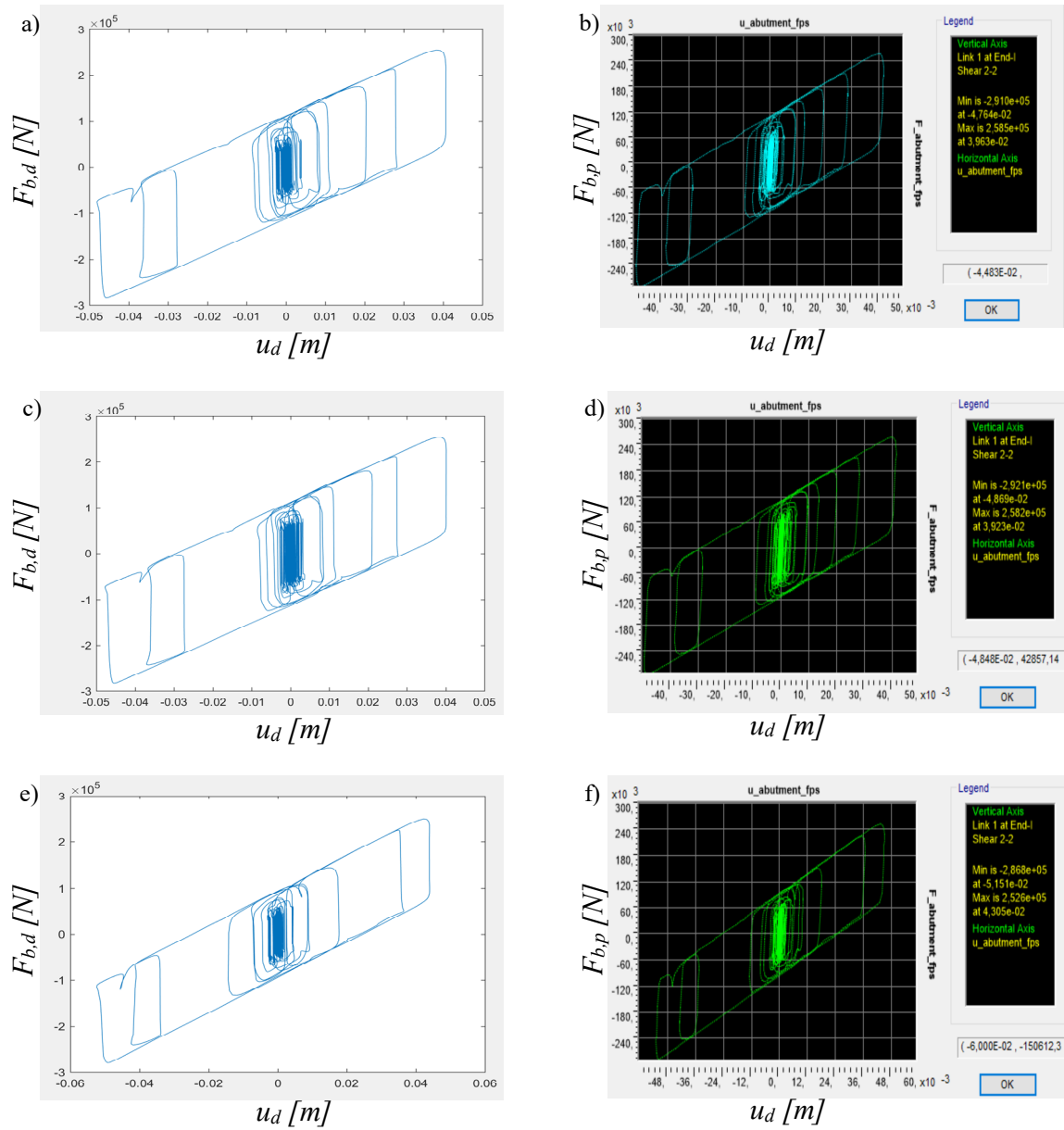
Figure 4.11 – MATLAB® vs SAP2000® results comparison in terms of deck velocity dependence: a) and b) for $f_{max} = 0.03$, $f_{min} = 0.01$; c) and d) for $f_{max} = 0.03$, $f_{min} = 0.015$; e) and f) for $f_{max} = 0.025$, $f_{min} = 0.01$
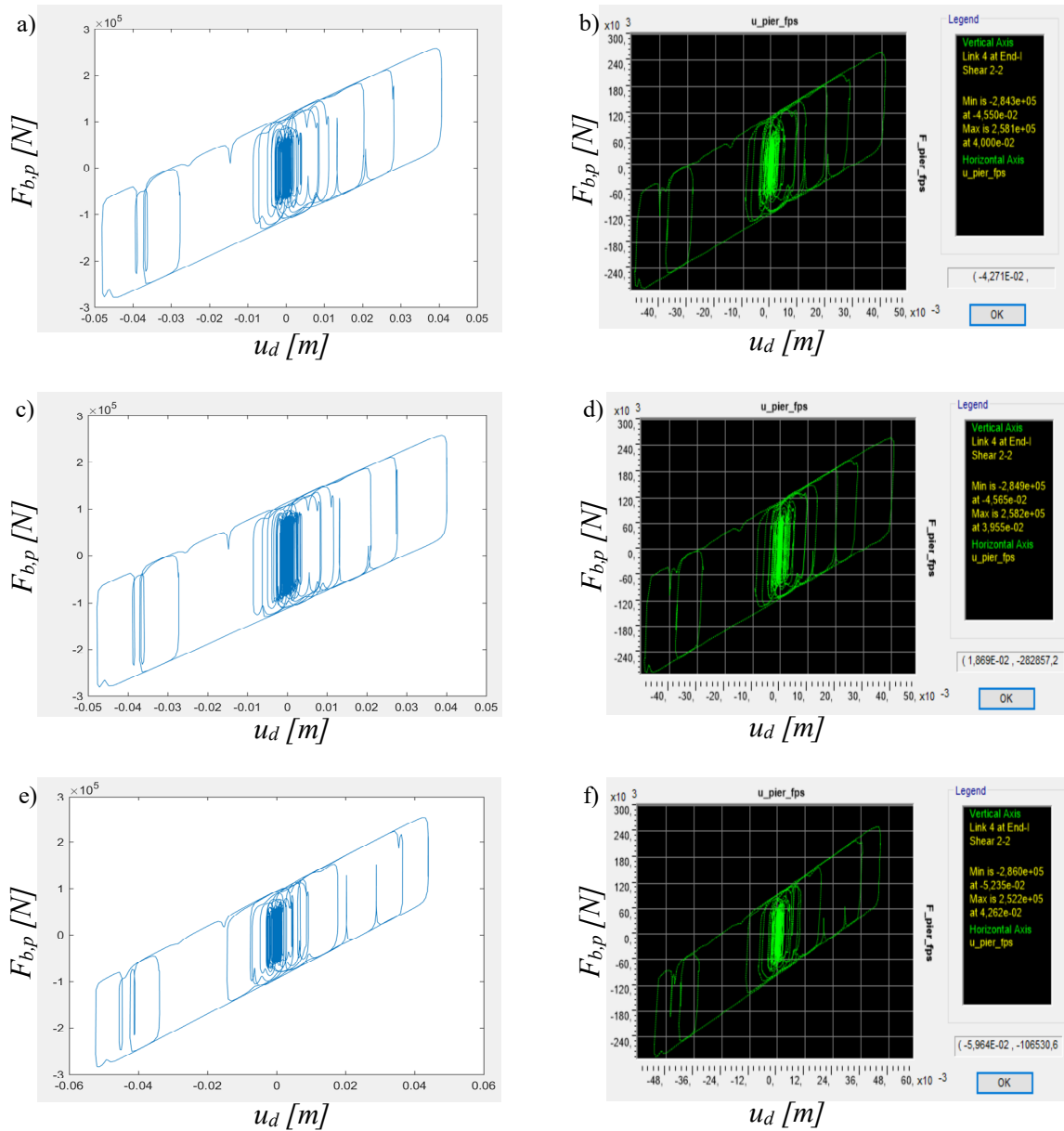
Figure 4.12 – MATLAB® vs SAP2000® results comparison in terms of pier velocity dependence: a) and b) for $f_{max} = 0.03$, $f_{min} = 0.01$; c) and d) for $f_{max} = 0.03$, $f_{min} = 0.015$; e) and f) for $f_{max} = 0.025$, $f_{min} = 0.01$

4.5   INFLUENCE OF HIGHER MODES

Once the stability of the algorithm has been identified and the *2* dof model has been validated, it was possible to carry out a higher discretization of the pier to further refine the solution. This way, a *5+1* dof system has been implemented (Figure 4.13 and 4.14) and then its accuracy in solution has been tested by performing the analysis of a *7+1* dof model (Figure 4.15 and 4.16), so that it was possible to investigate how much two additional dof improved both the convergence and the stability of the solution. By performing the

MATLAB & Simulink® analyses with different dof, it has been calculated and compared the maximum seismic response in terms of geometric mean GM and dispersion β of pier and deck displacements, in function of the dimensionless parameter Π_μ^* and for a single earthquake excitation.

$$u_d = v_d + v_{p,5} + v_{p,4} + v_{p,3} + v_{p,2} + v_{p,1}$$
$$u_{p,5} = v_{p,5} + v_{p,4} + v_{p,3} + v_{p,2} + v_{p,1}$$
$$u_{p,4} = v_{p,4} + v_{p,3} + v_{p,2} + v_{p,1}$$
$$u_{p,3} = v_{p,3} + v_{p,2} + v_{p,1}$$
$$u_{p,2} = v_{p,2} + v_{p,1}$$
$$u_{p,1} = v_{p,1}$$
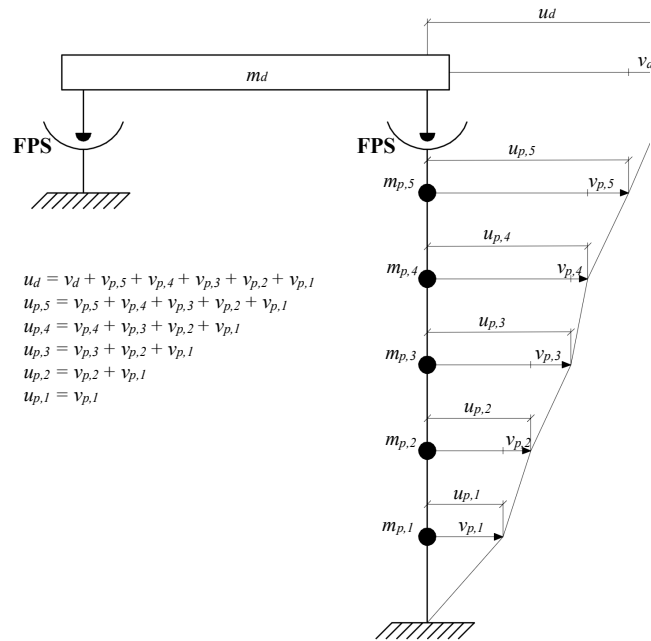
Figure 4.13 – Mathematical 5+1 dof bridge model
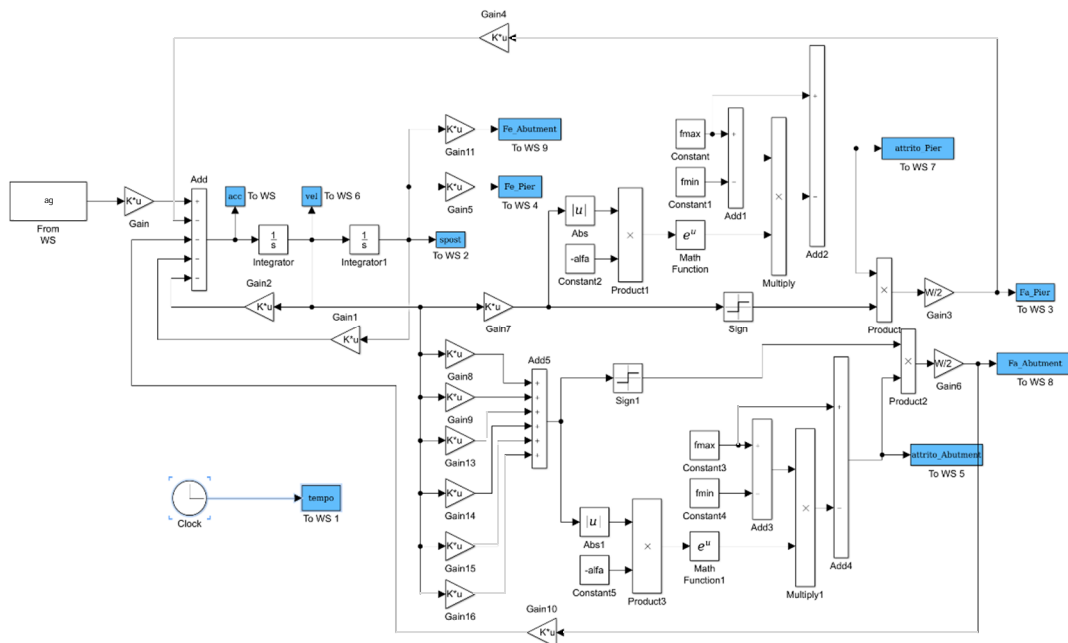
Figure 4.14 – Simulink® diagram to solve the 5+1 dof model's dynamic equations considering the pier – abutment interaction

$$u_d = v_d + v_{p,7} + v_{p,6} + v_{p,5} + v_{p,4} + v_{p,3} + v_{p,2} + v_{p,1}$$
$$u_{p,7} = v_{p,7} + v_{p,6} + v_{p,5} + v_{p,4} + v_{p,3} + v_{p,2} + v_{p,1}$$
$$u_{p,6} = v_{p,6} + v_{p,5} + v_{p,4} + v_{p,3} + v_{p,2} + v_{p,1}$$
$$u_{p,5} = v_{p,5} + v_{p,4} + v_{p,3} + v_{p,2} + v_{p,1}$$
$$u_{p,4} = v_{p,4} + v_{p,3} + v_{p,2} + v_{p,1}$$
$$u_{p,3} = v_{p,3} + v_{p,2} + v_{p,1}$$
$$u_{p,2} = v_{p,2} + v_{p,1}$$
$$u_{p,1} = v_{p,1}$$
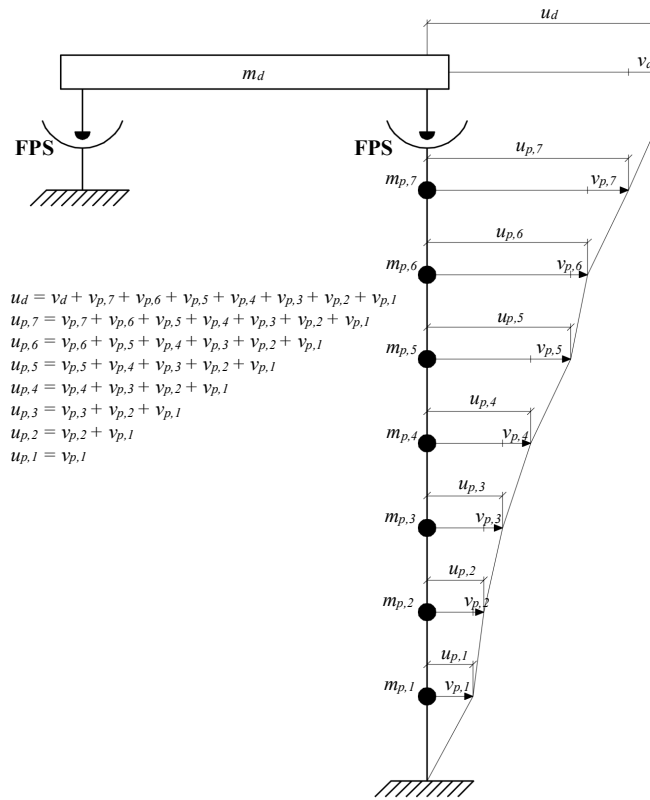
Figure 4.15 – Mathematical 7+1 dof bridge model
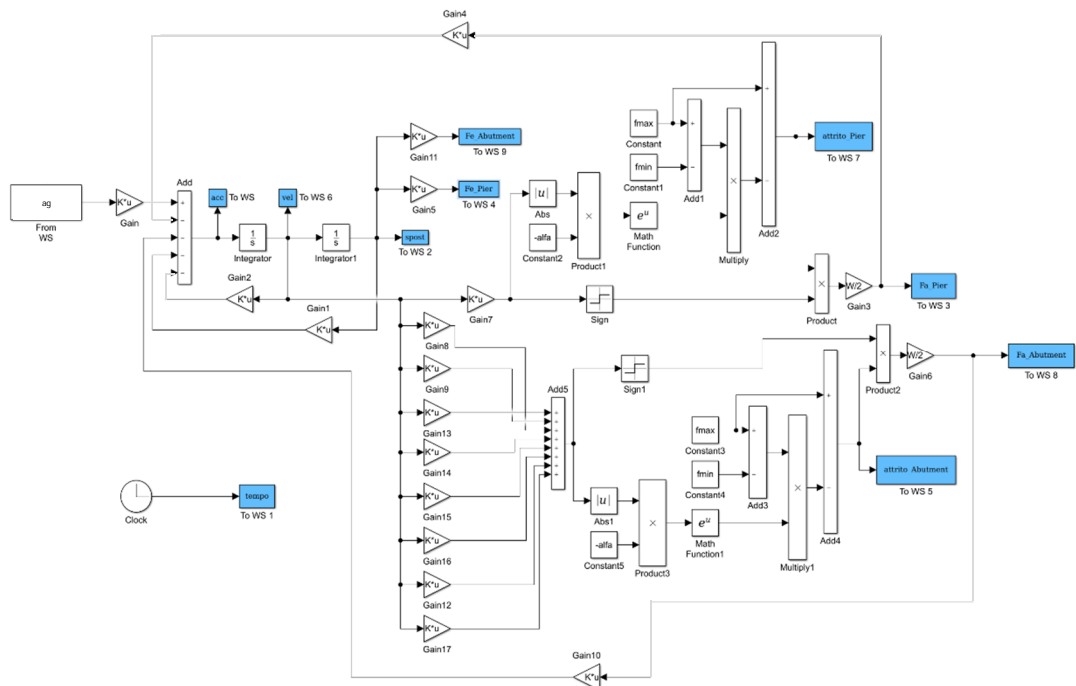
Figure 4.16 – Simulink® diagram to solve the 7+1 dof model's dynamic equations considering the pier – abutment interaction

As shown in the following Figure 4.17, *5+1* and *7+1* dof models converge better than *1+1* dof one. Besides, between them there are very small differences. Hence, with the purpose to save on computing time, it may be stated that the definitive model adopted in the study is the *5+1* dof one.
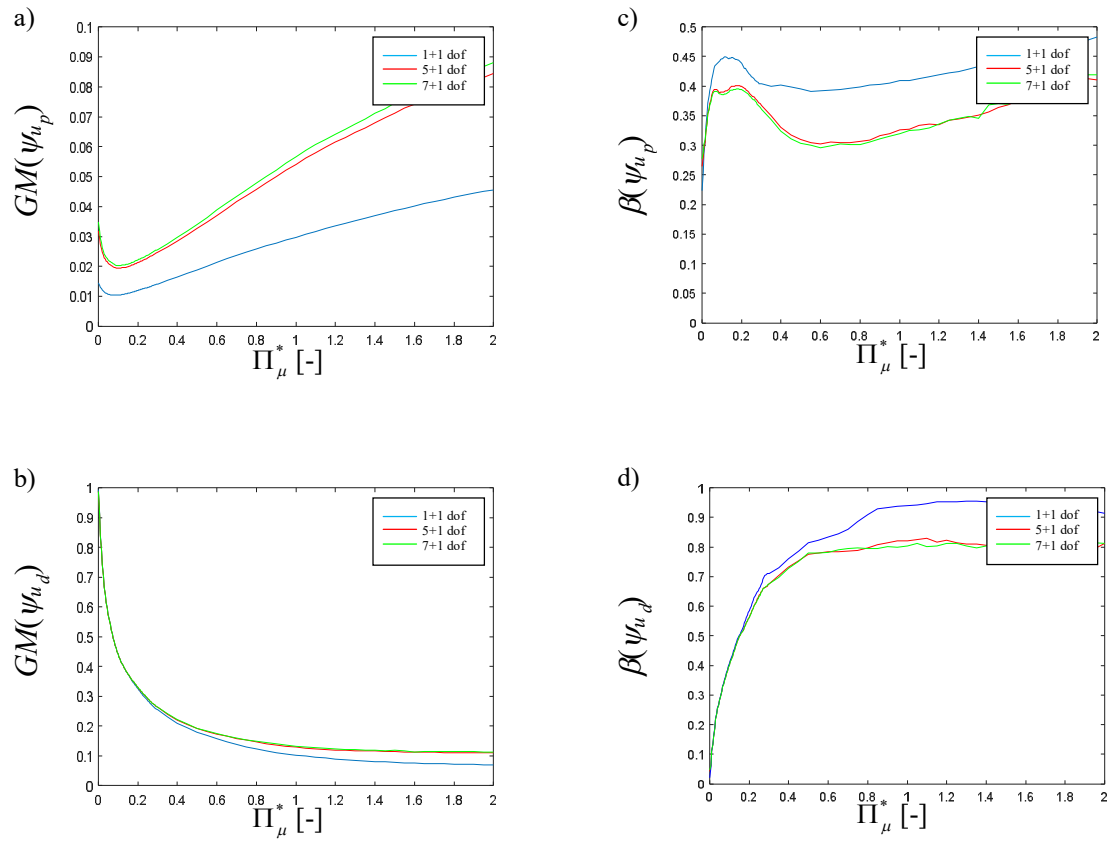
Figure 4.17 – Comparison between different models to evaluate their convergence

5

PARAMETRIC ANALYSIS RESULTS

This chapter presents the results of an extensive parametric study carried out on the *5+1* dof model, described in the previous §4.5, to evaluate the relation between the isolating system and structure properties and the performance of bridges isolated with FPS bearings.

5.1 *RESULTS OBTAINED IN MATLAB & SIMULINK®*

The results achieved by implementing the MATLAB & Simulink® model are a combination of 5700 T_p, T_d, Π_λ and Π_μ^* values.

The parameters Π_{ξ_d} and Π_{ξ_p} have been assumed respectively equal to 0% and 5%, the mass ratio Π_λ was varied in the range between 0.1 and 0.2, Π_μ^* in the range between 0 (no friction) and 2 (very high friction), the base-isolated system period T_d in the range between 2 and 4 s and the pier period T_p in the range between 0.05 and 0.2 s, so that the parameter Π_ω varied in the range between 10 (rigid superstructure) and 80 (flexible superstructure). For each value of the parameters varied in the parametric study, the differential equations of motion have been repeatedly solved for the different considered ground motions scaled to a common value of $S_{pa}(T_d)$. It is noteworthy that the dimensionless response is independent on the choice of the *IM* value. The Runge–Kutta–Fehlberg integration algorithm available in MATLAB & Simulink® has been employed for its ability of automatically adjusting the time-integration step size, thus improving the solution accuracy. The probabilistic properties of the normalized response have been evaluated by estimating the geometric mean *GM* and the dispersion β of the parameters of interest through Equations 4.29 and 4.30, §4.3.1.3.

Figures 5.1 to 5.8 show the statistics of the response parameters ψ_{u_d}, ψ_{u_p}, $\psi_{F_{b,p}}$ and $\psi_{F_{b,a}}$, obtained for different values of the system parameters varying in the range of interest. In particular, the geometric mean is represented on the left column and the dispersion on the right one. Each figure contains several surface plots in function of the ninety-five Π_μ^* and five T_d values considered, corresponding to the three different values of Π_λ. In addition, the *GM* and β values are referred to a specific period T_p.
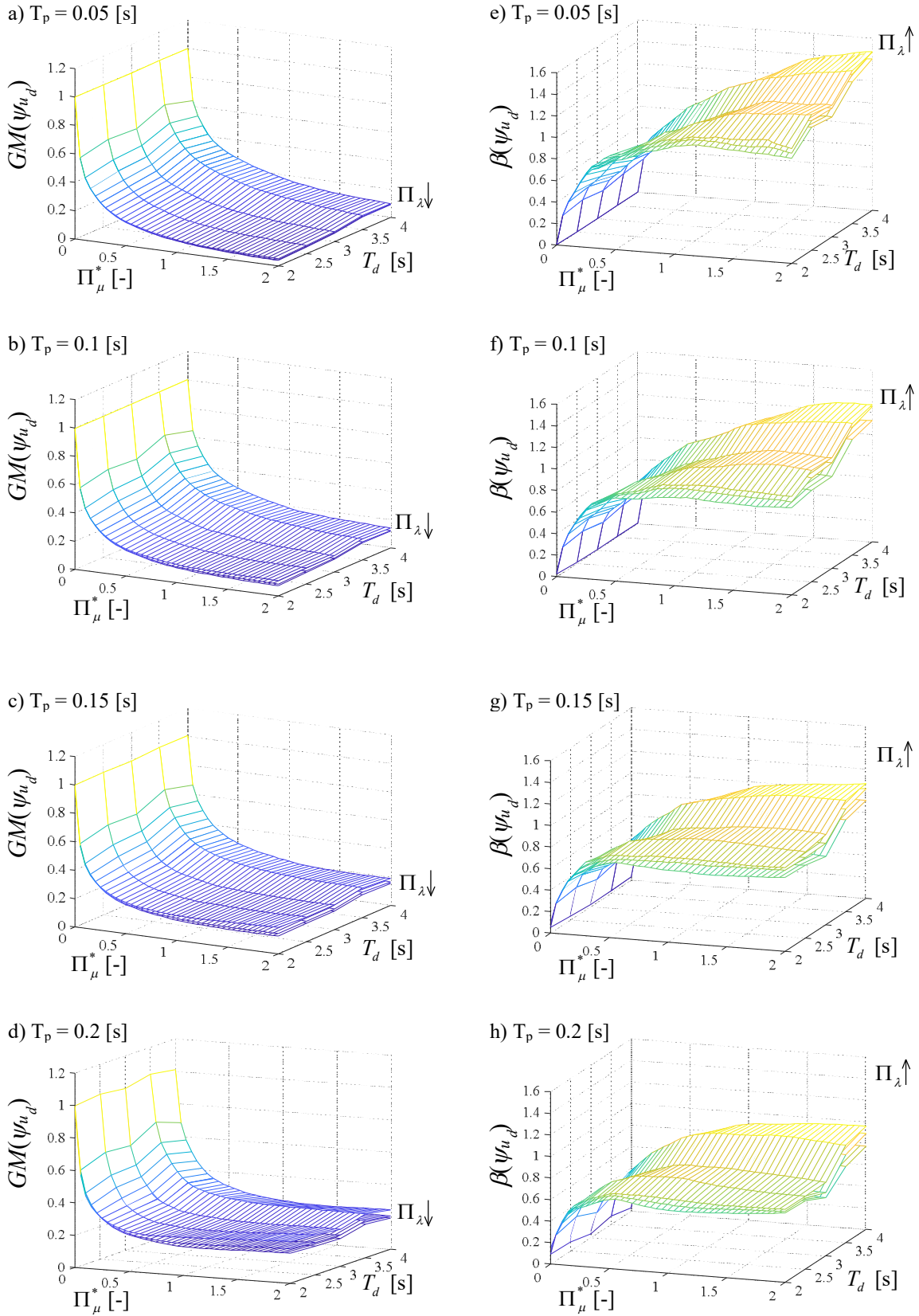
Figure 5.1 – Normalized deck displacement versus Π_μ^* and T_d: median value and dispersion for fixed values of T_p and different values of Π_λ. The arrow denotes the increasing direction of Π_λ
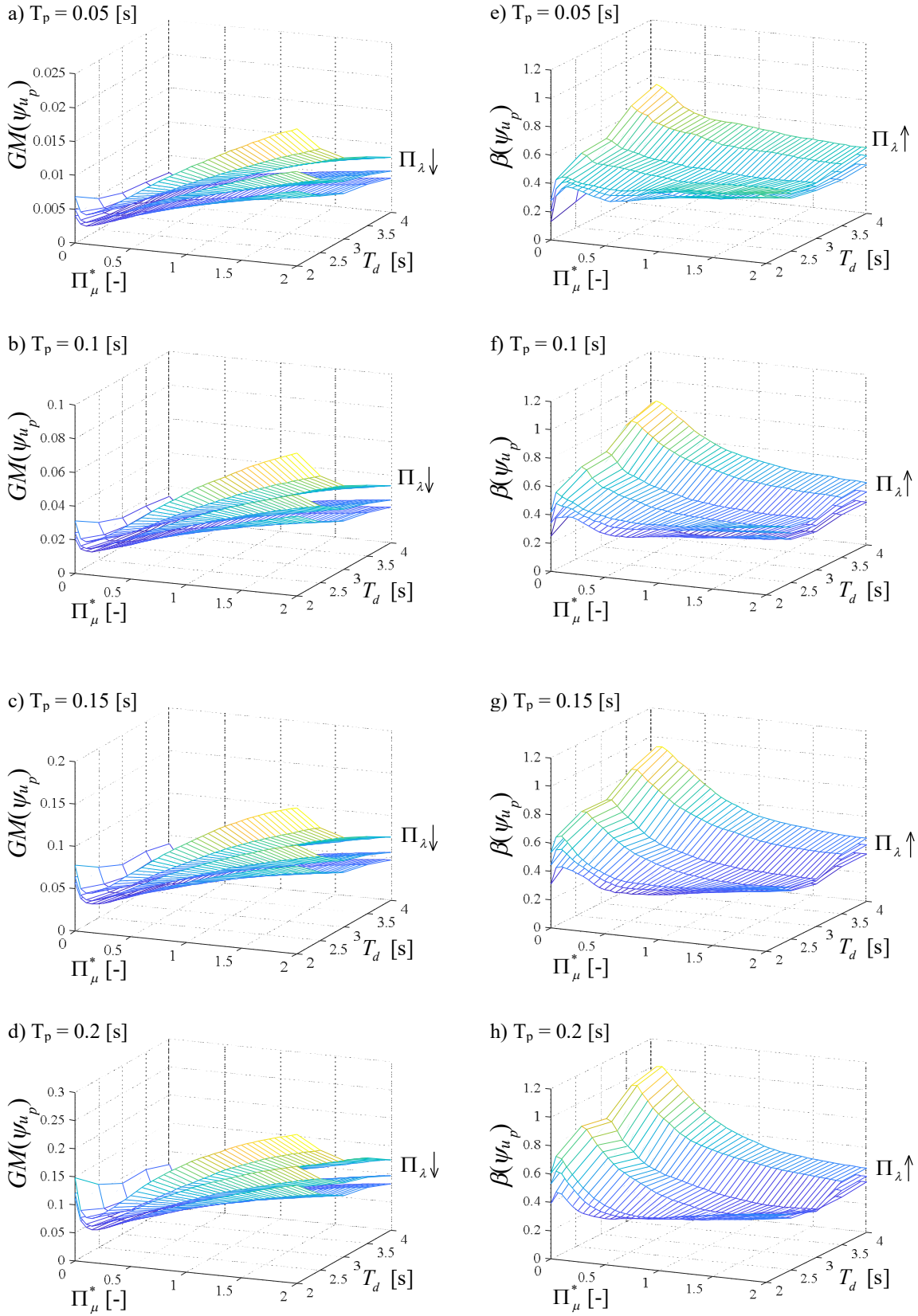
Figure 5.2 – Normalized pier displacement versus Π_μ^* and T_d: median value and dispersion for fixed values of T_p and different values of Π_λ. The arrow denotes the increasing direction of Π_λ
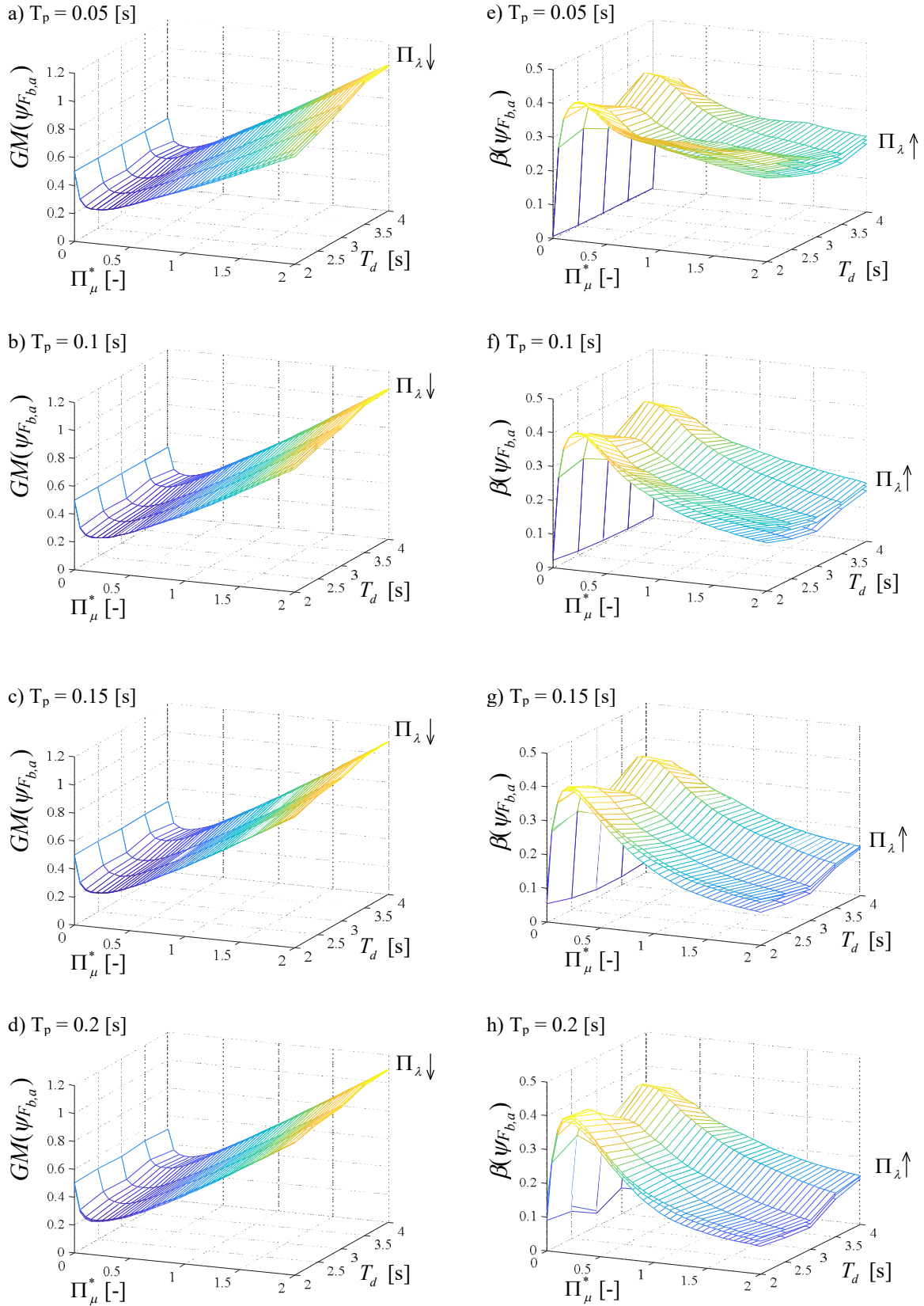
Figure 5.3 – Normalized bearing force at abutment level versus Π_μ^* and T_d: median value and dispersion for fixed values of T_p and different values of Π_λ. The arrow denotes the increasing direction of Π_λ

a) T_p = 0.05 [s]

e) T_p = 0.05 [s]

b) T_p = 0.1 [s]

f) T_p = 0.1 [s]

c) T_p = 0.15 [s]

g) T_p = 0.15 [s]

d) T_p = 0.2 [s]

h) T_p = 0.2 [s]
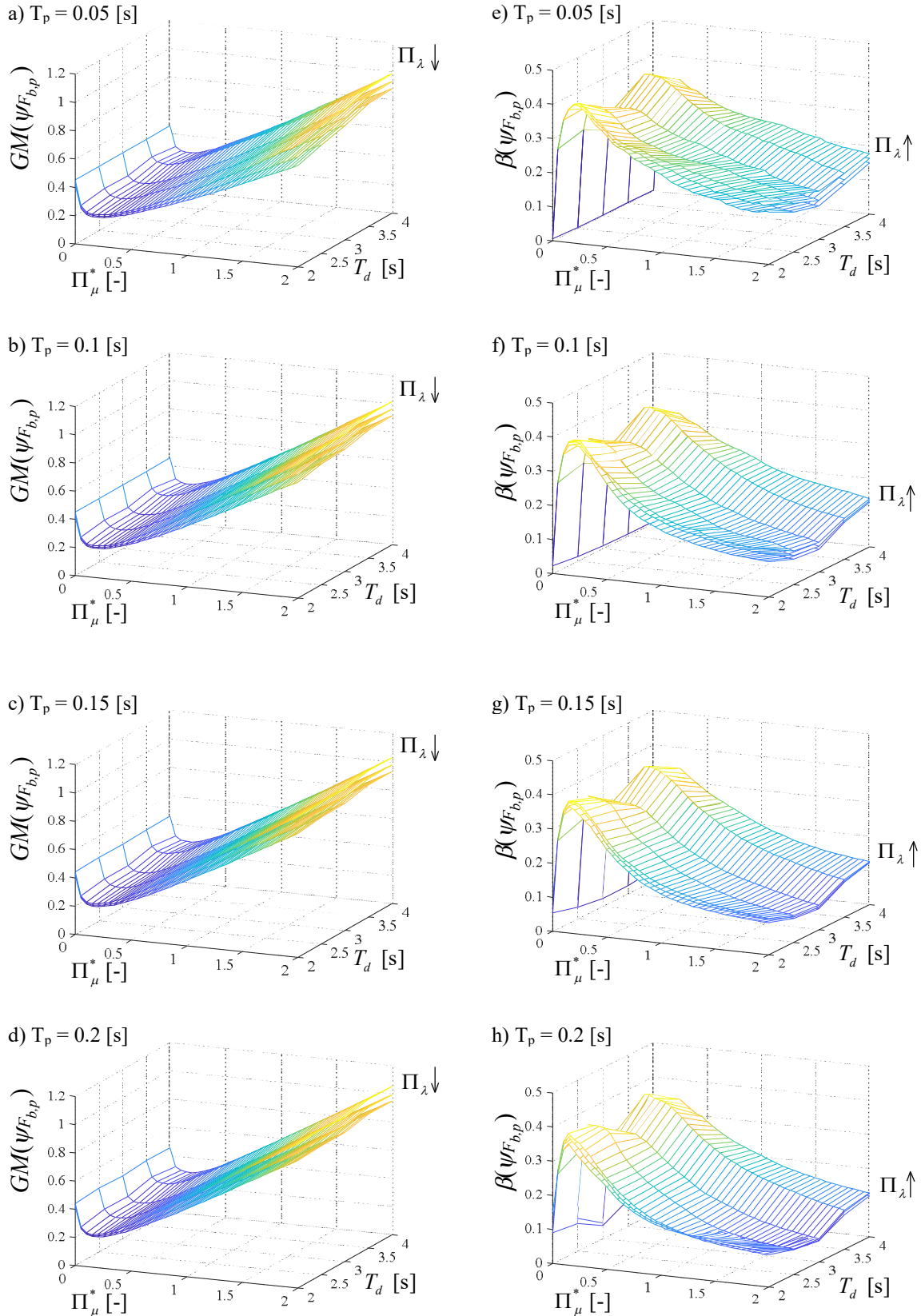
Figure 5.4 – Normalized bearing force at pier level versus Π_μ^* and T_d: median value and dispersion for fixed values of T_p and different values of Π_λ. The arrow denotes the increasing direction of Π_λ
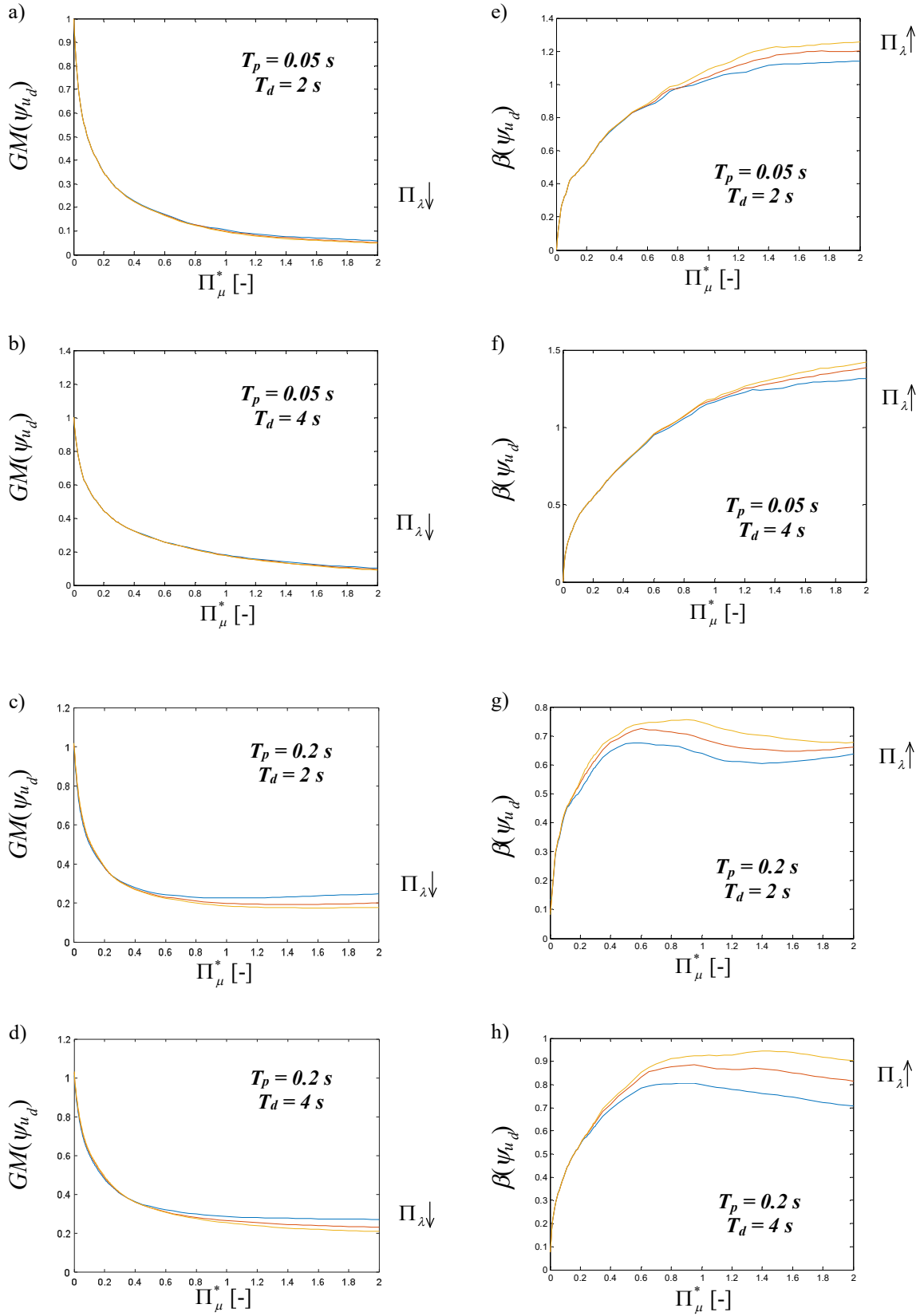
Figure 5.5 – Normalized deck displacement versus Π_μ^*: median value and dispersion for fixed values of T_p and T_d and different values of Π_λ. The arrow denotes the increasing direction of Π_λ
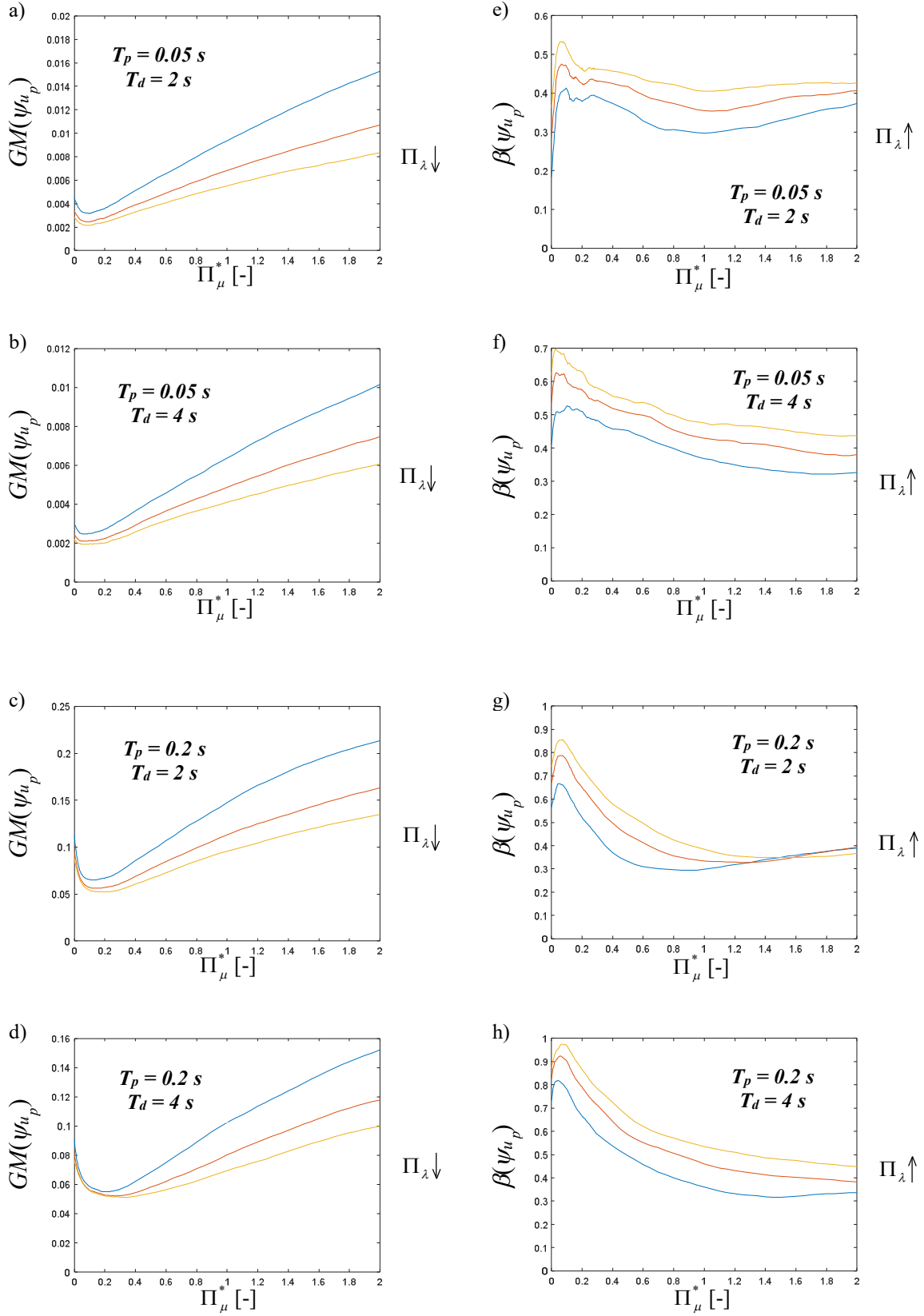
Figure 5.6 – Normalized pier displacement versus Π_μ^*: median value and dispersion for fixed values of T_p and T_d and different values of Π_λ. The arrow denotes the increasing direction of Π_λ
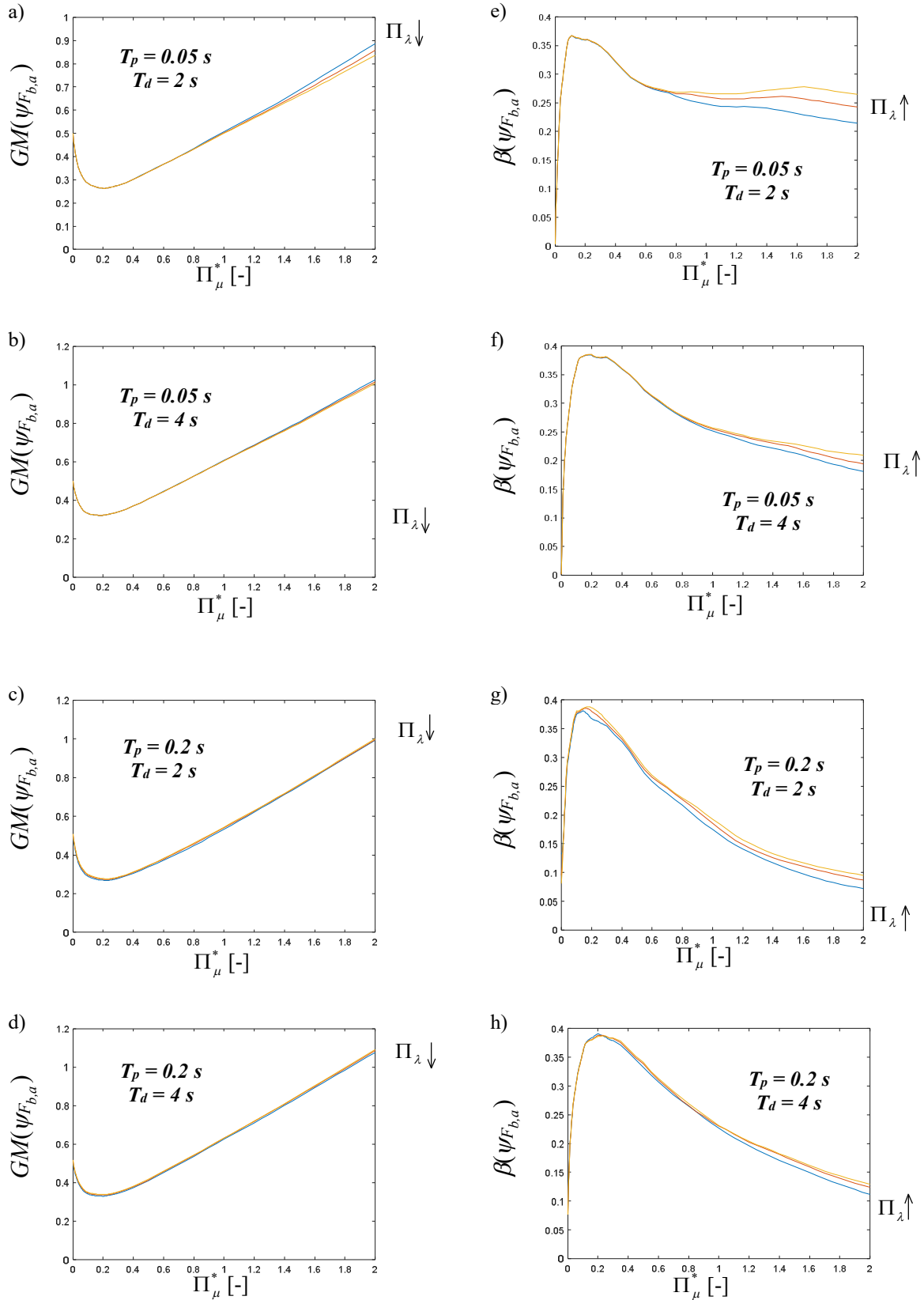
Figure 5.7 – Normalized bearing force at abutment level versus Π_μ^*: median value and dispersion for fixed values of T_p and T_d and different values of Π_λ. The arrow denotes the increasing direction of Π_λ
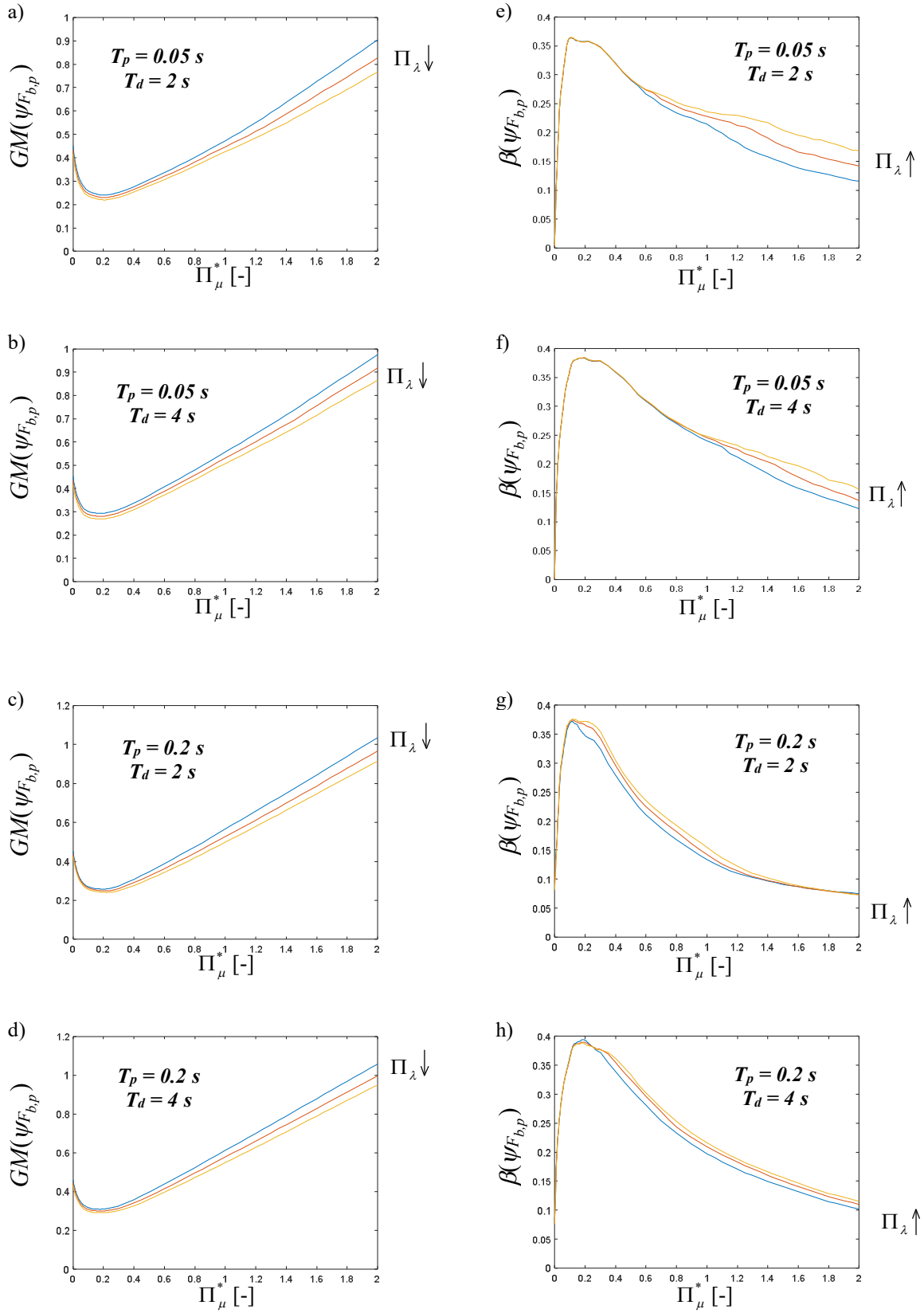
Figure 5.8 – Normalized bearing force at pier level versus Π_μ^*: median value and dispersion for fixed values of T_p and T_d and different values of Π_λ. The arrow denotes the increasing direction of Π_λ

In Figure 5.1 are plotted the results concerning the normalized deck displacement ψ_{u_d}. The geometric mean $GM(\psi_{u_d})$ is equal to unit for $\Pi_\mu^* = 0$ (reference situation of isolated structure on frictionless devices). Obviously, $GM(\psi_{u_d})$ significantly decreases as Π_μ^* increases. The values of $GM(\psi_{u_d})$ are only slightly influenced by Π_λ, which controls the contribution of the higher modes of vibration to the response. For low T_p values, i.e., cases a) and b), the influence of Π_λ on $GM(\psi_{u_d})$ is negligible because the substructure is rigid, whereas in the cases c) and d), the values of $GM(\psi_{u_d})$ decrease by increasing Π_λ, that is, by increasing the pier inertia over that of the superstructure. The dispersion $\beta(\psi_{u_d})$ increases for increasing values of Π_μ^*, as a result of the reduction in efficiency of the *IM* employed in the study. The mass ratio Π_λ has influence on the response dispersion especially in the case of high T_p values. Obviously, in the reference situation corresponding to $\Pi_\mu^* = 0$ and very low T_p value, the dispersion is nil for all the values of T_d and Π_λ considered.

Figure 5.2 shows the variation with the system parameters of the normalized substructure displacements ψ_{u_p}. The values of $GM\left(\psi_{u_p}\right)$ decrease for increasing values of T_d, as well as for increasing values of Π_λ. It is noteworthy that for low Π_μ^* values, $GM\left(\psi_{u_p}\right)$ decreases by increasing Π_μ^*, whereas for high Π_μ^* values, it increases by increasing Π_μ^*. Hence, there exists a critical value of Π_μ^* such that the substructure displacement is minimized. This critical value falls within the range between 0 and 0.35 depending on the values of T_d and Π_λ. The values of the dispersion $\beta\left(\psi_{u_p}\right)$ are very low for low Π_μ^* values because of the high efficiency of the IM employed in the study and attain their peak for values of Π_μ^* close to the critical one.

Figures 5.3 and 5.4 report the normalized bearing force at abutment and pier level, $\psi_{F_{b,a}}$ and $\psi_{F_{b,p}}$, for the different values of the characteristic response parameters. The values of $GM(\psi_{F_{b,a}})$ and $GM\left(\psi_{F_{b,p}}\right)$ are very sensitive to variations of Π_μ^*: in particular, by increasing Π_μ^*, the values of $GM(\psi_{F_{b,a}})$ and $GM\left(\psi_{F_{b,p}}\right)$ firstly decrease and then they increase and tend to a unit value. This reflects the fact that for high friction values or low seismic intensities, the normalized forces are controlled by the bearing friction rather than by the bearing stiffness. While $GM(\psi_{F_{b,a}})$ is very slightly affected by the values of the other variables (self-similarity property), Π_λ has the same effect on $GM\left(\psi_{F_{b,p}}\right)$ as on $GM\left(\psi_{u_p}\right)$.

In order to clearly show the internal variations in the graphs above, they have been plotted the two-dimensional sections of the diagrams, comparing the extreme values of each system parameter (Figures 5.5 to 5.8).

5.1.1 *Optimum Friction Values*

The existence of a critical, optimum value of the friction coefficient minimizing the substructure displacements was observed (Figure 5.2). The latter is the result of two counteracting effects that follow an increase of the friction coefficient. The first effect is an increase in energy dissipation, which reduces the substructure displacements. The second effect is the increase of the isolator strength (and thus of the equivalent stiffness, with a reduction of the corresponding equivalent fundamental vibration period), which on the other hand increases the substructure displacements.

It may be of interest to evaluate the critical normalized friction value $\Pi^*_{\mu,opt}$ that minimizes response percentile other than the 50th, corresponding to different exceedance probabilities (Ryan & Chopra, 2004).

Figures 5.9 and 5.10 report the variation of $\Pi^*_{\mu,opt}$ with Π_λ and T_p obtained by considering the minimization of the median (i.e. 50th percentile), the 16th percentile and the 84th percentile of the normalized substructure displacements ψ_{u_p}. It is observed that $\Pi^*_{\mu,opt}$ generally increases by increasing both Π_λ and T_p and by increasing the percentile level. Finally, according to Equation 4.23, §4.2.1, the critical friction coefficient linearly increases with the *IM* level, since:

$$f_{max,opt} = \frac{S_{pa}(T_d)}{g} \cdot \Pi^*_{\mu,opt} \qquad (5.1)$$

a) T_d = 2.0 [s]

b) T_d = 2.5 [s]

c) T_d = 3.0 [s]

d) T_d = 3.5 [s]

e) T_d = 4.0 [s]
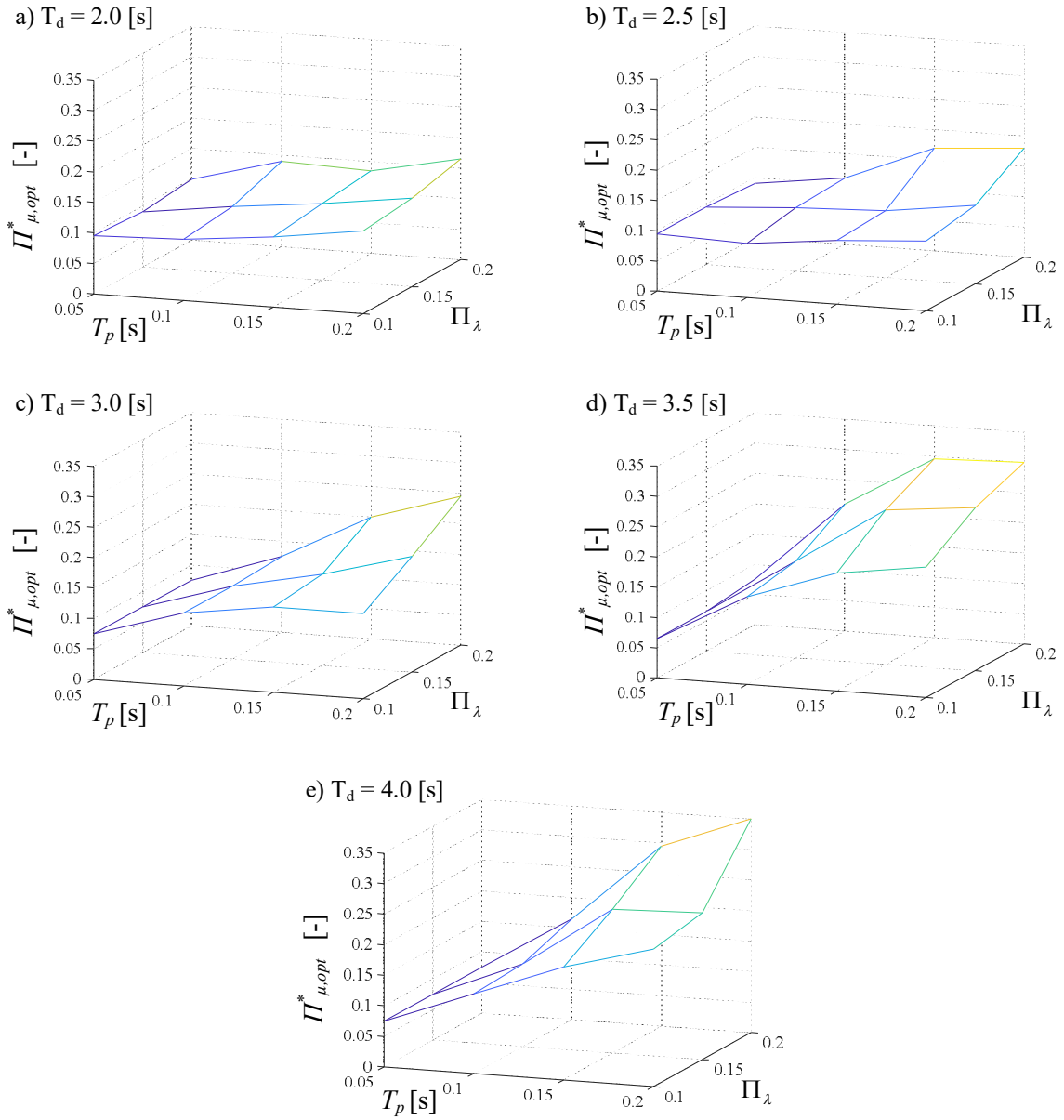
Figure 5.9 – Optimum values of normalized friction versus T_p and Π_λ with reference to the 50th percentile of ψ_{u_p}

a) $T_d = 2.0$ [s]

b) $T_d = 2.5$ [s]

c) $T_d = 3.0$ [s]

d) $T_d = 3.5$ [s]

e) $T_d = 4.0$ [s]
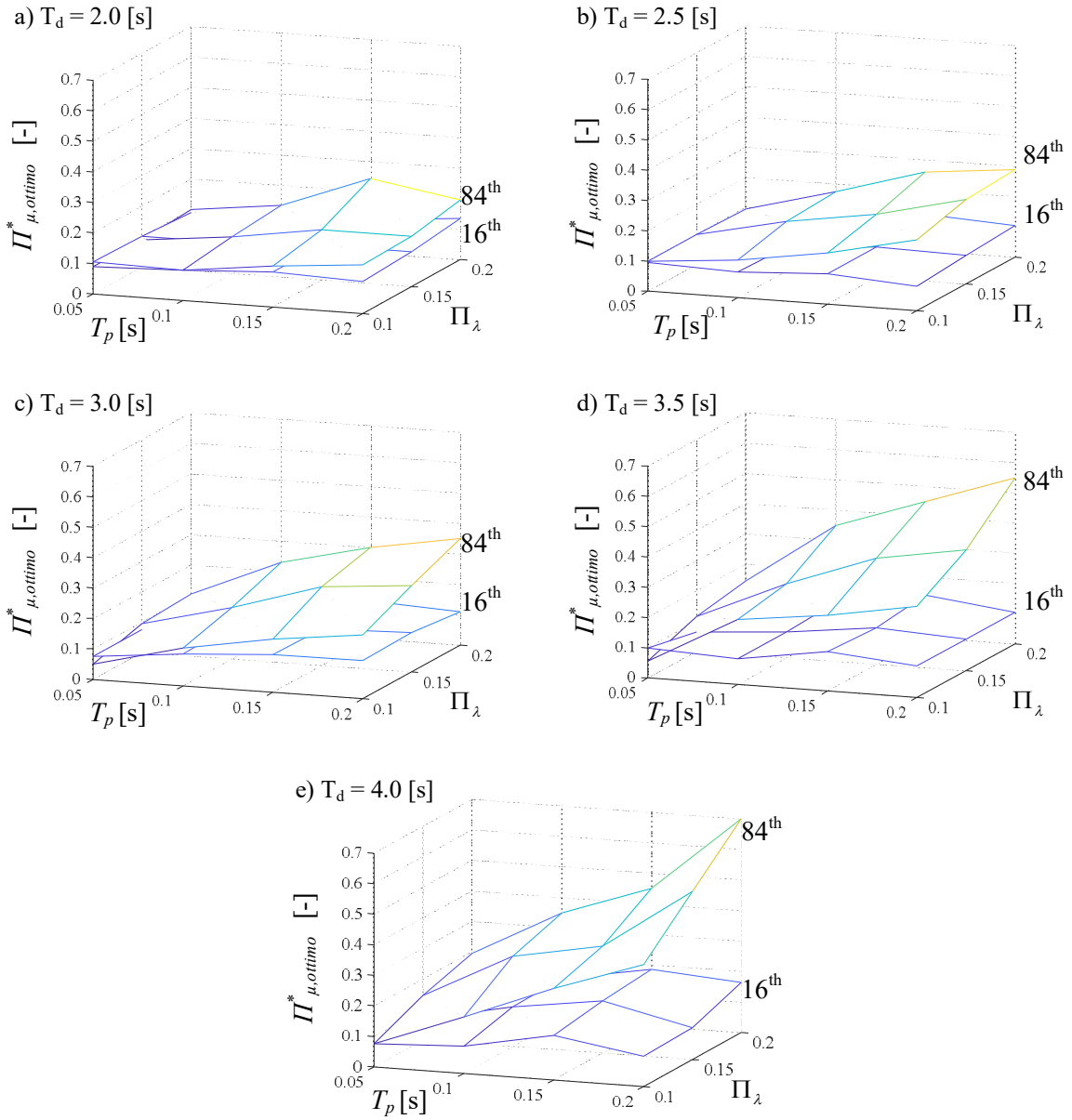
Figure 5.10 – Optimum values of normalized friction versus T_p and Π_λ with reference to the 16th and 84th percentiles of ψ_{u_p}

6

STRUCTURAL RESPONSE ANALYSIS

Bridges are key elements of transportation systems. Previous seismically induced damages to these structures, the significant cost of reconstruction and the need to bridges' immediate operation revealed the necessity of seismic vulnerability assessment of them according to performance based earthquake engineering philosophy. Such methodology requires accurate prediction of seismic capacity of the bridges and seismic demand associated to them. To achieve this goal, a newly born analysis method, called Incremental Dynamic Analysis (IDA), has been proposed by Vamvatsikos and Cornell (Vamvatsikos & Cornell , 2002).

In the current study, IDA is applied to reach the relationship between the seismic capacity and the demand of the structure and evaluate the structural performance accurately. IDA curves provide appropriate result formats which may be used to estimate the annual average frequency of exceeding predefined damage states and develop fragility curves of the bridges. Moreover, they may be integrated with hazard curves in order to evaluate the seismic reliability of the structure.

6.1 *INCREMENTAL DYNAMIC ANALYSIS*

Incremental Dynamic Analysis has emerged, over the last two decades, as an efficient and rigorous tool for seismic demand analysis, specifically in its probabilistic domain. It is a computational analysis method to perform a comprehensive assessment of the behaviour of structures under seismic loads, in order to estimate the seismic risk faced by a given structure. IDA involves performing multiple nonlinear dynamic analyses of a structural model under a suite of ground motion records, each scaled to several levels of seismic intensity. The scaling levels are appropriately selected to force the structure through the entire range of behaviour, from elastic to inelastic and finally to global dynamic instability, where the structure essentially experiences collapse. Initially, the method was called *Dynamic Pushover* and it was conceived as a way to estimate a path for the global collapse of the structure, but it was later recognized that such a technique would also enable checking for multiple limit states: not only for Life Safety, as is the standard for most seismic design methods, but also for lower and higher levels of intensity that represent different threat levels, such as Fully Operational and Near Collapse limit states.

The results are represented by the IDA curves, in terms of seismic intensity, typically denoted by a scalar *Intensity Measure* (*IM*), versus structural response, as measured by an *Engineering Demand Parameter* (*EDP*). Possible choices for the *IM* are scalar quantities related to the severity of the recorded ground motion and scaled linearly or nonlinearly with its amplitude; they may be the peak ground acceleration PGA or the peak ground velocity PGV, but the most widely used is the spectral acceleration. The *EDP* may be any structural response quantity that relates to structural, non-structural or contents' damage. Typical choices, for buildings, are the maximum inter-story drift, the individual peak story drifts and the peak floor accelerations.

In the present study it has been chosen as *IM* the spectral pseudo-acceleration $S_{pa}(T_d)$ at the isolated period of the system, while the maximum values of deck and pier displacements, $u_{d,max}$ and $u_{p,max}$ respectively, have been taken as *EDP*.

It is worth to note that, in general, the *IM* choice should be driven by criteria of efficiency, sufficiency and hazard computability: many studies demonstrated that the spectral pseudo-acceleration at the isolated period of the system is more efficient than the peak ground acceleration (Luco & Cornell, 2007) & (Pinto, Giannini, & Franchin, 2003); its use permits to reduce the response dispersion for the same number of ground motion considered and to obtain more confident response estimates for a given number of records employed.

The incremental dynamic analysis has been performed by scaling the thirty ground acceleration records presented in Table 4.2 (§ 4.3.1.2) to the *IM* levels related to the Life Safety spectrum of the site of L'Aquila (Abruzzo, Italy). These $\bar{S}_{pa}(T_d)$ values are shown in Table 6.1, while Figure 6.1 depicts the Life Safety (LS) and Near Collapse (NC) spectra. It is noteworthy that it has been also considered the Near Collapse limit state because the isolating system has to be verified with reference to it (Norme Tecniche per le Costruzioni, 2008). Hence, the range of variation of $S_{pa}(T_d)$ contemplated in the IDA implementation is between 0 and 3 m/s^2, i.e., the maximum $\bar{S}_{pa}(T_d)$ value at the Near Collapse limit state.

T_d [s]	$\bar{S}_{pa}(T_d)$ [g] at LS	$\bar{S}_{pa}(T_d)$ [g] at NC
2.0	0.2366	0.2973
2.5	0.1892	0.2378
3.0	0.1389	0.1940
3.5	0.1021	0.1425
4.0	0.0782	0.1091

Table 6.1 – Spectral pseudo-acceleration values related to the Life Safety and Near Collapse response spectra of L'Aquila
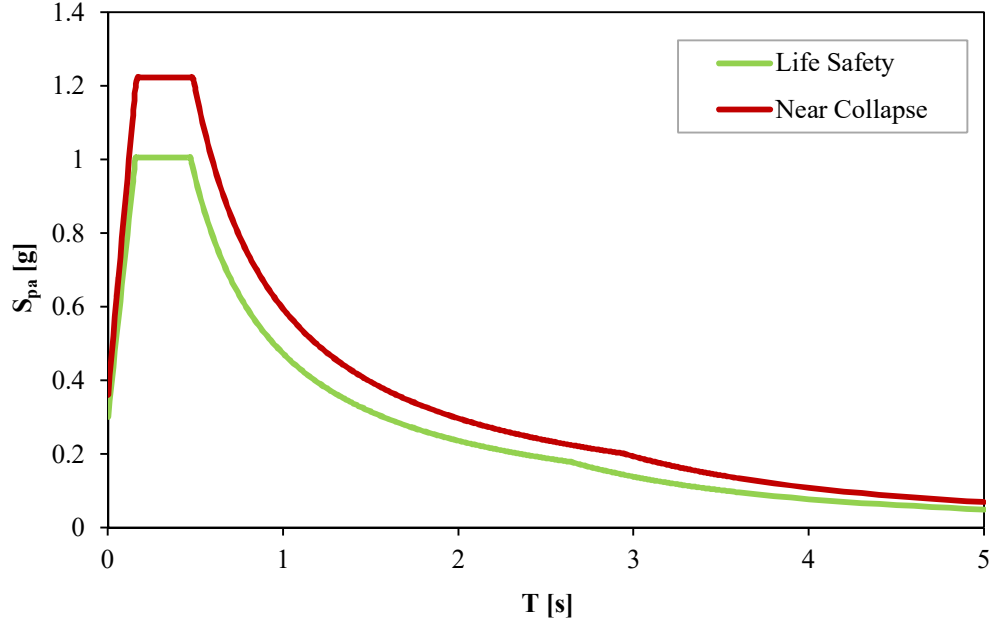
Figure 6.1 – Life Safety and Near Collapse response spectra of L'Aquila

From the $\Pi^*_{\mu,opt}$ values obtained after performing the parametric analysis presented in §5.4, the five values of the optimum friction coefficient at high velocities $f_{max,opt}$, corresponding to those of $\bar{S}_{pa}(T_d)$, have been defined, basing on Equation 5.1:

$$f_{max,opt} = \frac{\bar{S}_{pa}(T_d)}{g} \cdot \Pi^*_{\mu,opt} \tag{6.1}$$

Hence, the optimal $\Pi^*_{\mu,opt,AQ}$ parameters, referred to the site of L'Aquila, have been determined:

$$\Pi^*_{\mu,opt,AQ} = \frac{f_{max,opt} \cdot g}{S_{pa}(T_d)} \tag{6.2}$$

Subsequently, as for a selected *IM* level the IDA based values of *EDP* are modelled using a Lognormal distribution, the 50th, 16th and 84th percentiles of deck and pier displacements have been calculated at each *IM* level, following the procedure outlined in §4.3.1.3 (Equation 4.31) and basing on the geometric mean and dispersion dimensional values:

$$GM(u_{d,max}) = \frac{GM(\psi_{u_d}) \cdot S_{pa}(T_d)}{\omega_d^2} \tag{6.3}$$

$$GM(u_{p,max}) = \frac{GM(\psi_{u_p}) \cdot S_{pa}(T_d)}{\omega_d^2} \tag{6.4}$$

$$\beta(u_{d,max}) = \frac{\beta(\psi_{u_d}) \cdot S_{pa}(T_d)}{\omega_d^2} \qquad (6.5)$$

$$\beta(u_{p,max}) = \frac{\beta(\psi_{u_p}) \cdot S_{pa}(T_d)}{\omega_d^2} \qquad (6.6)$$

The $S_{pa}(T_d)$ versus $u_{d,max}$ and $u_{p,max}$ IDA plots, for fixed values of T_p and T_d and in function of the λ parameter, are shown in the following Figures 6.2 to 6.11.

In Figures 6.2 to 6.6 are plotted the results concerning the maximum deck displacement $u_{d,max}$. The dispersion is higher and the influence of the mass ratio λ is more marked for high T_d and medium-to-high T_p values, that is, in the cases of flexible system. Actually, the deck response decreases by increasing λ. The pier response dependence on the mass ratio (Figures 6.7 to 6.11) is evident even for low values of the periods and gradually reduces by increasing T_d. Furthermore, the dispersion, especially that related to the 84th percentile, is higher than in the case related to the deck.
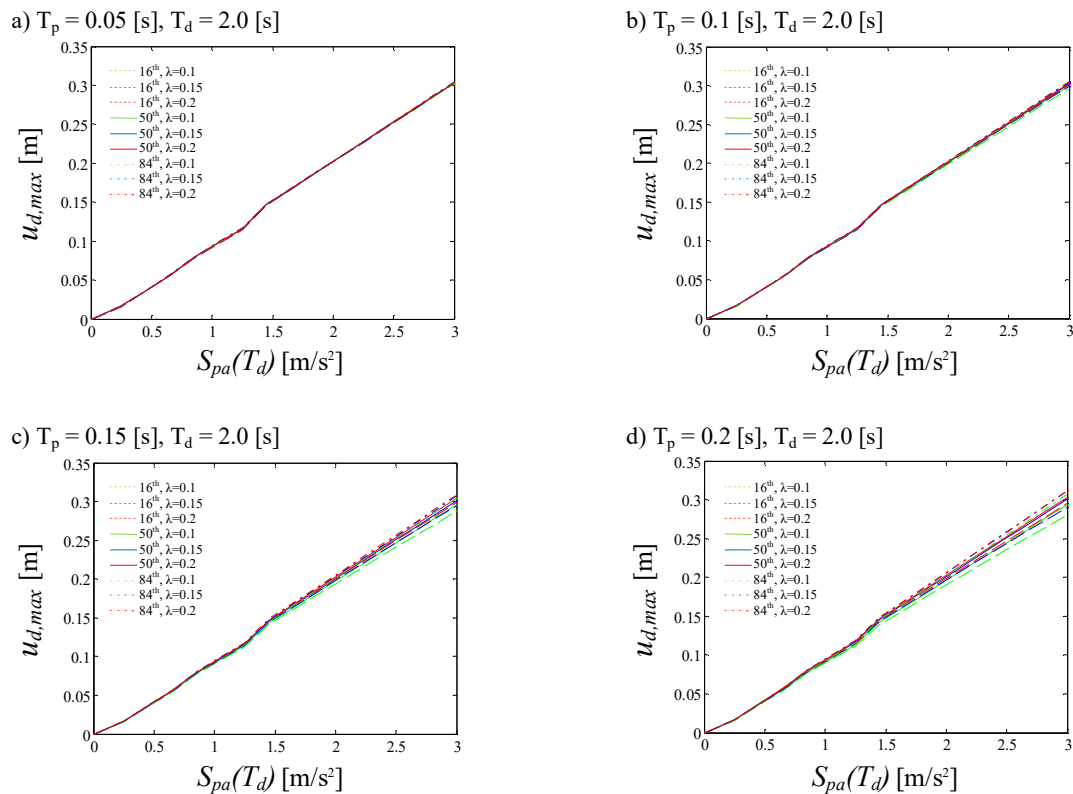
Figure 6.2 – IDA curves concerning the deck maximum displacements for fixed $T_d = 2s$ value and different T_p and λ values

a) $T_p = 0.05$ [s], $T_d = 2.5$ [s]

b) $T_p = 0.1$ [s], $T_d = 2.5$ [s]

c) $T_p = 0.15$ [s], $T_d = 2.5$ [s]

d) $T_p = 0.2$ [s], $T_d = 2.5$ [s]
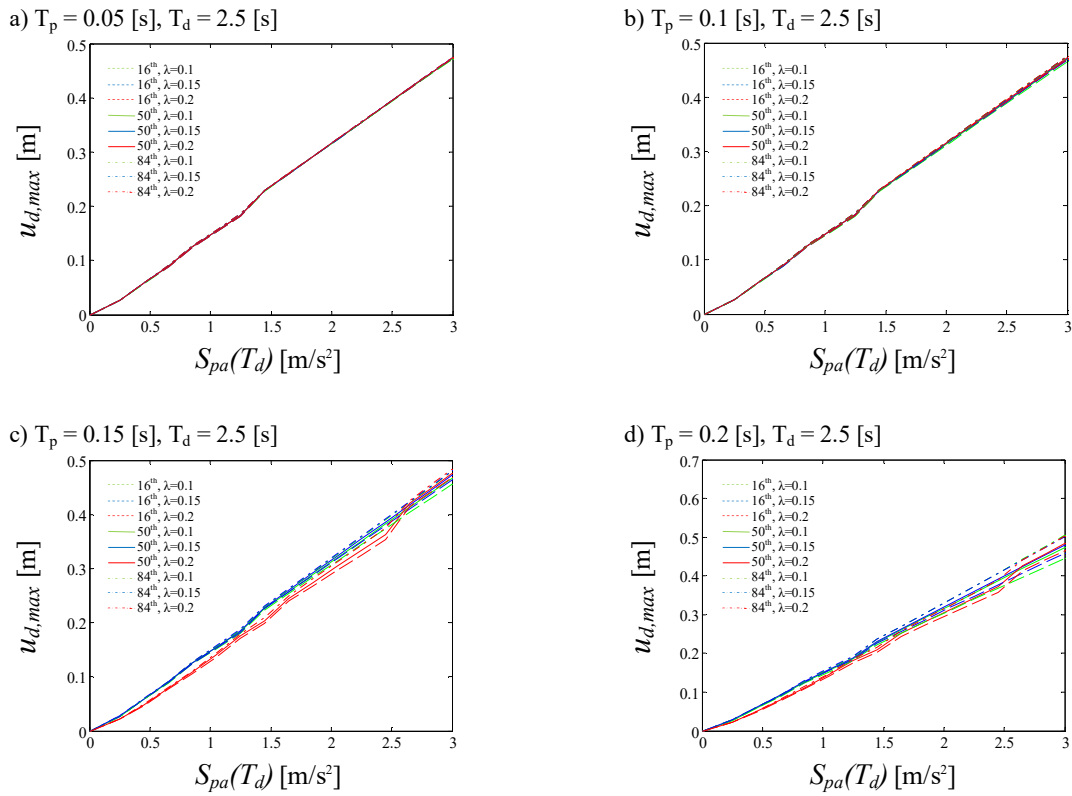
Figure 6.3 – IDA curves concerning the deck maximum displacements for fixed $T_d = 2.5s$ value and different T_p and λ values

a) $T_p = 0.05$ [s], $T_d = 3.0$ [s]

b) $T_p = 0.1$ [s], $T_d = 3.0$ [s]

c) $T_p = 0.15$ [s], $T_d = 3.0$ [s]

d) $T_p = 0.2$ [s], $T_d = 3.0$ [s]
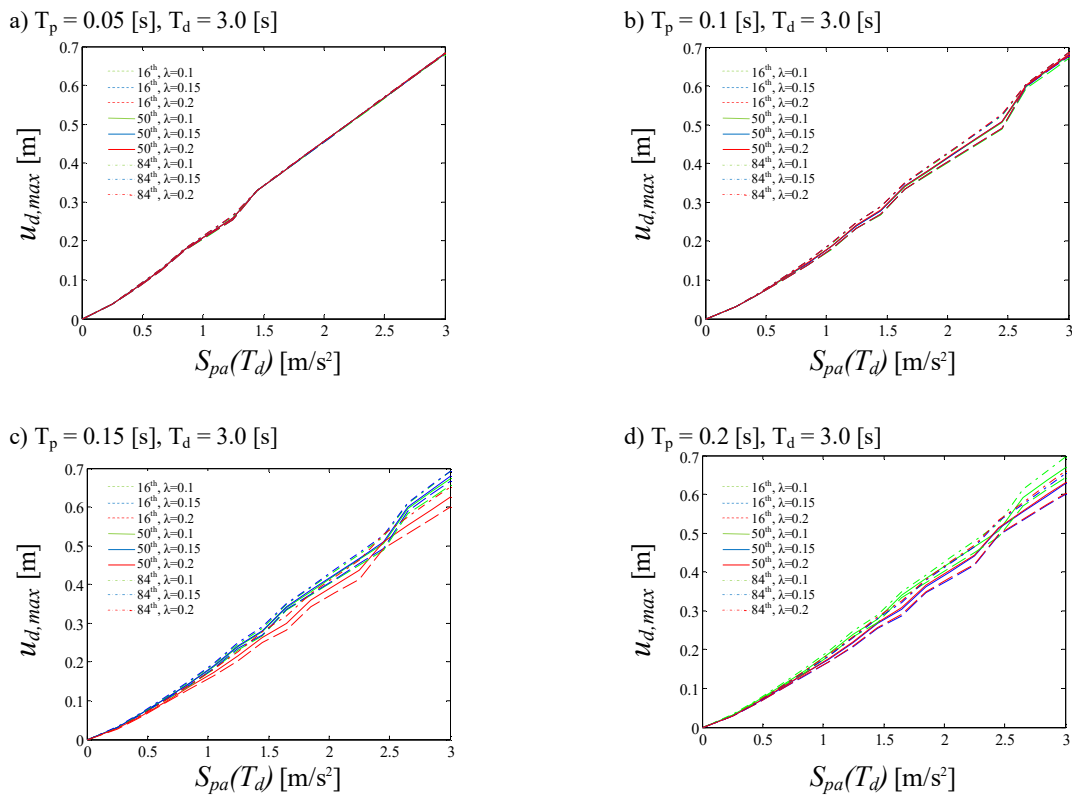
Figure 6.4 – IDA curves concerning the deck maximum displacements for fixed $T_d = 3s$ value and different T_p and λ values

a) T_p = 0.05 [s], T_d = 3.5 [s]

b) T_p = 0.1 [s], T_d = 3.5 [s]

c) T_p = 0.15 [s], T_d = 3.5 [s]

d) T_p = 0.2 [s], T_d = 3.5 [s]
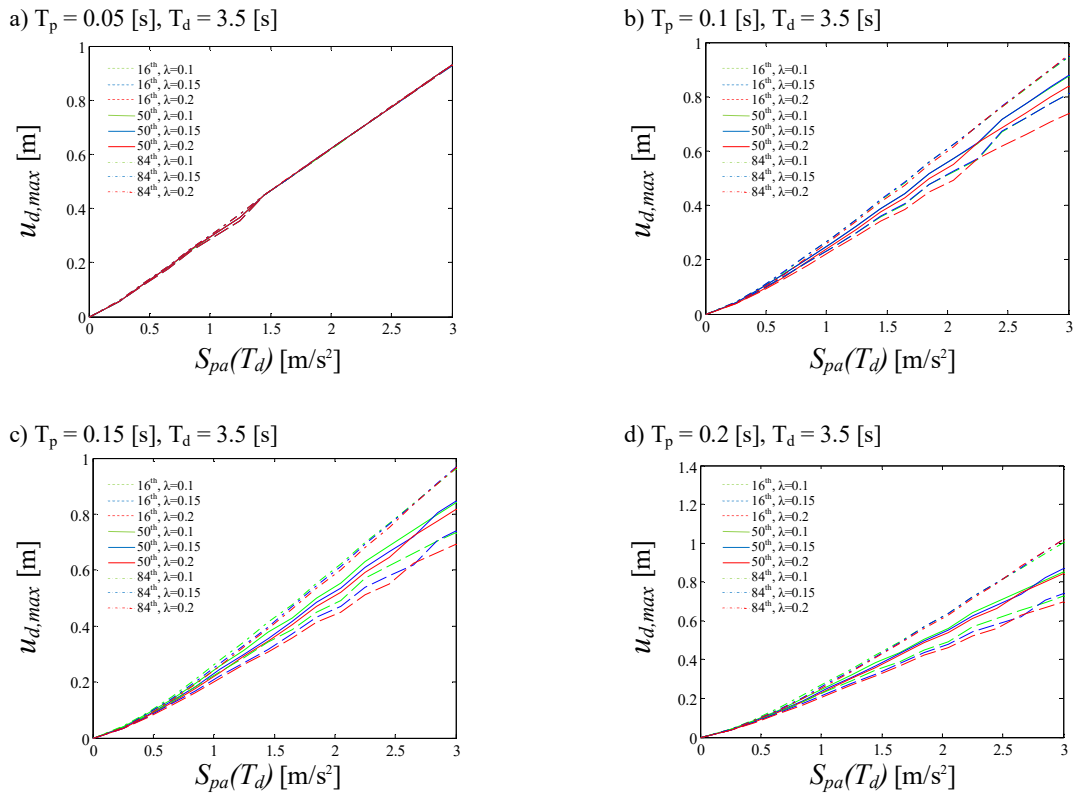
Figure 6.5 – IDA curves concerning the deck maximum displacements for fixed T_d = 3.5s value and different T_p and λ values

a) T_p = 0.05 [s], T_d = 4.0 [s]

b) T_p = 0.1 [s], T_d = 4.0 [s]

c) T_p = 0.15 [s], T_d = 4.0 [s]

d) T_p = 0.2 [s], T_d = 4.0 [s]
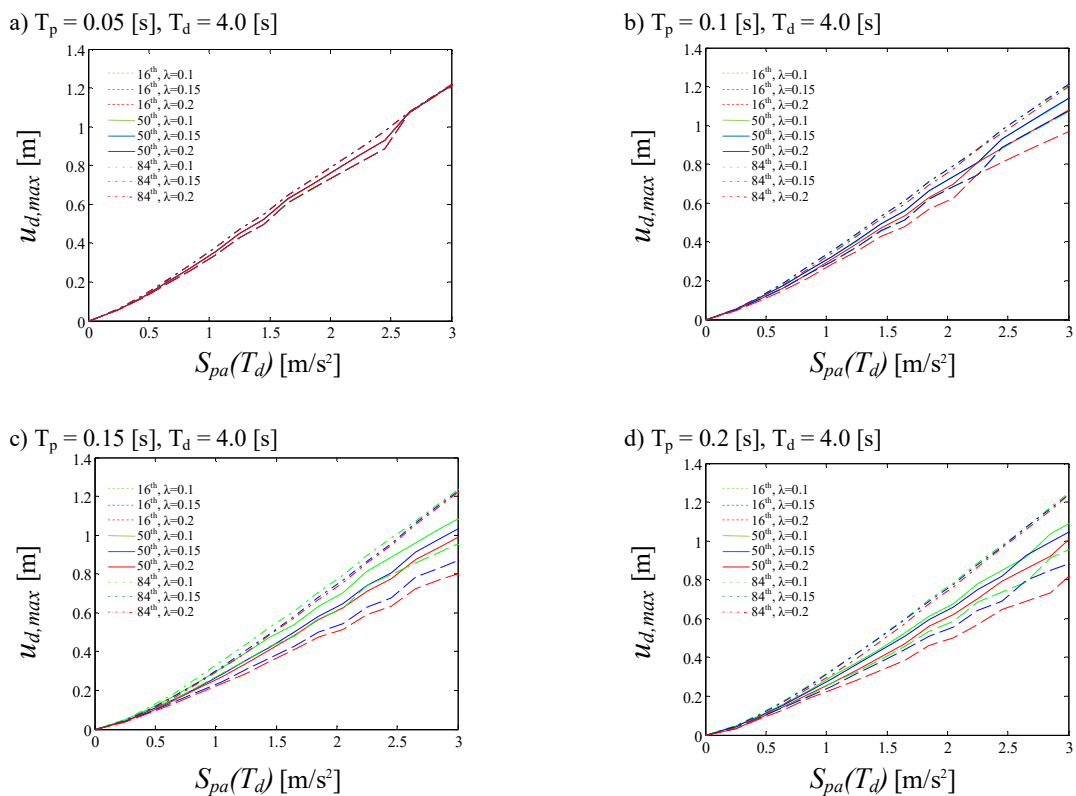
Figure 6.6 – IDA curves concerning the deck maximum displacements for fixed T_d = 4s value and different T_p and λ values

a) $T_p = 0.05$ [s], $T_d = 2.0$ [s]

b) $T_p = 0.1$ [s], $T_d = 2.0$ [s]

c) $T_p = 0.15$ [s], $T_d = 2.0$ [s]

d) $T_p = 0.2$ [s], $T_d = 2.0$ [s]
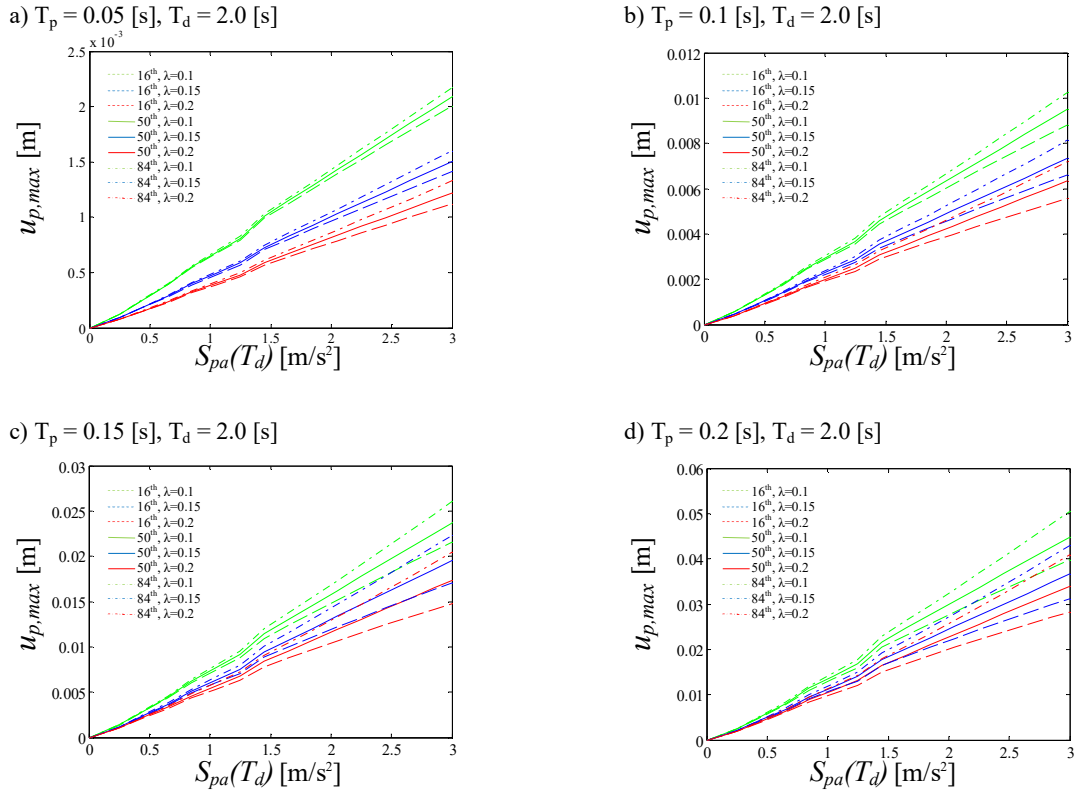
Figure 6.7 – IDA curves concerning the pier maximum displacements for fixed $T_d = 2s$ value and different T_p and λ values

a) $T_p = 0.05$ [s], $T_d = 2.5$ [s]

b) $T_p = 0.1$ [s], $T_d = 2.5$ [s]

c) $T_p = 0.15$ [s], $T_d = 2.5$ [s]

d) $T_p = 0.2$ [s], $T_d = 2.5$ [s]
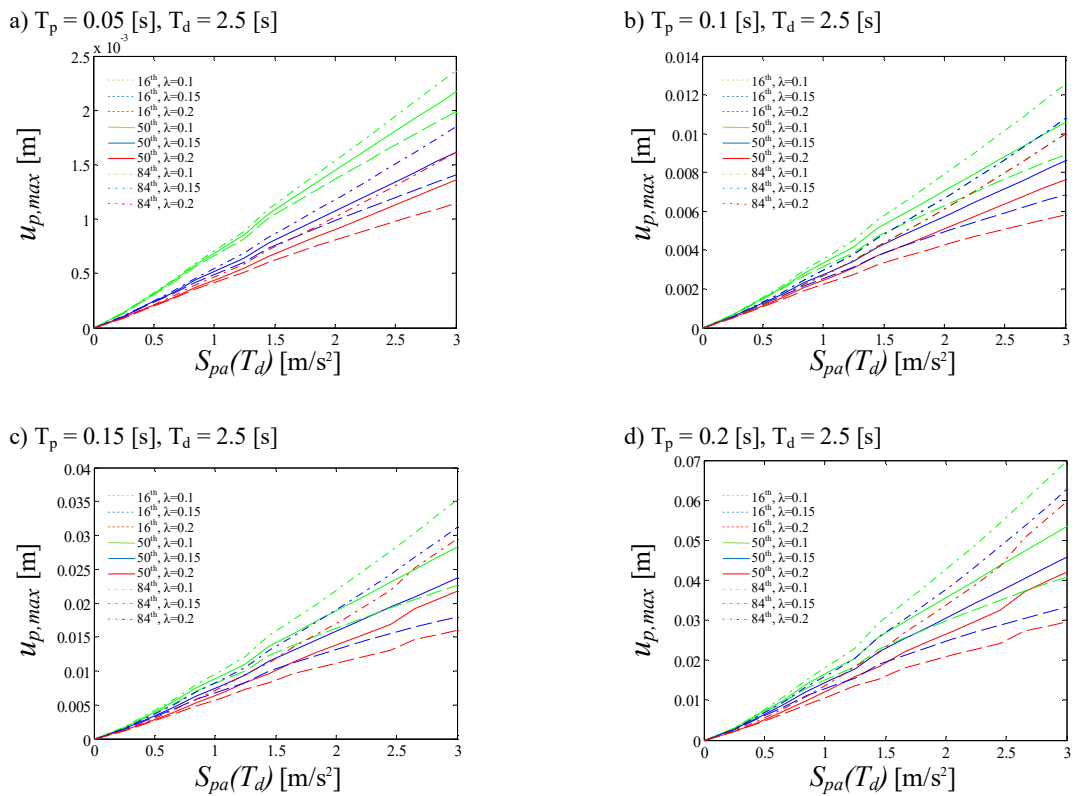
Figure 6.8 – IDA curves concerning the pier maximum displacements for fixed $T_d = 2.5s$ value and different T_p and λ values

a) T_p = 0.05 [s], T_d = 3.0 [s]

b) T_p = 0.1 [s], T_d = 3.0 [s]

c) T_p = 0.15 [s], T_d = 3.0 [s]

d) T_p = 0.2 [s], T_d = 3.0 [s]
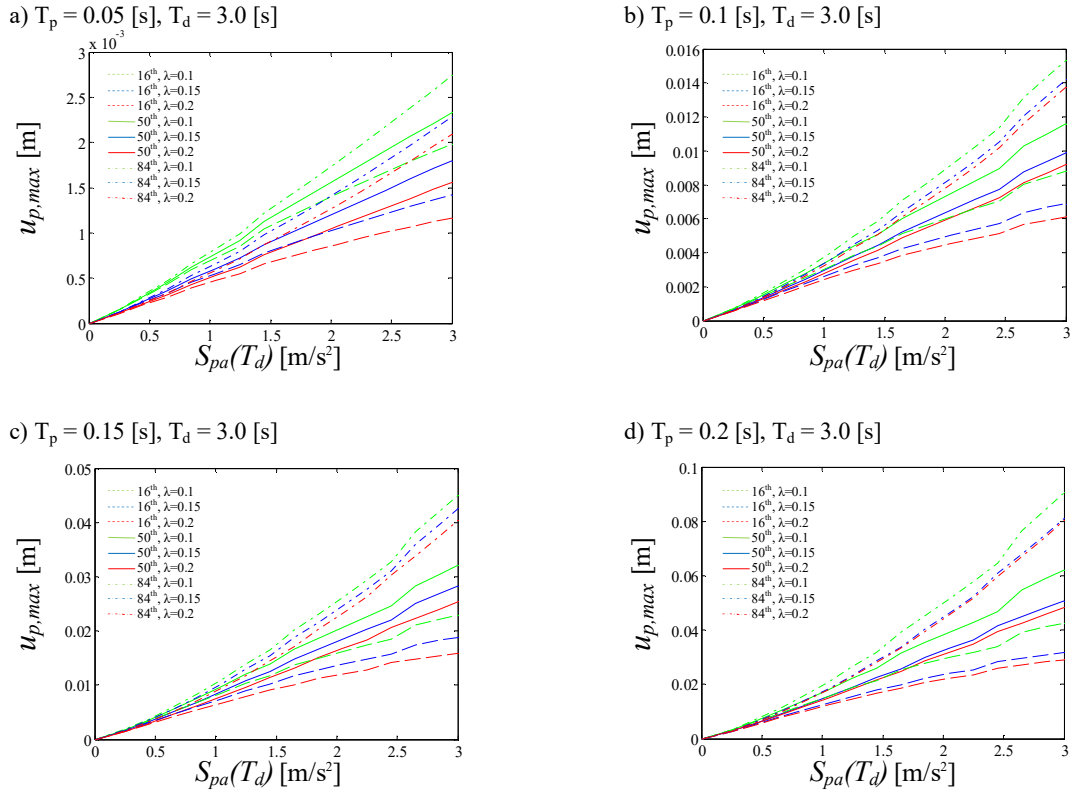
Figure 6.9 – IDA curves concerning the pier maximum displacements for fixed $T_d = 3s$ value and different T_p and λ values

a) T_p = 0.05 [s], T_d = 3.5 [s]

b) T_p = 0.1 [s], T_d = 3.5 [s]

c) T_p = 0.15 [s], T_d = 3.5 [s]

d) T_p = 0.2 [s], T_d = 3.5 [s]
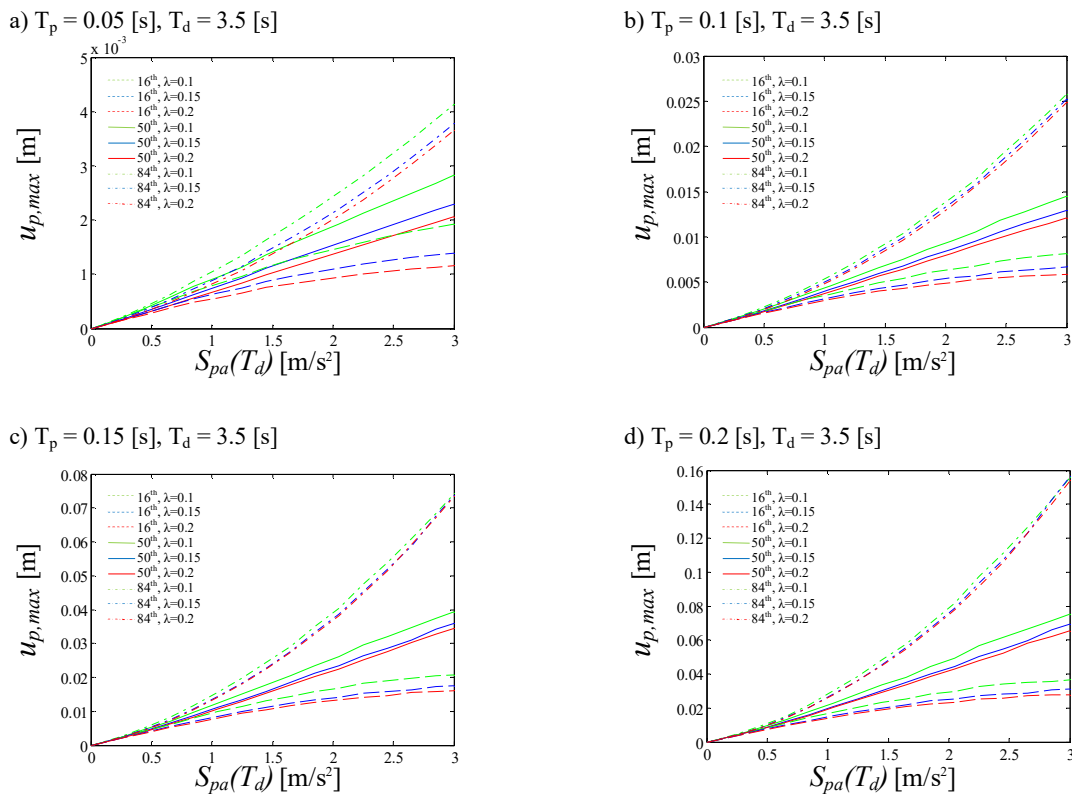
Figure 6.10 – IDA curves concerning the pier maximum displacements for fixed $T_d = 3.5s$ value and different T_p and λ values

a) $T_p = 0.05$ [s], $T_d = 4.0$ [s]

b) $T_p = 0.1$ [s], $T_d = 4.0$ [s]

c) $T_p = 0.15$ [s], $T_d = 4.0$ [s]

d) $T_p = 0.2$ [s], $T_d = 4.0$ [s]
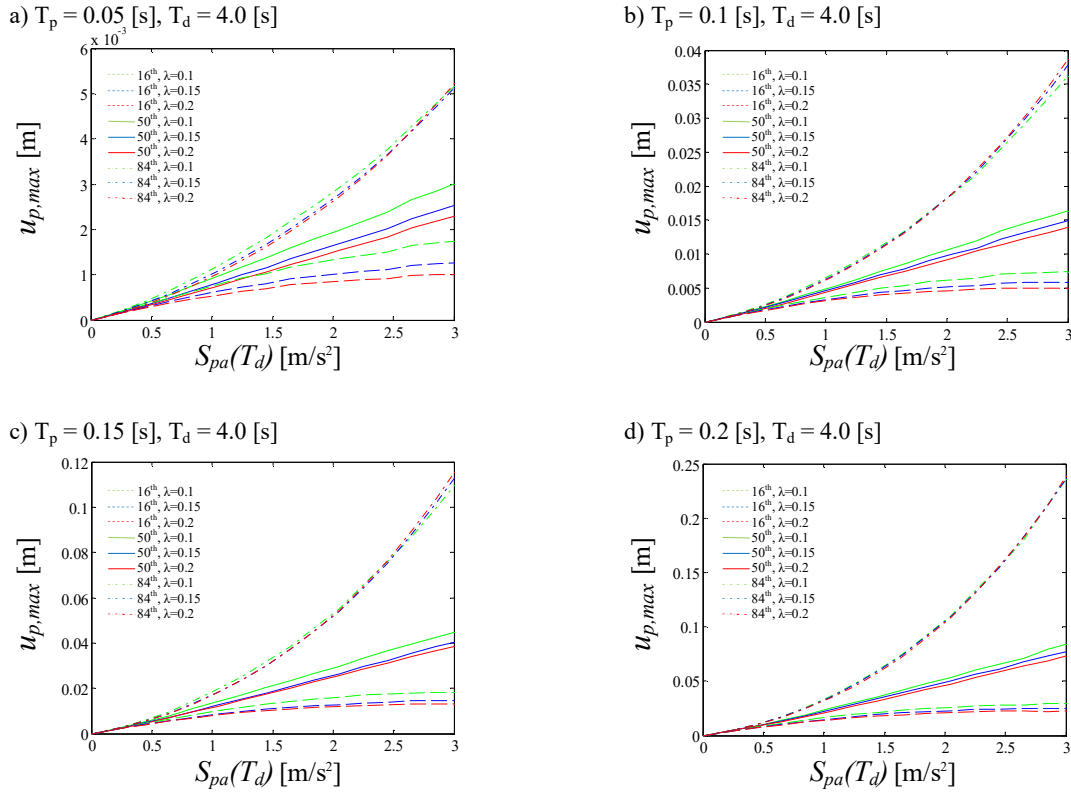
Figure 6.11 – IDA curves concerning the pier maximum displacements for fixed $T_d = 4s$ value and different T_p and λ values

6.2 *FRAGILITY ANALYSIS*

An incremental dynamic analysis involves *IM* vs *EDP* curves for a suit of acceleration records, which is commonly used in probabilistic seismic demand analysis (PSDA). The IDA based PSDA may be easily incorporated into seismic fragility analysis of structures.

The seismic fragility of a structure is defined as its conditional probability of failure, given a specific intensity of the seismic action. The probability of failure may be calculated for any limit state, since the latter is typically described as the performance level defined for a specific response quantity or *Damage Measure* (*DM*), while the seismic intensity level is described by an intensity measure. This way, the fragility of a structure may be defined as:

$$F_r = P(DM \geq DM_l | IM) \qquad (6.7)$$

in which DM_l is the threshold response quantity.

In this study, the column drift index CDI (§1.1) has been defined as DM parameter for the pier, with reference to the Fully Operational, Operational, Life Safety and Near Collapse limit states (Table 6.2): they have been considered the column drift index reduced values CDI_{is} for isolated bridges, i.e., $CDI_{is} = \frac{1}{3}CDI$ (FEMA 274, 1997). Referring to the isolating system, instead, they have been delineated nine limit states in terms of in-plan radius r design values, varying in the range between 0.10 m and 0.50 m (Table 6.3).

The pier in the bridge model has been considered to be of uniform circular cross section throughout the height. The latter has been determined from the fundamental time period of the pier T_p with top free condition, since it may be expressed as (Jangid R. , 2008):

$$T_p = \sqrt{\frac{\overline{m}_p h^4}{EI}} \cdot \frac{2\pi}{(1.875)^2} \tag{6.8}$$

where $\overline{m}_p$ is the mass per unit length, h is the height and EI is the flexural rigidity of the pier. Equation 6.8 is based on the fundamental time period of a uniform cantilever beam under transverse vibrations. The mechanical and geometrical characteristics of the column are represented in Table 6.4.

Limit state	Column drift index CDI	Column drift index CDI_{is}
Fully Operational	0.7 %	0.23 %
Operational	1.5 %	0.5 %
Life Safety	2.5 %	0.83 %
Near Collapse	5 %	1.67 %

Table 6.2 – Column drift index values for isolated bridges, related to the different limit states

Limit state	1	2	3	4	5	6	7	8	9
r [m]	0.10	0.15	0.20	0.25	0.30	0.35	0.40	0.45	0.50

Table 6.3 – In-plan radius values of FPS related to the different limit states

Bridge Column characteristics	
Concrete Strength Class	C30/37
Young Modulus	$E = 32837$ MPa
Specific weight	$\gamma = 25$ kN/m^3
Cross section diameter	$d = 140$ cm
Mass per unit length	$\overline{m}_p = 3923$ kg/m
Moment of inertia	$I = 1.89 \cdot 10^7$ cm^4

Table 6.4 – Mechanical and geometrical characteristics of pier

As the IDA curves have been derived, in correspondence of each *IM* level they identify the probability density function (PDF) of the *EDP*. From this latter, the probability of failure may be calculated, according to Equation 6.7, at each *IM* level as the area subtended by the PDF starting from the DM_l value corresponding to the limit state in consideration. In a *IM* vs F_r graph, these results are represented by point values. However, it is advantageous to express the fragility as a continuous function of the intensity measure, in order to obtain the so-called fragility curves. These have been developed, for each limit state, using a Lognormal model. After determining the normal standard variable u_r related to the *i*th point of the fragility curve, the latter is defined by means of a linear regression on Lognormal plane ($\ln IM$ vs u_r). This way, the parameters of the probability law may be defined, as the regression equation is:

$$u_r = a \cdot \ln IM + b \qquad (6.10)$$

In fact, the Lognormal distribution of a variable x is equivalent to a Gaussian distribution of variable $y = \ln x$, characterized by the parameters μ_y and σ_y (mean and standard deviation, respectively). Therefore, by setting:

$$u_r = \frac{y - \mu_y}{\sigma_y} \qquad (6.11)$$

they may be derived:

$$\mu_y = -\frac{b}{a} \qquad \sigma_y = \frac{1}{a} \qquad (6.12)$$

Finally, the probability of failure may be calculated as a function of the *IM* level, for a selected limit state defined by DM_l:

$$F_r = 1 - \Phi\left[\frac{\ln\left(\mu_y | DM_l\right)}{\sigma_y}\right] \qquad (6.9)$$

where Φ is the standard normal CDF (cumulative distribution function) operator.

The following Figures 6.12 to 6.19 show the fragility curves, plotted in a non-logarithmic scale and referred both to the isolating system and the substructure, for each limit state and for the bridge dynamic characteristics that most affect the seismic vulnerability.

a) $T_p = 0.05$ [s], $T_d = 2.0$ [s]

b) $T_p = 0.1$ [s], $T_d = 2.0$ [s]

c) $T_p = 0.15$ [s], $T_d = 2.0$ [s]

d) $T_p = 0.2$ [s], $T_d = 2.0$ [s]
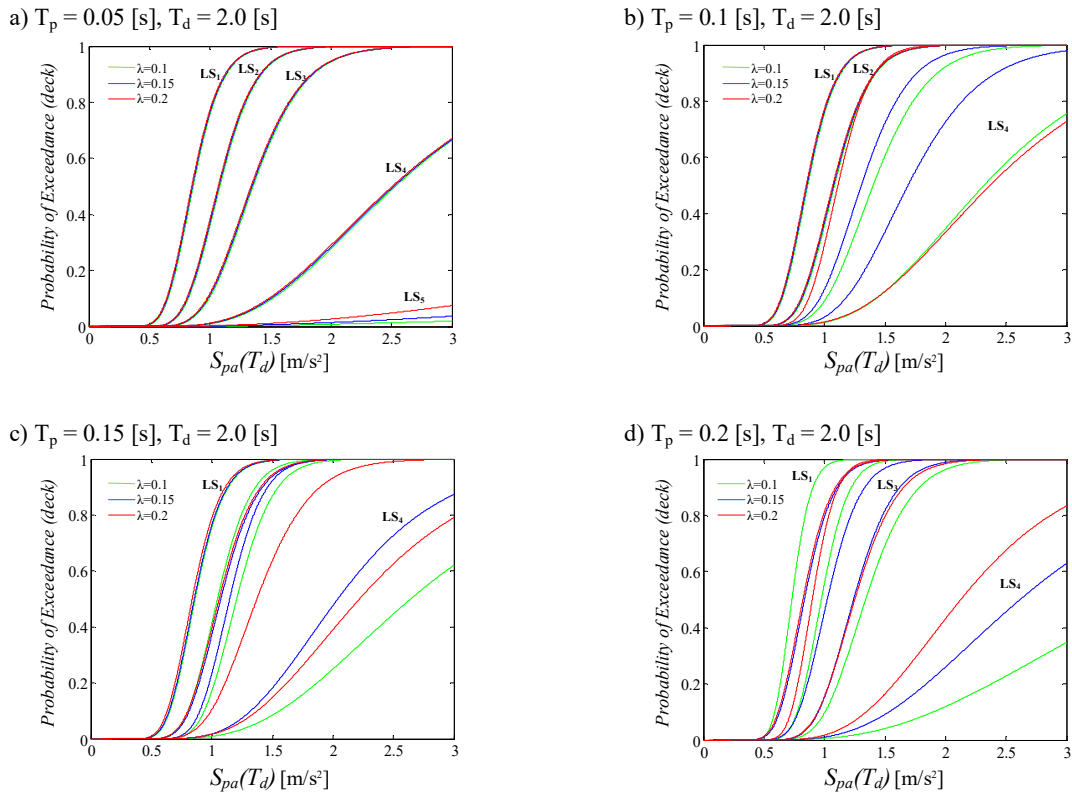
Figure 6.12 – Fragility curves referred to the isolating system for each limit state LS_i and for fixed $T_d = 2s$ value and different T_p and λ values

a) $T_p = 0.05$ [s], $T_d = 2.5$ [s]

b) $T_p = 0.1$ [s], $T_d = 2.5$ [s]

c) $T_p = 0.15$ [s], $T_d = 2.5$ [s]

d) $T_p = 0.2$ [s], $T_d = 2.5$ [s]
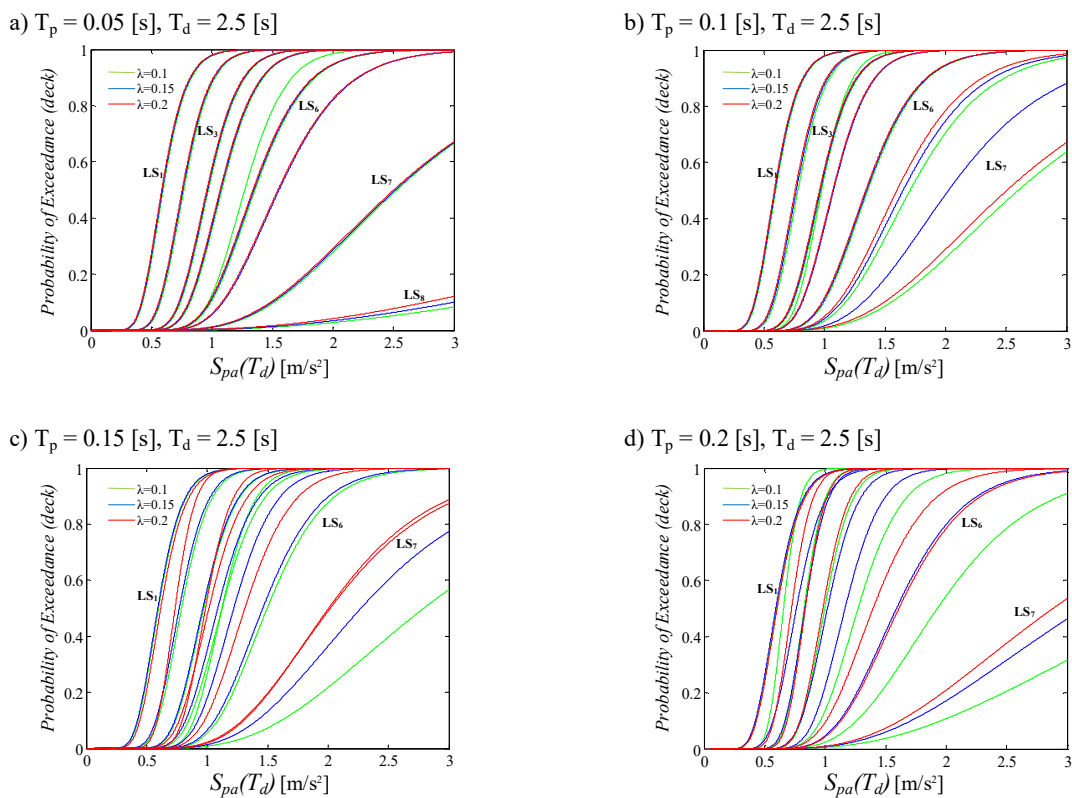
Figure 6.13 – Fragility curves referred to the isolating system for each limit state LS_i and for fixed $T_d = 2.5s$ value and different T_p and λ values

a) $T_p = 0.05$ [s], $T_d = 3.0$ [s]

b) $T_p = 0.1$ [s], $T_d = 3.0$ [s]

c) $T_p = 0.15$ [s], $T_d = 3.0$ [s]

d) $T_p = 0.2$ [s], $T_d = 3.0$ [s]
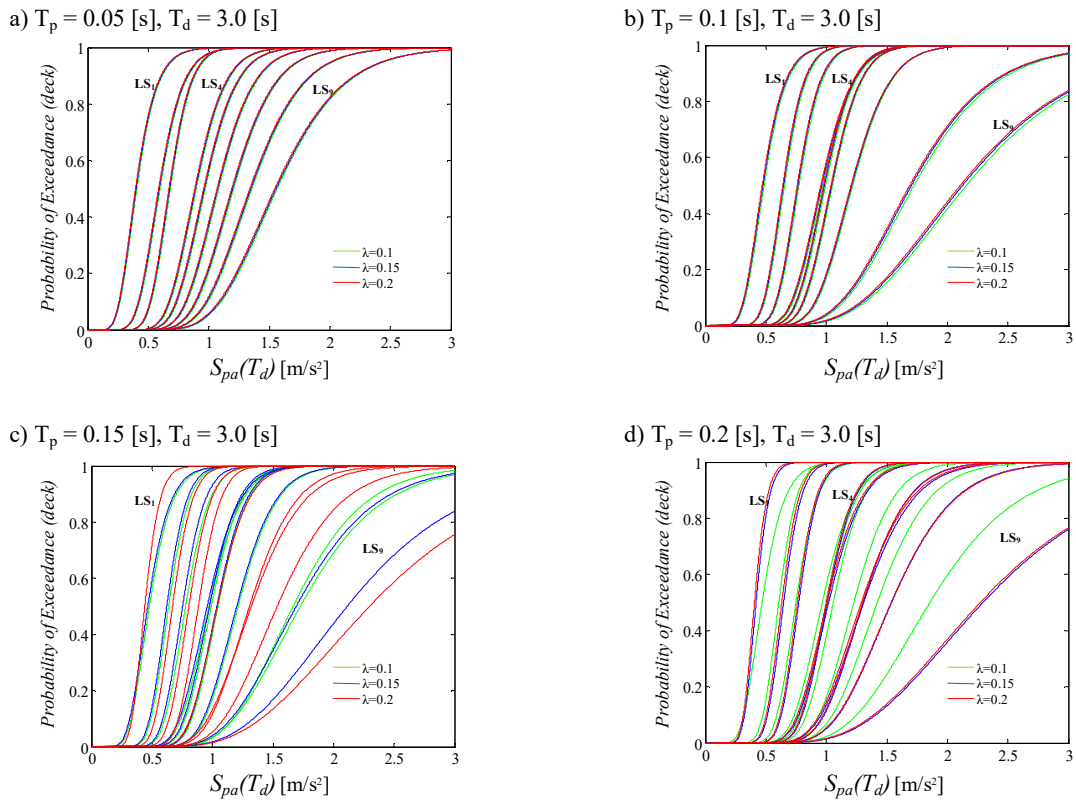
Figure 6.14 – Fragility curves referred to the isolating system for each limit state LS_i and for fixed $T_d = 3s$ value and different T_p and λ values

a) $T_p = 0.05$ [s], $T_d = 3.5$ [s]

b) $T_p = 0.1$ [s], $T_d = 3.5$ [s]

c) $T_p = 0.15$ [s], $T_d = 3.5$ [s]

d) $T_p = 0.2$ [s], $T_d = 3.5$ [s]
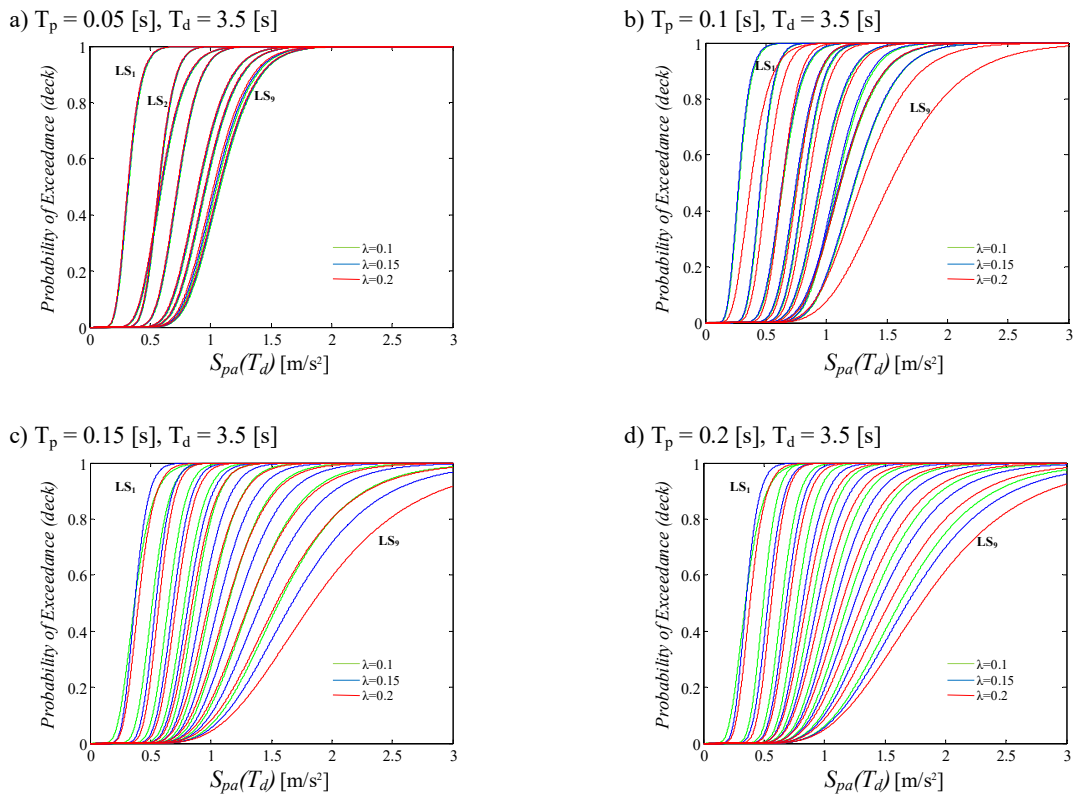
Figure 6.15 – Fragility curves referred to the isolating system for each limit state LS_i and for fixed $T_d = 3.5s$ value and different T_p and λ values

a) T_p = 0.05 [s], T_d = 4.0 [s]

b) T_p = 0.1 [s], T_d = 4.0 [s]

c) T_p = 0.15 [s], T_d = 4.0 [s]

d) T_p = 0.2 [s], T_d = 4.0 [s]
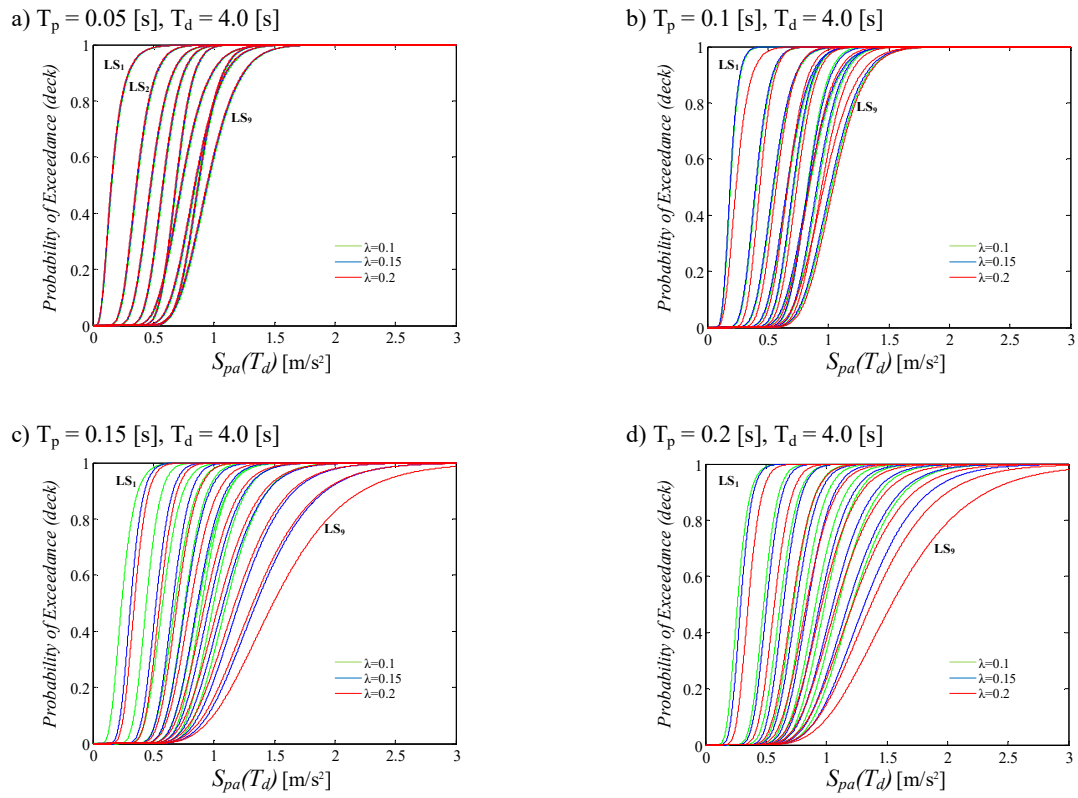
Figure 6.16 – Fragility curves referred to the isolating system for each limit state LS_i and for fixed $T_d = 4s$ value and different T_p and λ values

a) $T_p = 0.1$ [s], $T_d = 3.0$ [s]

b) $T_p = 0.1$ [s], $T_d = 3.5$ [s]

c) $T_p = 0.1$ [s], $T_d = 4.0$ [s]
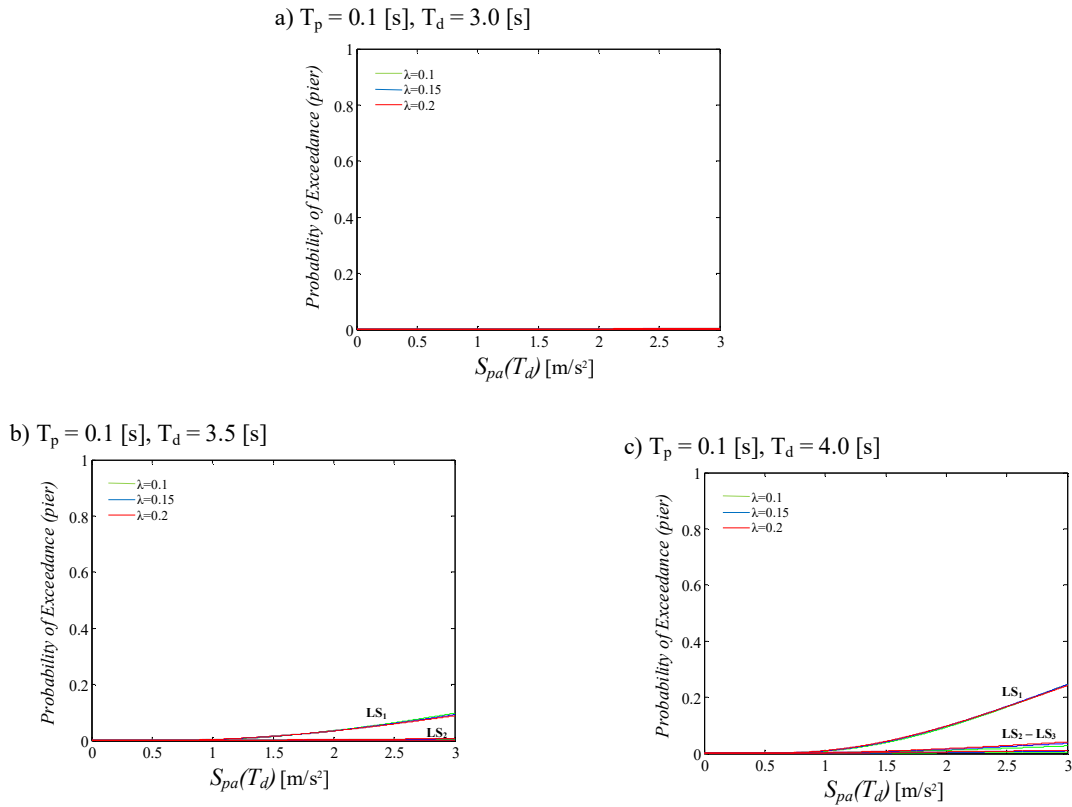
Figure 6.17 – Fragility curves referred to the substructure for each limit state LS_i and for fixed $T_p = 0.1s$ value and different T_d and λ values

a) $T_p = 0.15$ [s], $T_d = 2.5$ [s]

b) $T_p = 0.15$ [s], $T_d = 3.0$ [s]

c) $T_p = 0.15$ [s], $T_d = 3.5$ [s]

d) $T_p = 0.15$ [s], $T_d = 4.0$ [s]
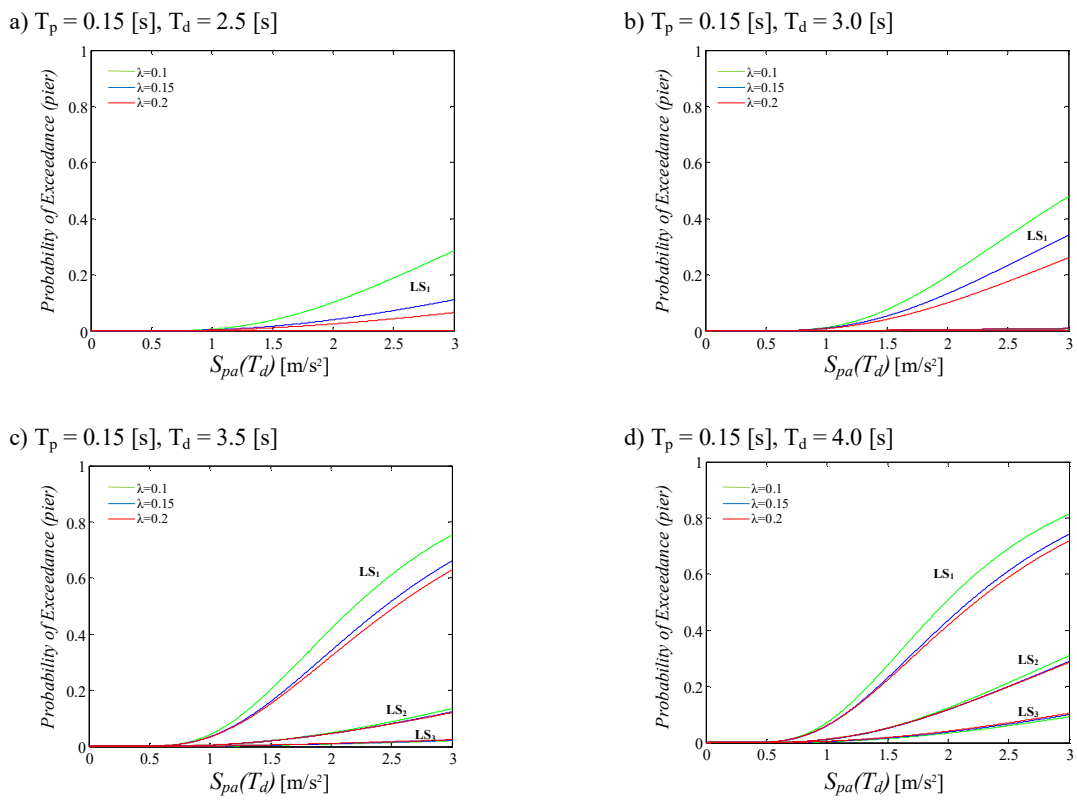
Figure 6.18 – Fragility curves referred to the substructure for each limit state LS_i and for fixed $T_p = 0.15s$ value and different T_d and λ values

a) T_p = 0.2 [s], T_d = 2.0 [s]

b) T_p = 0.2 [s], T_d = 2.5 [s]

c) T_p = 0.2 [s], T_d = 3.0 [s]

d) T_p = 0.2 [s], T_d = 3.5 [s]

e) T_p = 0.2 [s], T_d = 4.0 [s]
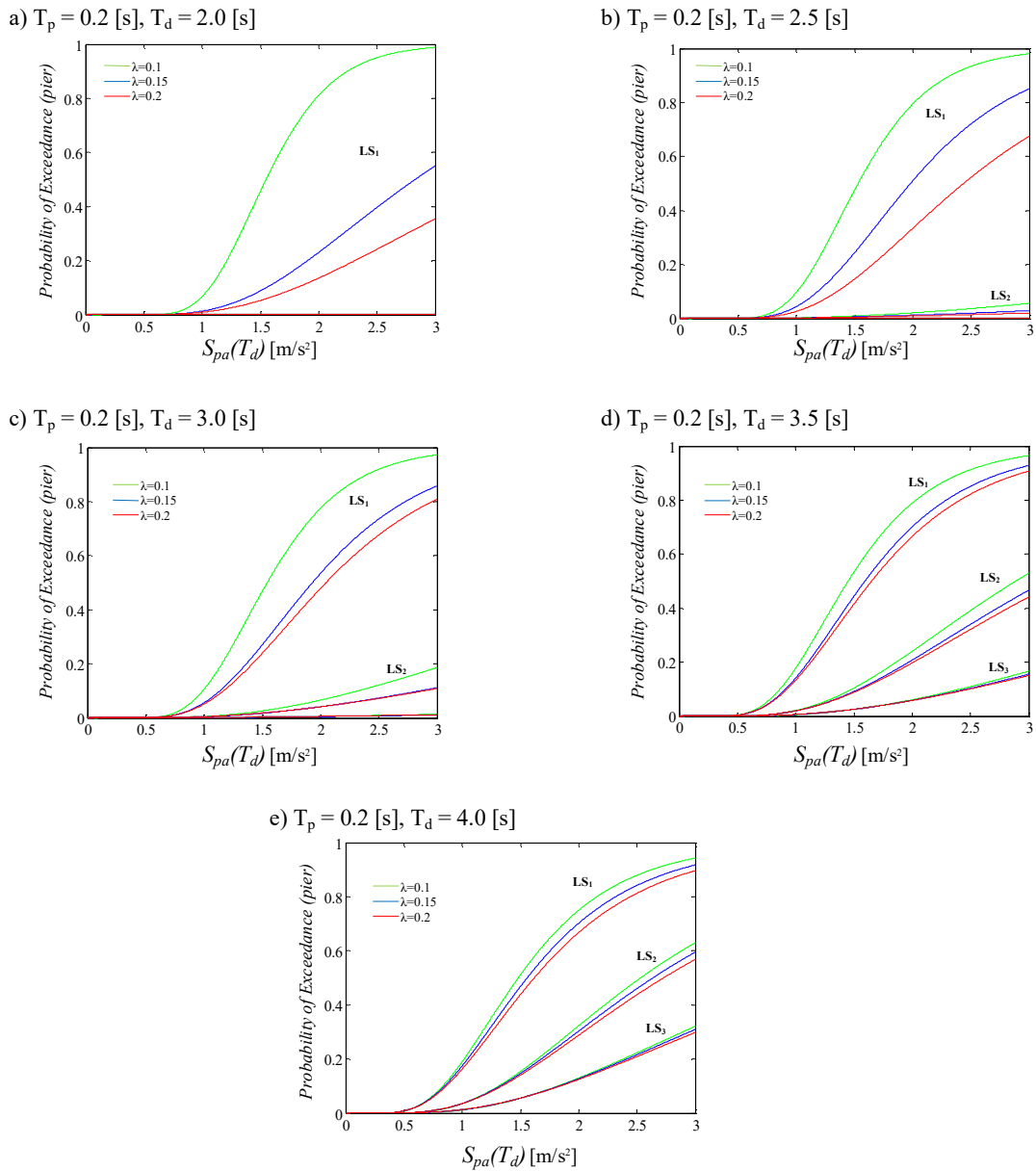
Figure 6.19 – Fragility curves referred to the substructure for each limit state LS_i and for fixed $T_p = 0.2s$ value and different T_d and λ values

In Figure 6.12 only the first four limit states LS_i have been considered as the fragility curves related to the fifth-to-ninth limit states assumed almost nil values, since they are referred to the lowest value of the isolated bridge period T_d. By increasing T_d (Figures 6.13 to 6.16), the system fragility gradually increases, as consequence of a higher displacement demand, typical of flexible structures. This phenomenon is very positive, as it demonstrates the efficiency of the isolating system, whose aim is uncoupling the superstructure from the substructure, so that nearly all of the displacement occurs over the height of the isolators. Additionally, the more the whole system is flexible, that is for increasing T_p and T_d values, the more the influence of the mass ratio is evident (Figures 6.13 to 6.15 – c-d).

Figures 6.17 to 6.19 show the results concerning the pier fragility: the cases related to the lowest T_p value have not been contemplated because they imply negligible exceedance probabilities, due to the high rigidity characterizing the structure. Actually, also in this case it may be said that the more the whole system is flexible, the more it is fragile, but the high fragility values, i.e., those attaining the unit, are reached for $S_{pa}(T_d)$ values much higher than the case of the isolator and only for the first limit state (Fully Operational). By increasing T_p, the mass ratio effect is evident, especially for the first limit sate. Clearly, for the lowest λ value (0.1), the pier is more fragile. Finally, it is noteworthy that the Near Collapse limit state has not been represented because, as expected, its probability of exceedance assumed almost nil values, since the verification of bridge piers has to be referred to the Life Safety limit state (Norme Tecniche per le Costruzioni, 2008).

In conclusion, it may be stated that the isolation system is efficient, as the pier fragility values resulted very low and almost all the displacements are concentrated at the isolating level.

6.3 RELIABILITY ANALYSIS

6.3.1 Evaluation of the local seismic hazard

The seismic hazard curve $\lambda_S(s)$ of a specific site identifies the annual average frequency of exceeding the s value by a parameter, which is representative of the local earthquake intensity S. This parameter is usually expressed in terms of spectral ordinate at the structure's fundamental period, i.e., in this study, the spectral pseudo-acceleration $S_{pa}(T_d)$.

The referring site is L'Aquila (Abruzzo, Italy): the following Table 6.5 shows its peak ground acceleration values at 50th, 16th and 84th percentiles, in function of the nine return periods considered by INGV – *Istituto Nazionale di Geofisica e Vulcanologia* (Meletti & Montaldo, 2007). Actually, the *DPC-INGV-S1 Project* by INGV provides nine PGA values to be associated to specific probability P_{VR} and annual average frequency λ_S of exceedance and, consequently, to an earthquake characterized by a specific return period T_R. In fact, the average frequency and the return period are correlated by the relationship:

$$\lambda_S(s_i) = \frac{1}{T_{R,i}} \qquad s_i = S(T_{R,i}) \qquad i = 1, \dots, 9 \qquad (6.13)$$

L'Aquila (ID=26306, lon:13°42'25'', lat:42°38'49'')					
P_{VR} in 50 years	T_R [yrs]	λ_S [yrs^{-1}]	PGA [g] (50th percentile)	PGA [g] (84th percentile)	PGA [g] (16th percentile)
2%	2475	0.0004	0.4522	0.5227	0.4098
5%	975	0.0010	0.3341	0.3674	0.3031
10%	475	0.0021	0.2608	0.2844	0.2378
22%	201	0.0050	0.1906	0.2038	0.1736
30%	140	0.0071	0.1640	0.1754	0.1510
39%	101	0.0099	0.1424	0.1535	0.1309
50%	72	0.0139	0.1226	0.1318	0.1111
63%	50	0.0199	0.1041	0.1115	0.0919
81%	30	0.0332	0.0789	0.0871	0.0680

Table 6.5 – L'Aquila: PGA values at 50th, 16th and 84th percentiles, in function of the nine return periods considered by INGV

From the nine median (50th percentile) PGA values provided by INGV, they have been determined the spectral pseudo-accelerations, evaluated at the nine return periods T_R and with reference to the five fundamental periods T_d of the isolated bridge. Based on these values, they have been defined the site's median hazard curves $\lambda_S(s)$. It is noteworthy that for the calculation of λ_{LS} (annual average frequency of exceeding the ith limit state), it should be used the mean hazard curve $\bar{\lambda}_S$, which is obtained by multiplying the median curve λ_S by an amplification factor β_H:

$$\bar{\lambda}_S(s) = \lambda_S(s) \cdot e^{0.5\beta_H^2} \tag{6.14}$$

$$\beta_H = \frac{\ln(S_{d,84th}) - \ln(S_{d,16th})}{2} \tag{6.15}$$

The amplification factor β_H is a parameter that allows estimating the epistemic uncertainty of the hazard, while $S_{d,84th}$ and $S_{d,16th}$ represent the spectral displacements evaluated considering, respectively, the PGA 84th percentile and 16th percentile values, in accordance to the relationship between the spectral pseudo-acceleration and displacement:

$$S_d(T_d) = \frac{S_{pa}(T_d)}{\omega_d^2} \tag{6.16}$$

The mean hazard curve $\bar{\lambda}_S(s)$ may be efficiently approximated by a quadratic logarithmic function:

$$\ln\left(\bar{\lambda}_S(\ln S)\right) = k_2 \ln S^2 + k_1 \ln S + k_0 \qquad (6.17)$$

which hence leads to:

$$\bar{\lambda}_S(s) = e^{k_0} \cdot e^{k_1 \ln S + k_2 \ln S^2} \qquad (6.18)$$
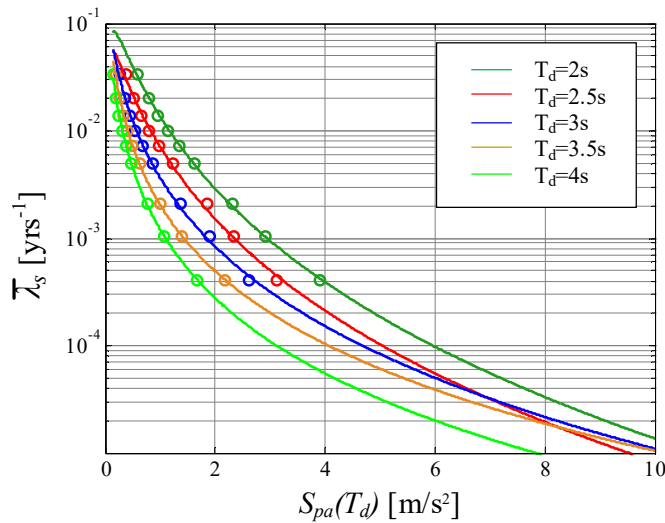
Figure 6.20 – L'Aquila: mean hazard curves for different T_d values. The dots denote the $\bar{\lambda}_S(s)$ values defined in the nine points $s_i = S(T_{R,i})$

6.3.2 *Reliability analysis results*

The annual average frequency of exceeding a specific limit state has been calculated basing on the *Law of Total Probability*, as the sum of the products between the conditional probability $P_{LS}(s)$ of exceeding the limit state given the seismic intensity level $S = s$, i.e., fragility, and the annual average frequency of S:

$$\lambda_{LS} = \int_0^\infty P_{LS}(s) \cdot \left| \frac{d\bar{\lambda}_S(s)}{ds} \right| ds \cong \sum_{i=1}^n P_{LS}(s_i) \cdot |\lambda_i| \qquad (6.19)$$

in which the summation is extended to a number n of points so that the estimation may be considered stable.

Once the λ_{LS} value, with reference to each limit state (Tables 6.6 and 6.7), has been determined, the probability of exceeding each limit state in fifty years has been calculated basing on the hypothesis of modelling the earthquakes occurrence as a *Poisson stochastic process* (Cornell, 1968):

$$P_{e,LS_i}(50yrs) = 1 - e^{-\lambda_{LS_i} \cdot 50} \qquad (\mathbf{6.20})$$

Limit state	Column drift index CDI_{is}	Acceptable Probability of failure P_f^*
Fully Operational	0.23 %	$5 \cdot 10^{-1}$
Operational	0.5 %	$1.6 \cdot 10^{-1}$
Life Safety	0.83 %	$2.2 \cdot 10^{-2}$
Near Collapse	1.67 %	$1.5 \cdot 10^{-3}$

Table 6.6 – Column drift index for isolated bridges, related to the different limit states and with reference to the acceptable failure probability values

Limit state	1	2	3	4	5	6	7	8	9
r [m]	0.10	0.15	0.20	0.25	0.30	0.35	0.40	0.45	0.50

Table 6.7 – In-plan radius values of FPS related to the different limit states

Hence, the reliability curves related to the isolation level and to the substructure have been obtained, with reference to the probability of exceeding each limit state in a 50-years timeframe.

6.3.2.1 *Substructure reliability curves*

The following diagrams show the reliability curves referred to the substructure. These curves have been plotted considering fixed the fundamental period T_d of the isolated bridge and varying both the substructure period T_p and the mass ratio λ (Figure 6.21).

It may be stated that all the considered limit states are respected and that the reliability is higher as the pier rigidity increases, that is, for low T_p values. Conversely, an increase in the FP vibration period involves an increment in the pier seismic demand.
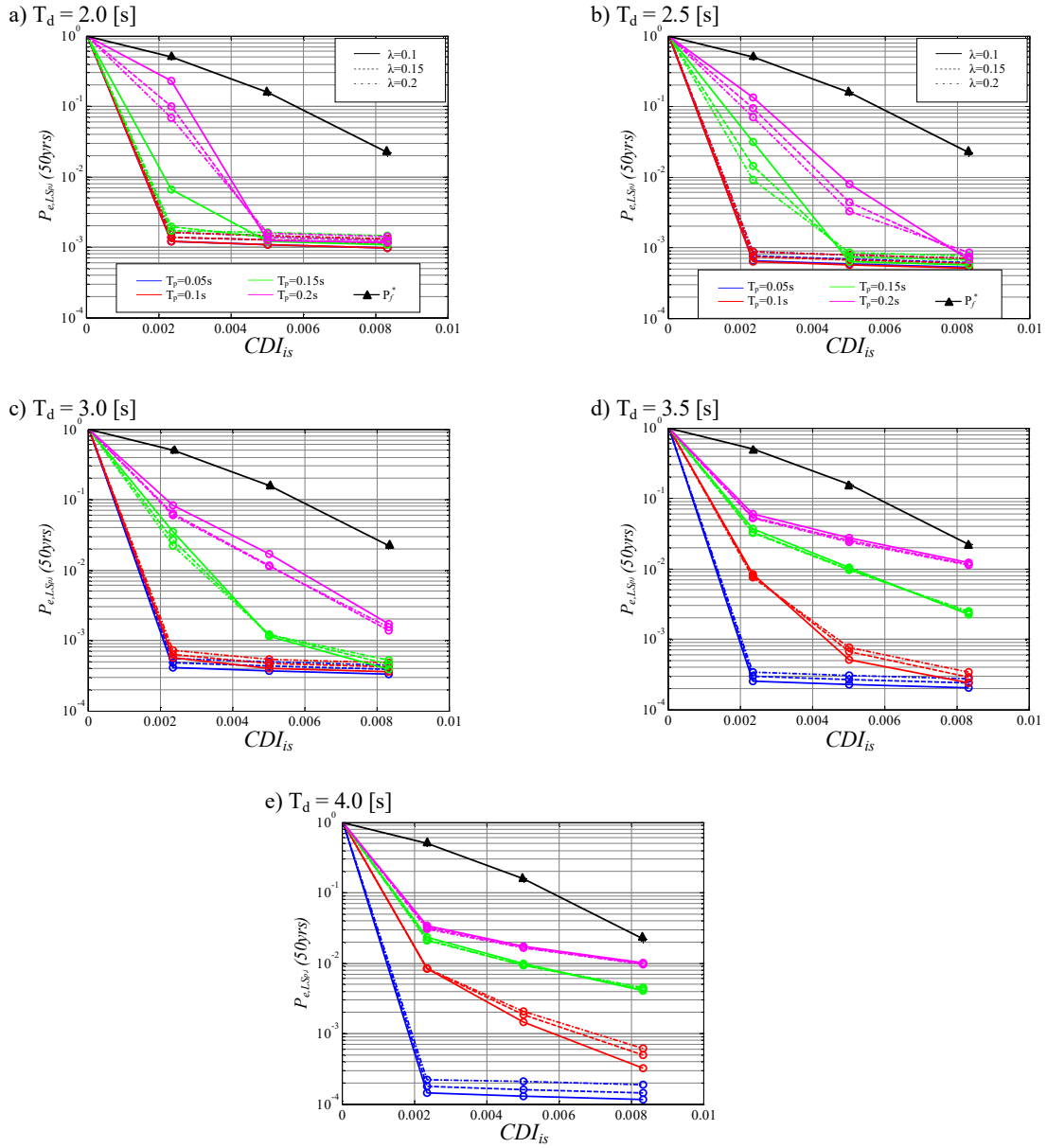
*Figure 6.21 – Reliability curves concerning the substructure,
for fixed T_d values and different T_p and λ values*

6.3.2.2 *Isolating system reliability curves*

The following diagrams show the reliability curves referred to the isolation system. These curves have been plotted considering fixed the fundamental period T_d of the isolated bridge and varying both the substructure period T_p and the mass ratio λ (Figure 6.22).
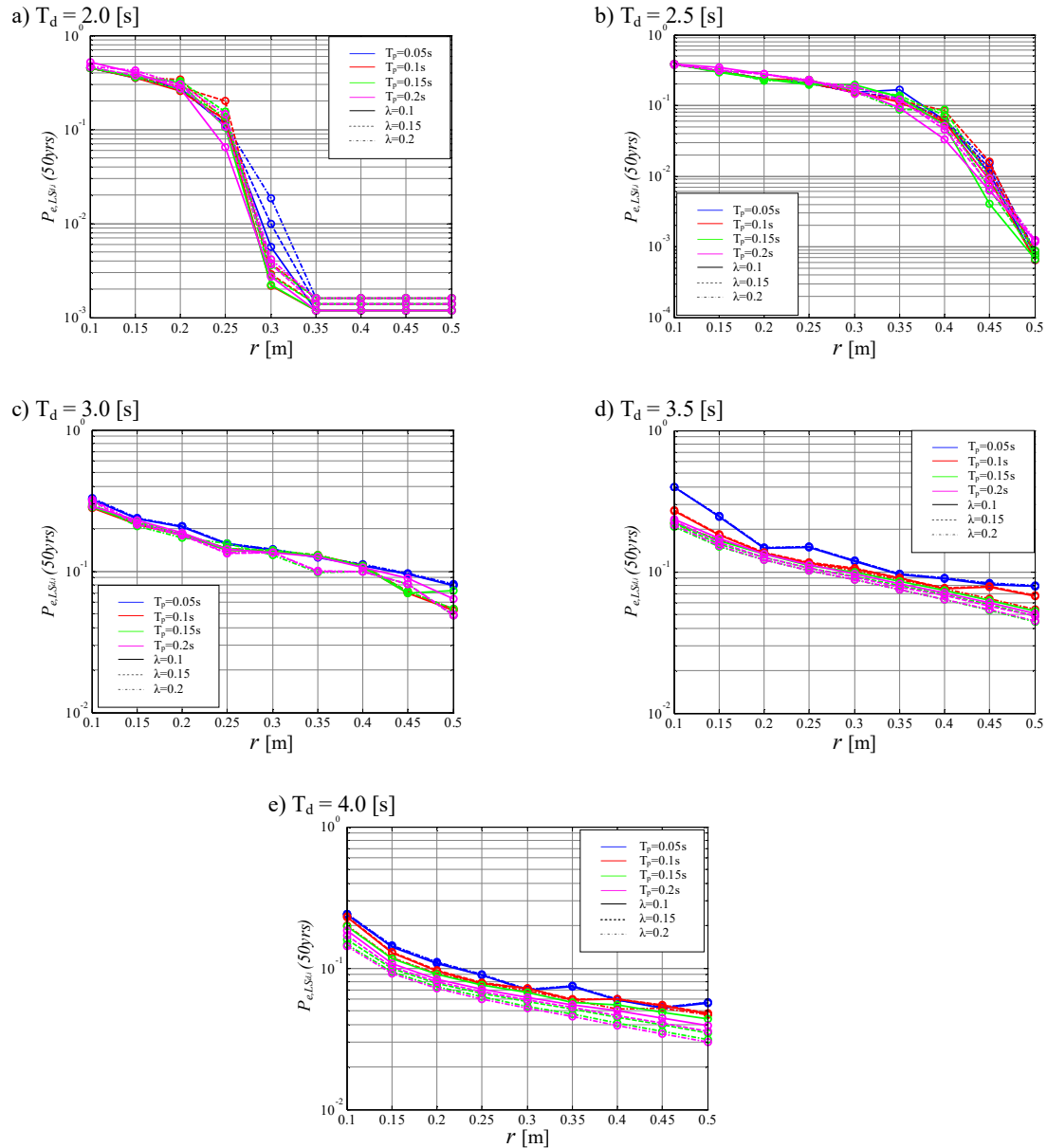
Figure 6.22 – Reliability curves concerning the isolating system, for fixed T_d values and different T_p and λ values

The reliability analysis results revealed that the isolating system is seismically less reliable as its fundamental period (and thus the curvature radius of the FP isolators) increases, since higher and higher exceedance probabilities correspond to the same limit state. This is related to the fact that an increment in the fundamental period moves the

isolated structure towards higher spectral displacement values, that is, the system becomes more and more flexible. For the same reason, the influence of T_p and λ is relevant only for the highest T_d values (Figure 6.22 – d-e).

The reliability curves of the isolating system have been then interpolated by a linear regression so as to obtain, in function of the fixed dynamic characteristics of the substructure and the isolator, the friction pendulum design diagrams, based on the in-plan radius r values to be provided for the FP design so that the probability of failure lies in a range whose order of magnitude may be considered acceptable, i.e., between 10^{-2} and 10^{-3} (Figure 6.23).
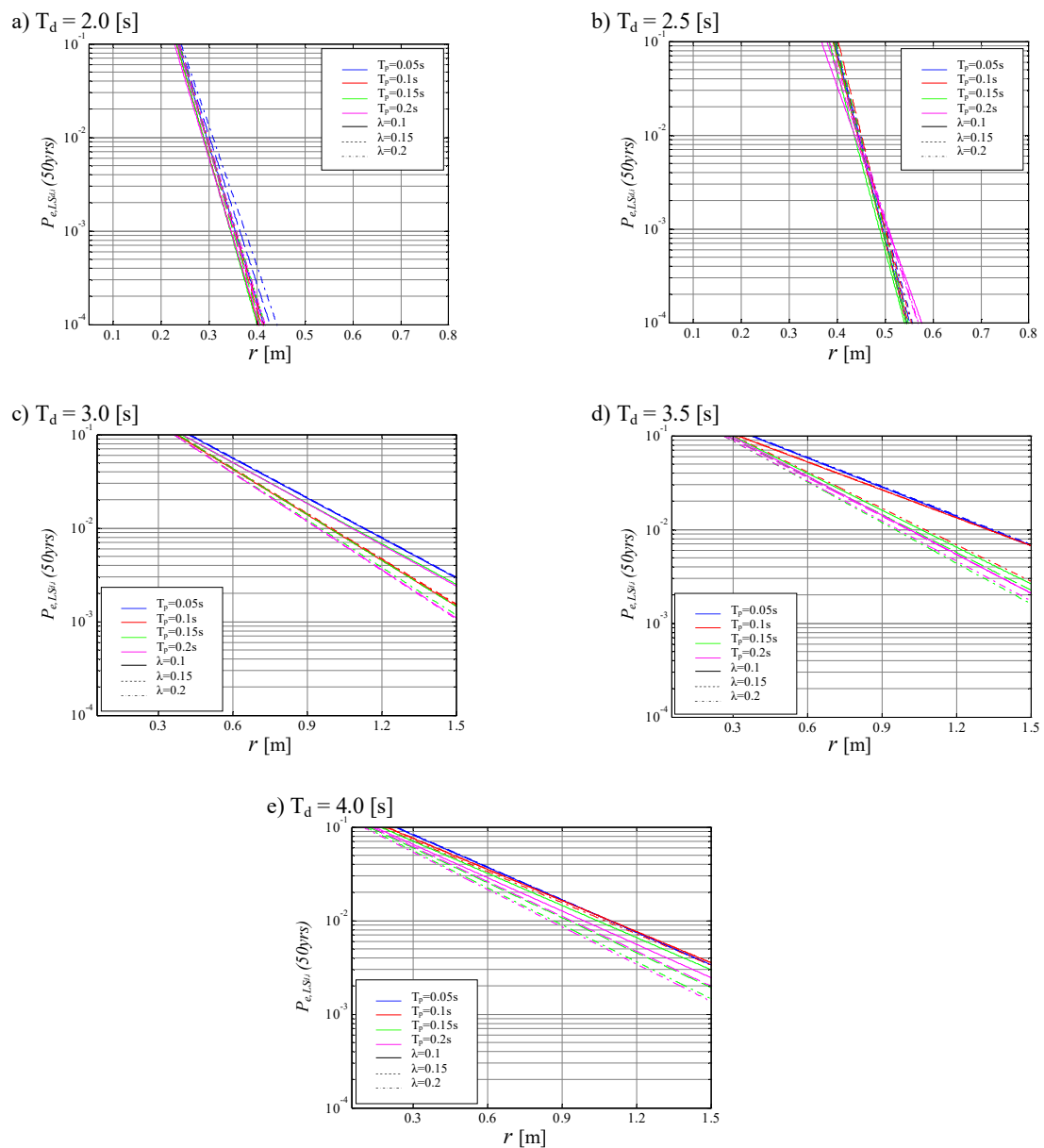
Figure 6.23 – Friction Pendulum System Design Diagrams,
for fixed T_d values and different T_p and λ values

CONCLUSIONS

The seismic reliability of a six-degree-of-freedom isolated bridge model has been assessed. 171,000 nonlinear dynamic parametric analyses have been performed, taking into account the intrinsic randomness of the Friction Pendulum devices dynamic behaviour and considering the earthquake input as a stochastic random process. The parametric analysis has been carried out by varying both these random variables and the main dynamic characteristics of the system, namely the vibration periods of the column and of the isolating system and the ratio between the pier and deck masses, i.e., mass ratio.

The structural model has been simulated through an algorithm implemented in the MATLAB & Simulink® computing software. The stability of the algorithm has been tested by performing two types of integration, in order to attain the most accurate approximation of the results. Accordingly, the analyses have been implemented considering both a fixed-step and a variable-step integration: as expected, this latter involved more precise results. The accuracy of the results produced by the MATLAB & Simulink® algorithm has been validated by making a comparison with the same model implemented in the professional software SAP 2000®.

The nonlinear dynamic parametric analyses results revealed an improvement in the response of the superstructure (deck), in terms of maximum displacement in function of increasing FPS friction coefficient values, whereas an optimum value of the friction coefficient for which the maximum pier displacement attains a minimum value has been observed. The latter is the result of two counteracting effects that follow an increase of the friction coefficient. The first effect is an increase in energy dissipation, which reduces the substructure displacements. The second effect is the increase of the isolator strength (and thus of the equivalent stiffness, with a reduction of the corresponding equivalent fundamental vibration period), which on the other hand increases the substructure displacements.

The estimates of the response statistics obtained for each parameter combination reflected the effect of the variability of the characteristics of the selected records at different intensity levels and they have been used for deriving fragility curves and for seismic risk analyses. Actually, after selecting a reference site, namely the town of L'Aquila (Abruzzo, Italy), relevant limit state functions have been derived, according to National and International regulations, in order to assess the fragility, i.e., the vulnerability, of the system,

by calculating the conditional probability of exceeding the different limit states considered, given a specific intensity of the seismic action.

In particular, an Incremental Dynamic Analysis (IDA) has been firstly performed to reach the relationship between the seismic demand and the capacity of the structure and evaluate the structural performance accurately. IDA curves provided appropriate result formats which allowed estimating the annual average frequency of exceeding predefined damage states and developing fragility curves of the bridge. Then, they have been integrated with hazard curves in order to evaluate the seismic reliability of the structure.

The fragility curves, referred both to the isolating system and the substructure, have been plotted in function of each limit state and for each dynamic characteristic of the bridge, namely the super- and substructure vibration periods and the mass ratio. It may be stated that the isolation system is efficient, as the pier fragility values resulted very low and almost all the displacements are concentrated at the isolating level. Actually, by increasing the period of the isolated bridge, the isolating system fragility gradually increases, as consequence of a higher displacement demand, typical of flexible structures. This phenomenon is very positive, as it demonstrates the efficiency of the isolating system, whose aim is uncoupling the superstructure from the substructure, so that nearly all of the displacement occurs over the height of the isolators. Additionally, the more the whole system is flexible, that is, for increasing periods values, the more the influence of the mass ratio is evident. Also the results concerning the pier fragility indicated that the more the whole system is flexible, the more it is fragile, but the high fragility values, i.e., those attaining the unit, are reached for seismic intensity values much higher than the case of the isolator and only for the first limit state (Fully Operational). By increasing the column period, the mass ratio effect is more marked, especially for the first limit sate. Clearly, for the lowest value of the mass ratio, the pier is more fragile, as it is more flexible.

Successively, the site's hazard curves have been developed in terms of spectral pseudo-acceleration, that is, the average number of events exceeding a definite value of the spectral pseudo-acceleration has been evaluated.

Once the annual average frequency of exceeding a specific limit state has been calculated, as the integral of the product between the system fragility and the seismic hazard of the site, the probability of failure in any time interval (in this study, fifty years) has been evaluated. Hence, they have been obtained the reliability curves related to the isolation level and to the substructure.

The reliability analysis results revealed that the isolating system is seismically less reliable as its fundamental period (and thus the curvature radius of the FP isolators) increases, since

higher and higher exceedance probabilities correspond to the same limit state. This is related to the fact that an increment in the fundamental period moves the isolated structure towards higher spectral displacement values, that is, the system becomes more and more flexible.

With reference to the substructure, it may be stated that all the considered limit states are respected and that the reliability is higher as the pier rigidity increases, that is, for low values of the column period. Conversely, an increase in the FP curvature radius involves an increment in the pier seismic demand.

Finally, the reliability curves of the isolating system have been interpolated by a linear regression so as to obtain, in function of the fixed dynamic characteristics of the substructure and the isolator, the friction pendulum design diagrams. These are based on the in-plan radius values to be provided for the FP design so that the probability of failure lies in a range whose order of magnitude may be considered acceptable. Consequently, it may be assured that the structure is able to perform, during all its useful life, the functions for which it has been designed.

Eurocode 8 - Design of Structures for Earthquake Resistance (Part 2: Bridges). (2005). Brussels: European Committee for Standardization.

Norme Tecniche per le Costruzioni. (2008). Gazzetta Ufficiale del 04.02.08, DM 14.01.08, Ministero delle Infrastrutture e dei Trasporti.

Ang, A., & Tang, W. (2007). Probability Concepts in Engineering-emphasis on Applications to Civil and Environmental Engineering.

Aslani, H., & Miranda, E. (2005). Probability-based Seismic Response Analysis. *Engineering Structures*.

Castaldo, P., & Tubaldi, E. (2015). Influence of FPS Bearing Properties on the Seismic Performance of Base-isolated Structures. *Earthquake Engineering & Structural Dynamics*.

Castaldo, P., Palazzo, B., & Della Vecchia, P. (2015). Seismic Reliability of Base-isolated Structures with Friction Pendulum Bearings. *Engineering Structures*, pp. 80-93.

Chu, S., Soong, T., & Reinhorn, A. (2005). Active, hybrid, and semi-active structural control: a design and implementation handbook. Wiley, United Kingdom.

Constantinou, M. C., Whittaker, A. S., Kalpakidis, Y., Fenz, D. M., & Warn, G. P. (2007). Performance of Seismic Isolation Hardware under Service and Seismic Loading.

Constantinou, M., Mokha, A., & Reinhorn, A. (1990). Teflon Bearings in Base Isolation II: Modeling. *Journal of Structural Engineering*.

Constantinou, M., Soong, T., & Dargush, G. (1998). Passive Energy Dissipation Systems for Structural Design and Retrofit. *Multidisciplinary Center for Earthquake Engineering Research*.

Constantinou, M., Whittaker, A., Fenz, D., & Apostolakis, G. (2007). Seismic Isolation of Bridges. University at Buffalo, State University of New York: *Department of Civil, Structural and Environmental Engineering*.

Cornell, A. (2004). Hazard, Ground Motions and Probabilistic Assessment for PBSD. In *Performance based seismic design concepts and implementation* (pp. 39-52). Berkeley, University of California: Pacific Earthquake Engineering Research Center.

Cornell, C., Jalayer, F., Hamburger, R., & Foutch, D. (2002). Probabilistic Basis for 2000 SAC Federal Emergency Management Agency Steel Moment Frames Guidelines. *Journal of Structural Engneering*, pp. 526-533.

Di Pasquale, G., Orsini, G., & Romeo, R. W. (2005). New Developments in Seismic Risk Assessment in Italy. In *Bulletin of Earthquake Engineering* (Vol. III, pp. 101-128).

Dolce, Cardone, & Croatto. (2005). Frictional Behavior of Steel-PTFE Interfaces for Seismic Isolation.

Dutta, A., & Mander , J. (1999). Seismic Fragility Analysis of Highway Bridges. *Proceedings of the Center-to-Center Project Workshop on Earthquake Engineering in Transportation Systems.* Tokyo, Japan.

Efraim, E., & Blostotsky, B. (2012). Design of Bridge Seismic Protection System and Selection of its Parameters using Capabilities of Simulink®. *14th International Conference on Computing in Civil and Building Engineering.*

FEMA 274. (1997). *NEHRP Commentary on the Guidelines for the Seismic Rehabilitation of Buildings.* Federal Emergency Management Agency.

Foti D., & Mongelli M. (2011). Isolatori sismici per edifici esistenti e di nuova costruzione: principi fondamentali, criteri di progettazione, dettagli costruttivi. Palermo: Flaccovio.

Ghobarah, A., & Ali, H. (1988). Design of Base-Isolated Highway Bridges. *Proceedings of Ninth World Conference on Earthquake Engineering*, *V.* Tokyo, Japan.

ISESD. (2016). Retrieved from *Internet-Site for European Strong-Motion Data*: http://www.isesd.hi.is/ESD_Local/frameset.htm

ITACA. (2016). Retrieved from *Italian Accelerometric Archive*: http://itaca.mi.ingv.it/ItacaNet/itaca10_links.htm

Jangid, R. (2008). Stochastic Response of Bridges Seismically Isolated by Friction Pendulum System. *Journal of Bridge Engineering.*

Kelly, J. (1996). Theory and Practice of Seismic Isolation Design. University of California, Berkeley: *Earthquake Engineering Research Center.*

Kelly, J. M. (1990). Base Isoaltion: Linear Theory and Design.

Luco, N., & Cornell, C. (2007). Structure-specific Scalar Intensity Measures for Near-source and Ordinary Earthquake Ground Motions. *Earthquake Spectra*, pp. 357-392.

Meletti, C., & Montaldo, V. (2007). Stime di Pericolosità Sismica per diverse probabilità di superamento in 50 anni: Valori di a_g. Retrieved from *Progetto DPC-INGV S1, Deliverable D2*: http://esse1.mi.ingv.it/d2.html

Mohka, A., Constantinou, M., & Reinhorn, A. (1988). Teflon Bearings in Aseismic Base Isolation: Experimental Studies and Mathematical Modeling.

Mokha, A., Constantinou, M., & Reinhorn, A. (1990). Teflon Bearings in Base Isolation I: Testing. *Journal of Structural Engineering.*

Palazzo, B., & Petti, L. (1995). Metodologie di Controllo di Sistemi Sismicamente Isolati. Università degli studi di Salerno.

PEER. (2016). *Pacific Earthquake Engineering Research Centre.* Retrieved from http://peer.berkeley.edu/

Pinto, P., Franchin, P., & Lupoi, A. (2009). Linee guida e Manuale applicativo per la Valutazione della Sicurezza Sismica e il Consolidamento dei Ponti esistenti in c.a. *Progetto DPC - Reluis 2005-2008 Linea 3: Valutazione e riduzione del rischio sismico di ponti esistenti*, (pp. 1-8, 43-52).

Pinto, P., Giannini, R., & Franchin, P. (2003). Seismic Reliability Analysis of Structures. Pavia, Italy: IUSS Press.

Priestley, M. (2000). Performance Based Seismic Design. *12WCEE.*

Priestley, M., Calvi, G., & Kowalsky, M. (2007). Direct Displacement-Based Seismic Design of Structures. *NZSEE Conference.*

Rahman, M., Ong, Z., Chong, W., Julai, S., & Khoo, S. (2015). Performance enhancement of wind turbine systems with vibration control: A review. *Renewable and Sustainable Energy Reviews*.

Rossetto, T., & Elnashai, A. (2003). Derivation of Vulnerability Functions for European-type RC Structures based on observational data. In *Engineering Structures* (Vol. XXV, pp. 1241-1263).

Ryan, K., & Chopra, A. (2004). Estimation of Seismic Demands on Isolators based on Nonlinear Analysis. *Journal of Structural Engineering*, pp. 392-402.

Structural Engineers Association of California. (1995). Performance-based Seismic Engineering. *SEAOC Vision 2000 Committee.* Sacramento, CA.

Vamvatsikos, D., & Cornell , C. (2002). Incremental Dynamic Analysis. *Earthquake Engineering and Structural Dynamics*.

Wood, S. (n.d.). Development of Performance-Based Seismic Design Procedures. Austin, Texas: Department of Civil Engineering, University of Texas.

Zayas, V., Low, S., & Mahin, S. (1987). The FPS Earthquake Resisting System. University of California, Berkeley: Earthquake Engineering Research Center.

Zayas, V., Low, S., & Mahin, S. (1990). A Simple Pendulum Technique for Achieving Seismic Isolation. *Earthquake Spectra*(6(2)), pp. 317-333.